
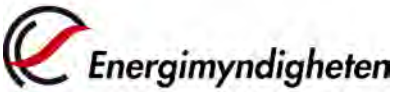


Project Report 43692-1

# Improved Borehole Technology for Geothermal Heat Pumps Development

*Authors :*
Alberto LAZZAROTTO
Willem MAZZOTTI PALLARD
Thierry RICHERT
Adrien VAUTRIN

January 14, 2021

# Acknowledgement

We would like to express our gratitude to the Swedish Energy Agency for supporting this project. The same can be said about our sponsors that supported the project with equipment, experience and data. Without them this project would have not been possible. A special thanks goes to THERMIA AB who provided a heat pump that was used for the project along with technical support, to TRIOPIPE AB who provided a coaxial borehole heat exchanger and data, to Bengt Dahlgren AB who provided services and data, and to Solifos AG for contributing with fiber optic cables.

We would also like to thank Jonas Anund Vogel to welcome the project within the Live-in Lab research activities and support us throughout the process of building the test-rig. A special thanks goes to Riccardo Sven Risuleo postdoctoral researcher in machine learning and system identification at the university of Uppsala and KTH for enriching the project with his knowledge about estimation and kernel methods.

# Contents

# Nomenclature

**Symbols**

| | | |
|---|---|---|
| $\alpha$ | annulus inner to outer radius ratio | |
| $\beta$ | center pipe inner to outer radius ratio | |
| $\chi(\alpha)$ | correction factor for $v$ and $\tau$ | |
| $\dot{V}$ | volume flow rate | $m^3/s$ |
| $\gamma$ | Euler–Mascheroni constant | |
| $\lambda$ | thermal conductivity | $W/(m \cdot K)$ |
| $\mathcal{W}$ | Lambert $\mathcal{W}$ function | |
| $\phi^*(\alpha)$ | correction factor for $f$ according to [10] | |
| $\psi(\alpha)$ | correction factor for $f$ | |
| $\rho$ | density | $kg/m^3$ |
| $\tau$ | shear stress | $Pa$ |
| $D$ | diameter | $m$ |
| $E_1(x)$ | exponential integral, $\int_x^\infty \frac{e^{-u}}{u} du$ | |
| $f$ | friction factor | |
| $L$ | length | $m$ |
| $P$ | pressure | $Pa$ |
| $R$ | thermal resistance | $m \cdot K/W$ |
| $r$ | radius | $m$ |
| $Re$ | Reynolds number | |
| $T$ | temperature | $^\circ$ / $K$ |
| $v$ | velocity | $m/s$ |

**Superscripts**

| | |
|---|---|
| $^*$ | modified or effective parameters |

**Subscripts**

| | |
|---|---|
| 0 | initial condition |
| *b* | borehole |
| *eq* | equivalent |
| *f* | fluid |
| *g* | ground |
| *h* | hydraulic diameter |
| *mid* | inner part of the annulus of a coaxial BHE |
| *o* | inner part of the center pipe of a coaxial BHE |
| *o* | outer part of the annulus of a coaxial BHE |

**Acronyms / Abbreviations**

ARMAX Auto-Regressive Moving Average with Extra Input

ARX Auto-Regressive with Extra Input

BHE Borehole Heat Exchanger

FIR Finite Impulse Response

GHG Green House Gas

GSHP Ground Source Heat Pump

ILS Infinite Line Source

RMSE Root Mean Square Error

SDR Standard Diameter Ratio

SSE Sum of Squared Errors

# Executive Summary

This report presents the final results of project *Improved borehole technology for Geothermal Heat Pumps development* financed by the Swedish Energy Agency. The project started in May 2017 and finished in June 2020. The project has been led by Dr. Alberto Lazzarotto and the work was carried out by Alberto Lazzarotto and Willem Mazzotti Pallard both from KTH – Royal Institute of Technology. Visiting students Adrien Vautrin from Insa Strasbourg and Thierry Richert from École Centrale de Lyon provided significant contribution to the project. Riccardo Sven Risuleo, postdoctoral researcher in machine learning at the University of Uppsala and KTH, also provided key contributions. The project benefited from in-kind contribution from Akademiska Hus, Asplan Viak, Avanti, Bengt Dahlgren, ClimaCheck, Einar Mattsson, Energi och Kylanalys, Geobatteri, HP Brunnsborrningar, Muovitech, Nowab, the Norwegian University of Science and Technology (NTNU), Palne Mogensen AB, Sindeq, Solifos, Stures Brunnsborrningar, Sweco, Thermia, Triopipe Geotherm, Tyréns, WellPerform, and Wessman Drilling Solution.

## Goals and background

Ground source heat pump is among the space heating and cooling technologies with greatest potential in terms of energy savings and emissions reduction in the building sector. Increased diffusion of the technology can be very beneficial for the reduction of Green House Gas (GHG) emissions which is key to achieve Sweden's goals in this regard.

While borehole technology is fairly established, there is still room for improvement in terms of design, testing, control, and monitoring. Such improvements could be the basis for a better integration of Ground source heat pump (GSHP) and Borehole Thermal Energy Storage (BTES) into the electric grid, easing issues such as limited capacity. This project aimed at tackling this challenge, touch upon all these points and provide new results that could have an impact on the technology. Experimental as well as theoretical investigation have been carried out to achieve these objectives. Most of the experimental work have been designed around the KTH Live-in Lab installation a laboratory within KTH campus with the goal of accelerating research within the built environment. The research covers the topics of coaxial borehole technology, thermal response test analysis methods and GSHP monitoring. The following sections provide an overview of the work done in each of these areas.

### *Hydraulic and thermal performance of borehole heat exchangers*

Effectiveness of borehole heat exchangers is measured in terms of pressure drop and thermal resistance. It is desirable to have the best heat transfer with the ground while keeping the pumping power as low as possible. While slight optimization of the borehole heat exchanger geometry can lead to small variation of the performance, only more significant changes in

the design can provide a disruptive result. The traditional types of borehole heat exchangers are single and double U-pipes fitted within a vertical borehole with lengths that may vary between 100 and 300 meters. The heat is extracted or injected into the ground by circulating a secondary fluid within the borehole and the heat transfer is driven by the temperature difference between the fluid and the so-called borehole wall. The innovative borehole type investigated within this project is a coaxial ground heat exchangers design with the annular pipe in contact with the borehole wall. This specific design has the advantage of improving the thermal contact between the circulating fluid and the surrounding ground (potentially reducing the thermal resistance).

In this work we performed an experimental investigation of the performance of this type of coaxial borehole heat exchanger and focused on the pressure drop aspect. A careful characterization of the pressure drop is necessary for the correct hydraulic design of borehole systems. According to our literature review this aspect is not yet completely understood for the specific case of coaxial borehole heat exchangers. Our goal here was providing our experience along with improved tools to enables engineers to perform more accurate calculation of the pressure drop for coaxial BHEs. Furthermore, we wanted to compare the pressure drop measurements of coaxial systems alongside the state of the art technology the U-pipe.

The performed study covers the theory of pressure losses in the annular region of coaxial pipes and a comparison between modeled pressure drop with pressure drop measurements from six installations. The measurements were performed on boreholes of various lengths and with different cross-section geometry. The results found indicate that theoretical pressure drop underpredicts actual pressure drop. The analysis performed on this difference for several coaxial BHE suggests that it is the linear pressure drops that should be corrected, rather than accounting for singular losses at the bottom and the top. More pressure loss measurements for coaxial installations will be needed to strengthen the evidence of this result. A more complete understanding of this issue may lead to an improvement of the coaxial BHE design. Finally the comparison between measurement from coaxial boreholes and U-pipes suggests that the pressure losses for coaxial pipes are lower or comparable to the one of U-pipes for a given flow rate.

### *Innovative method for testing borehole heat exchangers*

Proper borehole heat exchanger design and GSHP control are key to ensure high performance and robustness of these systems. The main body of work found in the scientific literature addresses mainly the design issue and much less work has been performed when it comes to control of borehole systems. In this work we take a look at the limitation and potential improvement of Thermal Response Test (TRT), a key tool used in the design stage for the thermal characterization of BHEs. Furthermore we investigate how this testing methodology could be extended to provide more information on the dynamic response at shorter time-scales which is very useful for the optimal design of the control strategy.

TRT is the state-of-the-art methodology for in situ thermal characterization of borehole heat exchangers and is the key tool to ensure a design of BHE installation that guarantees the expected performance during the whole life-time of the system. The test consists in injecting a step of power into the ground for about three days and measure the change in fluid temperature in time. The measurements are then used along with a physical model of the ground to determine the parameters yielding the best fit between model and measurement data.

In this study, we focus on a well known limitation of practical implementation of TRT, the discrepancy between the ideal test requirements and the actual test condition on the field. In particular, we performed a theoretical study to investigate the effects that noisy measurements and drifting loads can have on the test results and we concluded that TRT is rather robust to noise but does not handle well power drifts overtime. The simulation performed showed that in extreme cases where the drift is severe a test complying with the ASHRAE criteria for TRT can yield a difference in conductivity of up to 25% compared to the *true* value when using the standard procedure and other methods accounting for power changes gave more reliable results. On the other hand when data are exclusively affected by white noise, which is accounted as a variation in power, the reverse result was found. That is, the standard TRT procedure yielded to robust results while the method accounting for power changes did not.

These results motivated the investigation of alternative methods for the analysis of the TRT tests with the goal of improving the robustness to noise and power drifts. A major reason for these deviations is the so called model error, which is the difference between the model used to fit the data and the actual *true* behavior of the system. In the traditional TRT analysis we make a strong choice on the parametric model utilized to fit the data. This choice is based on a reasonable physical model, but the reality can be more complicated and the model might be insufficient to describe well the behavior of the system. A potential solution to this problem is relaxing the hypothesis on the model and make it more flexible and capable of fitting a larger variety of behaviors. Following this reasoning, we explored what in literature goes under the name of non-parametric models. Since these models are more flexible, they are expected to reduce the model error and as a bonus provide a good characterization of short dynamics which is not given using the traditional analysis.

A full scale experimental rig for testing these methods has been designed and built from the ground up. The design used provides the required flexibility in terms of load exchanged with the ground, and in terms of measurement equipment used. The test-rig was utilized to run several tests and produce datasets consisting of power injected and relative temperature response. The analysis procedure required dividing the datasets collected into training set and testing set. The first set was used to identify the temperature response to a step heat injection, and the second one to compare temperature data with predictions made with the model based on the response identified. The result obtained showed very good agreement between prediction and measurement data especially in the early transient region. These results are very promising since this type of methodology could be applied to determine in-situ the response of a particular borehole and tune its control strategy. The estimation could be performed both from traditional step heat load signal, but also from variable input load. This is very important because it means that also "imperfect" input signals can be effectively used to produce a good estimate of the step response.

### *Monitoring of borehole systems*

Monitoring the performance of borehole fields and geothermal heat pumps is key to test the technology on the field and highlight potential issues and improvements of these systems. Within the scope of the project we followed up two installations: the test-rig at KTH Live-in Lab and the GSHP on the property *Forskningen 2*. The first one is the test-rig presented in the previous section, while the latter one is a GSHP connected to 11 boreholes and supplying the energy demand for space heating and domestic hot water of 3 buildings used as student accommodations.

The goals of the monitoring were the evaluation of the performance of the system and the comparison of behavior of long and short boreholes within the same borehole field which is a peculiarity of the *Forskiningen 2* borehole installation . The data available comprise electricity use of the compressor and pumps along with heat exchanged and inlet and outlet temperatures in several key locations of the system such as the borehole loop, the evaporator loop and the condenser loop. The measurement data have been analyzed and key parameters have been visualized and compared side by side. We analyzed the performance of the borehole by looking at the heat exchanged with the ground and the temperature at the inlet and outlet of the borehole loop. In addition to these data, Distributed Temperature Sensing (DTS) measurements were collected in three boreholes. The DTS data provide temperature profile along the borehole depth and a finer view of the heat transfer process at different depth. In each of the borehole analyzed it is possible to notice heterogeneity in the heat transfer at different depths by looking at the temperature profile. A trend observed is the increase in temperature along the depth. On top of this trend, anomalies were registered on a few sections where discontinuities in the temperature profile could be appreciated and higher temperature were recorded. This data highlights the added value that DTS monitoring can provide in observing the real behavior of the underground with great level of detail from a spatial perspective and over an extended period of time. The DTS measurement were planned to be complemented by power measurements in each individual borehole. This portion of the project has unfortunately not been yet fully implemented, hence there are still uncertainty in the comparison between long and short boreholes because information on the proportion of heat exchanged in the different boreholes is not yet available. On a positive note, the sensors are already in place and they might serve as a starting point in a future project.

Going into the system level, the heat pumps performance were evaluated in term of COP on an hourly basis. As expected, the data show a clear increase in COP as the inlet evaporator temperature raise. On the other hand is harder to appreciate a correlation between the COP and the inlet fluid temperature in the evaporator. Finally, monthly performance factor (MPF) for the overall system including pumping power on the source and sink sides, fans of the air handling unit were evaluated on a monthly basis. The MPF evaluated only considering the compressor electricity (MPF1) is between 3.5 and 3.9 The MPF is reduced by 20% when accounting for pumping (MPF4). The overall MPF (MPF5) appear quite stable over time, without any large difference between summer and winter periods suggesting that the system can provide consistent performance throughout the whole year.

## The infrastructure

A major part of the experimental activities have taken place within the KTH Live-in Lab platform. KTH Live-in Lab is an infrastructure to accelerate innovation within the built environment. It provides a place for companies and researchers to come together and test new ideas as well a channel to communicate research. KTH Live-in Lab is equipped with a borehole system. A detailed description of the borehole system is provided in chapter 3 of this report but essentially the main feature that set this system apart is the presence of a dedicated research borehole that could be used exclusively for testing. This feature provided the required freedom necessary to carry out this research project.

# Publication list

1. A. Lazzarotto, W. Mazzotti, *Thermal response test performance evaluation with drifting heat rate and noisy measurements*, Proceeding of European Geothermal Congress, The Hague, 2019

2. A. Vautrin, *Development of a new test method for the thermalcharacterization of borehole heat exchangers*, Master's thesis, August 2019, Stockholm.

3. T. Richert, *Development of a test unit for innovative testing of borehole heat exchanger*, Report, June 2020, Stockholm.

In April 2020, Willem Mazzotti presented his mid-term seminar, a stepping stone in his Ph.D studies. In the discussion with the opponent Johan Claesson from Chalmers, several results from the project were presented and discussed.

Part of the work produced within this project is still under publication process. Topics that will be covered in upcoming publications are the evaluation of the effect of noise on TRT tests, pressure drop in coaxial heat exchangers and the use of kernel methods for non parametric estimation of borehole thermal response.

# Chapter 1

# Pressure Drop in coaxial borehole heat exchangers

The most commercially used BHE type is the U-pipe. Other types of BHE design have been investigated over the years to improve hydraulic and thermal performance of U-pipes but did not have the edge to earn a significant market share. Part of the reason is lack of testing and information about new design which makes it difficult for new concepts to be considered. In this chapter we focus our attention on coaxial heat exchangers, a BHE type with interesting properties from a thermal and hydraulic perspective. In particular, we will focus on the hydraulic performance of coaxial BHE due to lack of information found in the BHE literature regarding modeling of pressure drop in the annular region. The study includes:

- a literature review of studies on pressure drop in the annular region.
- implementation of a suitable model for the analytical prediction of pressure drop in the annular region.
- pressure drop measurements at the Live-in lab borehole coaxial BHE and collection of other pressure drop data-sets for coaxial borehole heat exchangers as well as for U-pipe and double U-pipes.
- analysis of modelled prediction and measurement data.

## 1.1 Data-sets

Pressure drop measurements from 6 coaxial boreholes, 3 single U-pipes and 1 double U-pipe were gathered. The main goal of this chapter is to focus on coaxial system but we consider important including data-sets of U-pipes in order to have a reference of hydraulic performance. The properties of the boreholes used for this analysis are given table 1.1. Definition for the geometrical parameters of the two configurations is provided in figure 1.1 and 1.2. The data-set from the Live-in-labs borehole were collected by Mazzotti and Vautrin within the framework of this project. The data-sets from Asker and Ingemar were collected by Mazzotti in the framework of the project "Deep borehole for Ground Source Heat Pumps" (40934-1). The data-set labeled Andersson [1] was kindly provided by Klas Andersson. The data-sets from Sigtuna, Stora Frosunda and Juvelen were kindly provided by José Acuña and Milan Stokuca (Bengt Dahlgren). The data-set from Norrtälje, Alkoven and Veddesta were provided by Triopipe AB and Bengt Dahlgren.

Each installation studied has its peculiarity. For the Ingemar BHE, the section is tighter for the final 150m (the diameter is reduced to 41mm from 44.1mm). For Andersson's installation, the $D_{mid}$ is greater (68mm) for the top 86m, because of an additional insulation layer of 14mm thickness. For Sigtuna, Stora Frösunda and Juvelen, and additional 6 meters of 20mm pipes outside the borehole needs to be taken into account in the pressure drop computation due to the position were the measurements were performed. These geometrical variations are taken into account for the linear pressure loss estimation.

*From here on, the investigated boreholes will be referred to by a character and a number. The character is "c", "u" or "d", corresponding to the type (coaxial, U-pipe or double-U-pipe) and the number is the length of the BHE in meters.*

**U-Tube**

| Borehole | Length [m] | $D_{int}$ [mm] | Fluid |
|---|---|---|---|
| Ingemar (u510) | 510 | 44.1 | EA 24.5-wt% |
| Sigtuna (u160) | 160 | 35.2 | EA 30-wt% |
| Stora Frösunda (u330) | 330 | 44 | EA 16-wt% |
| Juvelen (d250) | 250 (x2) | 28.2 (x2) | Water |

**Coaxial**

| Borehole | Length [m] | $D_o$ [mm] | $D_{mid}$ [mm] | $D_i$ [mm] | Fluid |
|---|---|---|---|---|---|
| Live-in Labs (c100) | 100 | 114 | 50 | 35.2 | EA 24.5-wt% |
| Asker (c800) | 800 | 150-165 | 75 | 66.2 | Water |
| Andersson (c170) | 170 | 114 | 40–68 | 35.2 | Water |
| Veddesta (c230) | 230 | 114 | 40–50 | 35.2 | Water |
| Alkoven (c250) | 250 | 114 | 40–50 | 35.2 | Water |
| Norrtälje (c200) | 200 | 114 | 40 | 35.2 | Water |

**Table 1.1:** Properties of the boreholes

## 1.2 Pressure drop Model

The goal of this work is providing tools to better predict the pressure drop in a coaxial heat exchanger systems and ease the design phase. To achieve this objective, a model for pressure drop in BHE is essential.

The general expression of the pressure drop, given by equation (1.1) can be used to get the theoretical pressure drop of the coaxial BHE :

$$\Delta P = f_o \frac{L\rho v_o^2}{2D_{eq}} + f_i \frac{L\rho v_i^2}{2D_i} \tag{1.1}$$

Where the index $o$ refers to the annuli part (exterior), $i$ refers to the inner pipe, and $eq$ stands for equivalent diameter (usually taken as the hydraulic diameter $D_h$).

In the Jones Jr. and Leung [10] paper, a correction factor is applied to the Reynolds number in order to find a modified friction factor in the annulus. But how should pressure

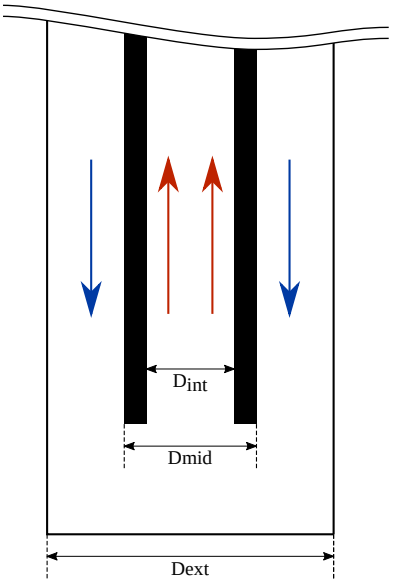


**Figure 1.1:** Diameters definition for coaxial borehole

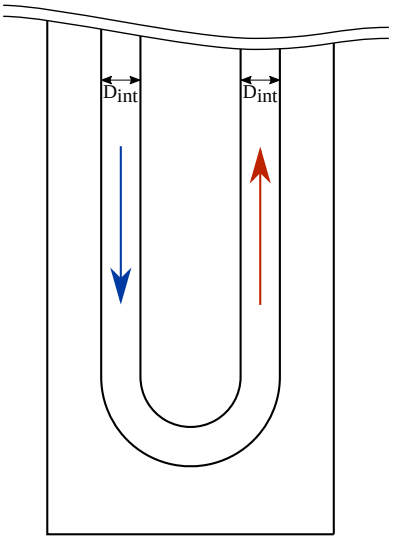


**Figure 1.2:** Diameters definition for U-tube borehole

be calculated in the annulus? Should the correction factor also be applied to the hydraulic diameter? It is not fully clear from the paper and in this section we will try to eliminate some of the confusion in this regard. In their article, the two authors define friction factor as

$$f = 8\frac{\bar{\tau}_w}{\rho v^2} \tag{1.2}$$

where $\bar{\tau}_w$ is the perimeter-averaged wall shear stress and $v$ is the average fluid velocity. For laminar flow, the shear stress as a function of the radius is given as

$$\tau_r = -\frac{r_o}{2}\frac{dP}{dx}\left(\frac{r}{r_o} + \frac{1-\alpha^2}{2ln(\alpha)}\frac{r_o}{r}\right) \tag{1.3}$$

where $r_o$ is the outer radius, $\alpha$ is the inner to outer radius ratio and $\frac{dP}{dx}$ is the pressure loss along the flow direction (negative). Accordingly, the perimeter-averaged shear stress can be found to be

$$\bar{\tau}_w = \frac{r_{mid}}{r_{mid}+r_o}\tau_i + \frac{r_o}{r_{mid}+r_o}\tau_o \tag{1.4}$$

$$= -\frac{r_o}{2}\frac{dP}{dx}\frac{1}{1+\alpha}\chi(\alpha) \tag{1.5}$$

where $r_{mid}$ is the outer diameter of the central pipe and

$$\chi(\alpha) = \alpha^2 + 1 + \frac{1-\alpha^2}{ln(\alpha)} \quad . \tag{1.6}$$

Moreover, the average velocity can be shown to be

$$v = -\frac{dP}{dx}\frac{r_o^2}{8\mu}\chi(\alpha) \quad . \tag{1.7}$$

In turn, this leads to the following expression for the friction factor

$$f = \frac{64}{Re}\frac{1-\alpha}{1+\alpha} = f_h \cdot \psi(\alpha) \quad . \tag{1.8}$$

where $Re$ is the Reynolds number defined with the hydraulic diameter $D_h = 2r_o(1-\alpha)$.

**Note:** the expression of eq. 1.8 is not the same as that found in [10]. This is clarified later on in this section.

The pressure drop in the annulus per meter of pipe under laminar flow can then be expressed by combining eqs. 1.2, 1.4 and 1.8

$$-\frac{dP}{dx} = f\frac{\rho v^2}{4r_o}\frac{1+\alpha}{\chi(\alpha)} \tag{1.9}$$

$$= f_h\frac{\rho v^2}{2D_h}\frac{(1-\alpha)^2}{\chi(\alpha)} \tag{1.10}$$

$$= f_h\frac{\rho v^2}{2D_h}\frac{1}{\phi^*(\alpha)} \tag{1.11}$$

where $\phi^*(\alpha)$ is the correction term given by [10]. Now, this expression is valid for laminar flow but how does it apply to turbulent flow? Jones Jr. and Leung [10] argue that, for smooth pipes, the friction factor is solely dependent on the Reynolds number, $Re$. Thus, the friction factor for turbulent flow rates should be calculated with the modified Reynolds number $Re^* = Re \cdot (\psi(\alpha))^{-1}$, so that

$$f = \begin{cases} \frac{64}{Re^*} \ , & for\ Re^* < 2000 \\ (0.838 \cdot \mathcal{W}(0.629Re^*))^{-2} \ , & for\ Re^* \geq 2000 \end{cases} \tag{1.12}$$

where $\mathcal{W}$ is the Lambert $\mathcal{W}$ function (Kármán-Prandtl approximation for smooth pipes).

Note that the starting point of this derivation was to define the friction factor as a function of the wall shear stress (eq. 1.2). For pressure drop calculations, it is perhaps more natural to use the effective friction factor defined as

$$-\frac{dP}{dx} = f^*\frac{\rho v^2}{2D_h} \quad . \tag{1.13}$$

With this definition, the modified friction factor $f^*$ may be expressed as

$$f^* = f(Re^*)\frac{1-\alpha^2}{\chi(\alpha)} \quad . \tag{1.14}$$

It is easy to check that $f^* \to f(Re) = f_h$ for $\alpha \to 0$. For $\alpha \to 1$, it can be numerically verified that $f^* \to \infty$ (for turbulent flow). This makes sense. On the one hand, as the radius ratio approaches 0, the concentric geometry approaches a fully circular (pipe) geometry. The friction factor then approaches that of the pipe problem. On the other hand, as the radius ratio approaches 1, the annular space vanishes which "creates" an infinitely large resistance to the flow (no circulation can then occur). The friction factor then approaches infinity.

It is important to keep in mind that all the previous developments are based on the shear stress definition of the friction factor (eq. 1.2). This leads to a corrected Reynolds number (eq. 1.8) and an additional correction to find the effective friction factor (eqs.1.13-1.14). If instead the friction factor is initially defined as

$$-\frac{dP}{dx} = f\frac{\rho v^2}{2D_h} \quad , \tag{1.15}$$

then only a correction on the Reynolds number emerges. This correction is

$$Re^* = Re \cdot \phi^*(\alpha) = \frac{\rho v D_h}{\mu}\phi^*(\alpha) \quad , \tag{1.16}$$

as appears in [10] and in eq. 1.9. It is therefore very likely that Jones Jr. and Leung [10] used the "pressure drop" definition of the friction factor, although it is inconsistent with the derivation provided in their article. One must remember that the shear stress and pressure drop definitions of the friction factor are not equivalent for the concentric pipe geometry. For the rest of the report, the "pressure drop definition" of the friction factor will be used. Hence,

$$f = f(Re^*) = f(Re \cdot \phi^*(\alpha)) \quad . \tag{1.17}$$

Again, it can easily be shown that $f(Re^*) \to f(Re) = f_h$ for $\alpha \to 0$. For $\alpha \to 1$, $\phi^*(\alpha)$ converges to a value of 2/3.

## 1.3 Optimal geometry for pressure drop considerations

Back to eq.1.1, it may be rearranged into

$$\Delta P = \frac{8\rho \dot{V}^2 L}{\pi^2 D_o^5}\left(\frac{f_o(Re_o^*)}{(1-\alpha)(1-\alpha^2)^2} + \frac{f_i(Re_i)}{\alpha^5\beta^5}\right) = \frac{8\rho \dot{V}^2 L}{\pi^2 D_o^5} f_{eq}(Re_o, \alpha, \beta) \quad . \tag{1.18}$$

where $Re_i$ refers to the inner pipe Reynolds number, $\beta$ is the center pipe inner ($r_i$) to outer ($r_{mid}$) radius ratio and $f_{eq}$ is the equivalent friction factor for the whole coaxial BHE. $Re_i$ may be expressed as a function of $Re_o = Re_o^*(\alpha = 0)$

$$Re_i = \frac{Re_o}{\alpha\beta} \quad , \tag{1.19}$$

which explains the non-dependency of $f_{eq}$ on $Re_i$.

Additionally, eq. 1.18 may be rewritten as

$$\frac{\Delta P}{L} = Re_o^2 \frac{\mu^2}{2\rho D_o^3} f_{eq}(Re_o, \alpha, \beta) \quad . \tag{1.20}$$

So for any given borehole diameter, here $D_o$, given fluid properties and given flow rates (which, combined with the two previous constraints is equivalent to a fix $Re_o$) the pressure drop per meter is minimized when $f_{eq}$ is minimized. The equivalent friction factor is shown in fig. 1.3 for different annulus radius ratios and Reynolds numbers ($Re_o$). The center pipe Standard Diameter Ratio (SDR) is fixed to 17, which is equivalen to $\beta = 0.88$. The minimum friction factor for each Reynolds number is also plotted as a dotted black line. A zoomed-in version of fig. 1.3 is provided in fig.1.4. When the flow is laminar in both the center pipe and the annulus, the position of the minimum becomes independent of the (borehole) Reynolds number. The minimum pressure drop is reached for $\alpha \approx 0.59$ For fully turbulent flows, the position of the minimum pressure drop slightly depends on the Reynolds number, although the change is small ($\alpha \approx 0.66 - 0.67$). Note that the pressure drop minima do not necessarily occur at the geometry leading to equal pressure drop in the annulus and the center pipe. This is exemplified in fig 1.5 which shows the shares of each channel in the total pressure drop for $Re_o = 5000$.

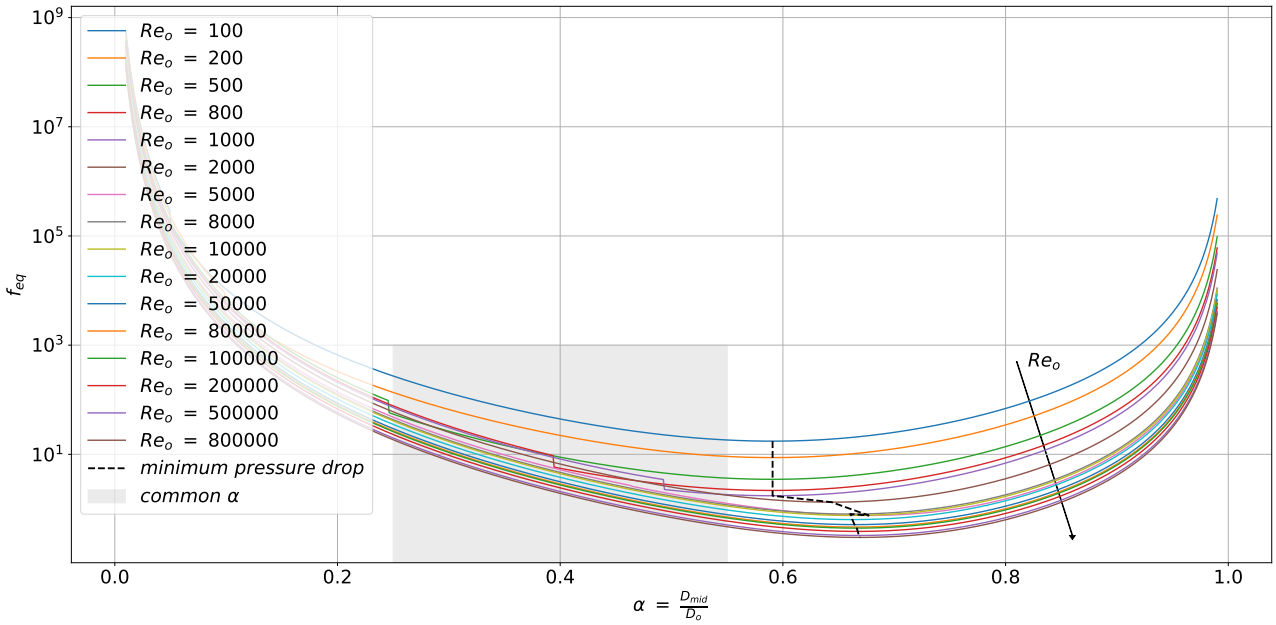


**Figure 1.3:** Equivalent friction factor for different annulus radius ratios and Reynolds numbers ($\beta = 0.88$)

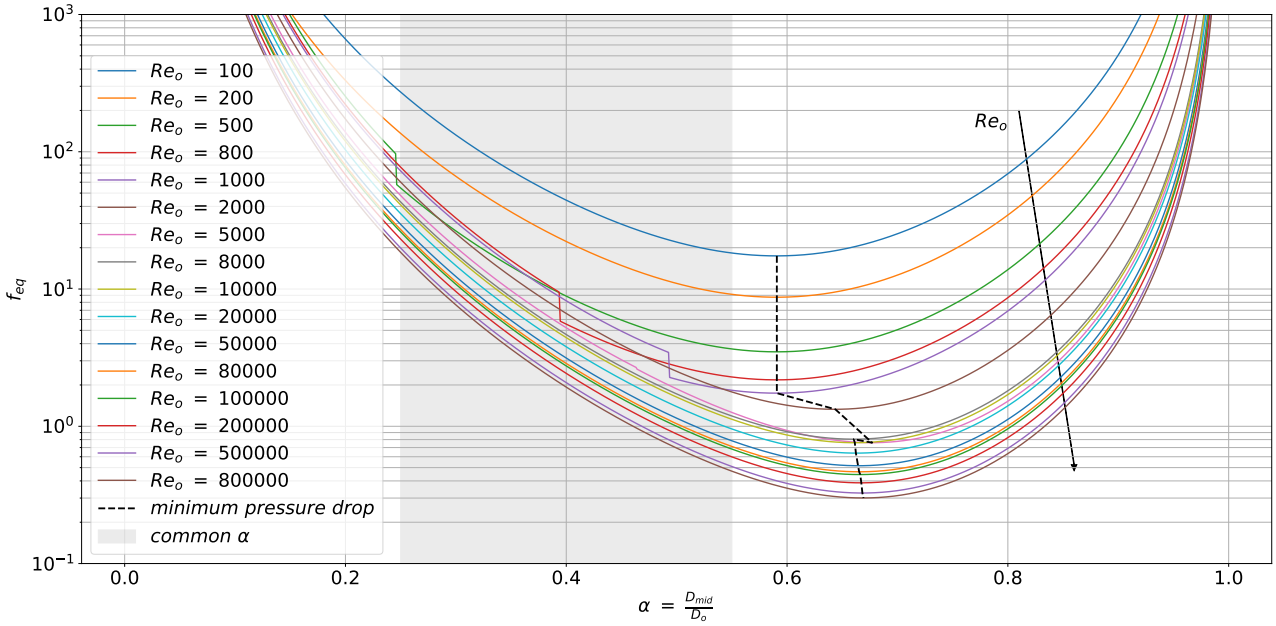


**Figure 1.4:** Equivalent friction factor for different annulus radius ratios and Reynolds numbers ($\beta = 0.88$) - Zoom

One may notice that the pressure drop minima occur outside the area of common coaxial BHE annulus ratio. There is approximately one order of magnitude ($\times 10$) between the minimum pressure drop and the pressure drop at common radius ratios. Pressure drop is, however, not the only performance indicator to account for in a design stage. Thermal considerations, in particular as regards thermal shunt, are also of importance to find suitable geometries. This is likely to explain why smaller ratios are in practice. Smaller center pipes are also easier to install. Moreover, this short study is only theoretical and comparison with data is needed in order to understand how well the linear pressure loss model fits measurements.

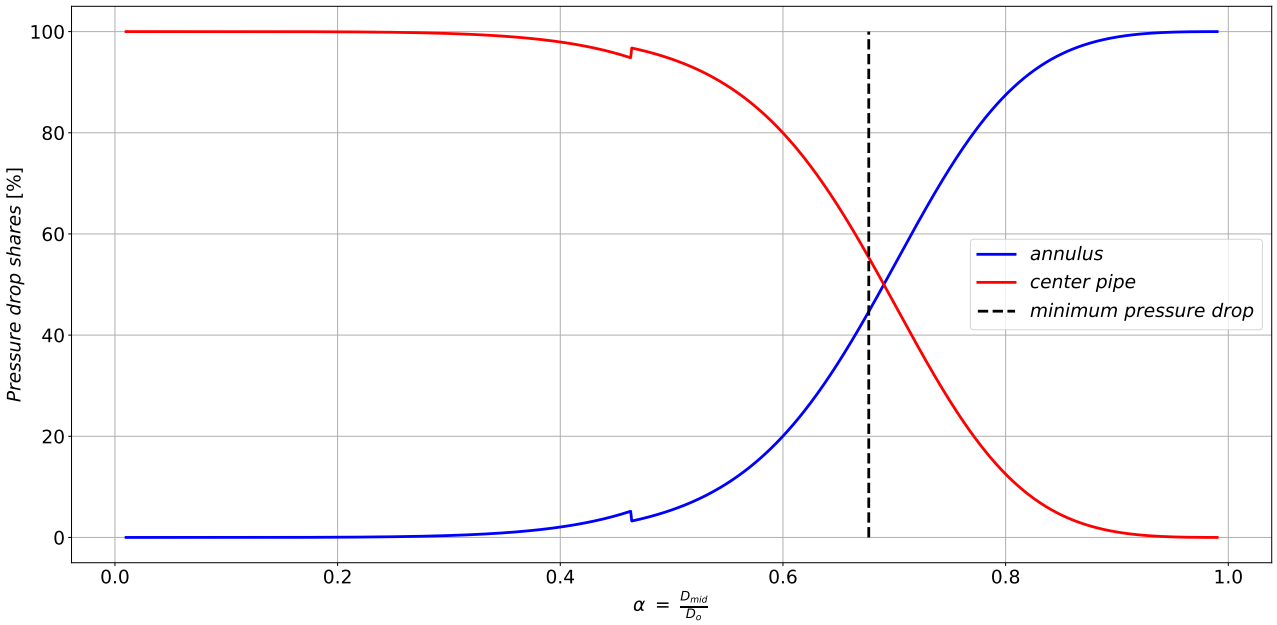


**Figure 1.5:** Contribution of the annulus and the center pipe in the total pressure drop of a coaxial BHE for different geometries ($Re_o = 5000$)

## 1.4 Characterisation of the pressure losses for a coaxial BHE

### 1.4.1 Analysis of the available data

Figure 1.6 shows pressure drop per meter vs flow rate for the data-sets introduced in section 1.1. The data are plotted on a log-log scale. The visualization displays the measurement data with crosses, and modelled curves with continuous lines.

The first observation that can be made is that the coaxial BHE c800 has the lowest linear pressure drop compared to the other BHEs. This fact is due to the pipe used. This pipe has a very large diameter when compared to the two other coaxial BHEs and yields a much lower pressure drop for a given flow rate. The second observation is that there is a significant difference between the modelled pressure drop and the measured one. This difference could be explained by singular losses or by limitations of the model used to predict the losses. In this section we will quantify the difference and gather the necessary information to better explain this discrepancy. Figure 1.6 suggests that a way to describe the pressure drop is :

$$\begin{aligned} log_{10}(\frac{\Delta P}{L}) &= a * log_{10}(V) + b \\ \Leftrightarrow \frac{\Delta P}{L} &= 10^b * V^a \end{aligned} \tag{1.21}$$

The coefficients a and b were computed by linear regression for theoretical and experimental data, and are displayed table 1.2. The regression could not be done on the c230 and c250 because data was available for only one flow rate value.

For all the other boreholes, the values of $a$ are matching better than the $b$ values. This means that the regression lines are almost parallel but do not overlap. As a matter of fact, the theoretical calculations always underpredict the empirical values, as seen on figure 1.6. This is expected: the theory only accounts for pressure drop in straight, smooth pipes. Additional

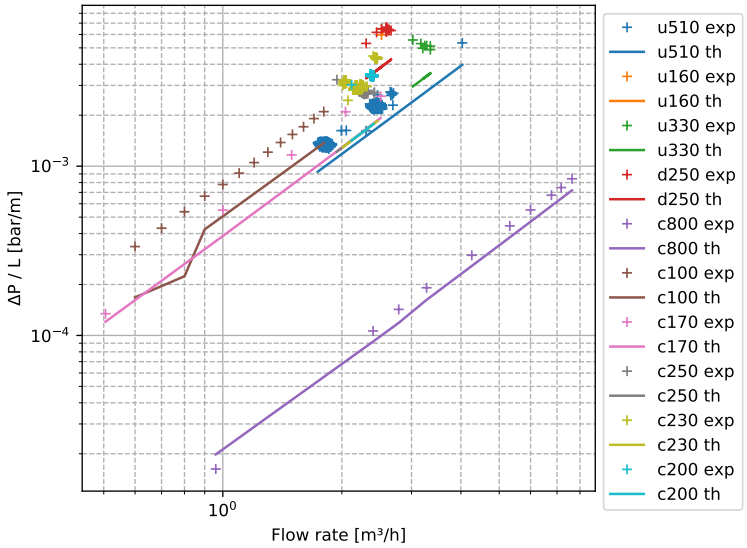


**Figure 1.6:** Pressure drop by unit of length, experimental, theoretical, and relative error

| BHE | a exp | b exp | a th | b th | $\frac{a_{exp}-a_{th}}{a_{th}}$ | $\frac{b_{exp}-b_{th}}{b_{th}}$ |
|---|---|---|---|---|---|---|
| c800 | 1.87 | 1.95 | 1.78 | 1.61 | 5.44 % | 21.2 % |
| c100 | 1.67 | 2.84 | 1.69 | 2.73 | -1.35 % | 3.98 % |
| c170 | 1.88 | 3.40 | 1.73 | 2.75 | 9.23 % | 25.4 % |

**Table 1.2:** Coefficients computed using linear regression – calculated for flow rates in $[m^3/s]$ and pressure drop in $[bar/m]$

pressure drops in e.g. bends are not accounted for. This could explain the more significant gaps observed for $b$ coefficients. In particular, the singular pressure drops at the bottom and top of coaxial heat exchangers may be important to consider since there is a sharp change of diameter.

It is therefore important to understand the geometry of this singularity. The bottom part of the central pipe is shown figure 1.7. In the final installation, the "torpedo weight" is connected to the end of the pipe. The pressure loss takes place due to sudden change of cross-section area and direction. Furthermore, 12 holes can be counted. This number may vary between boreholes. The diameter of each hole is around 10mm.

Local losses are classically modeled via the coefficient $C_0$ using the expression

$$\Delta P = C_0 \frac{\rho v^2}{2} \tag{1.22}$$

In literature there are no tabled values available for geometries similar to the one found in coaxial borehole heat exchangers. The approach adopted for the analysis is therefore utilizing the experimental data available and the theoretical model discussed in the previous section with the objective of isolating the contribution of the local losses. The idea is that the experimental measurements account for all the losses while the theoretical model considers only continuous losses. Given that the theoretical model yields reasonable results, the difference between experimental and theoretical pressure drop should yield a good estimation of the local losses.

Figure 1.8 shows the pressure difference for the coaxial BHEs c100, c170 and c800 as function of the volume flow. It is quite clear that all the curves presents a quadratic behavior

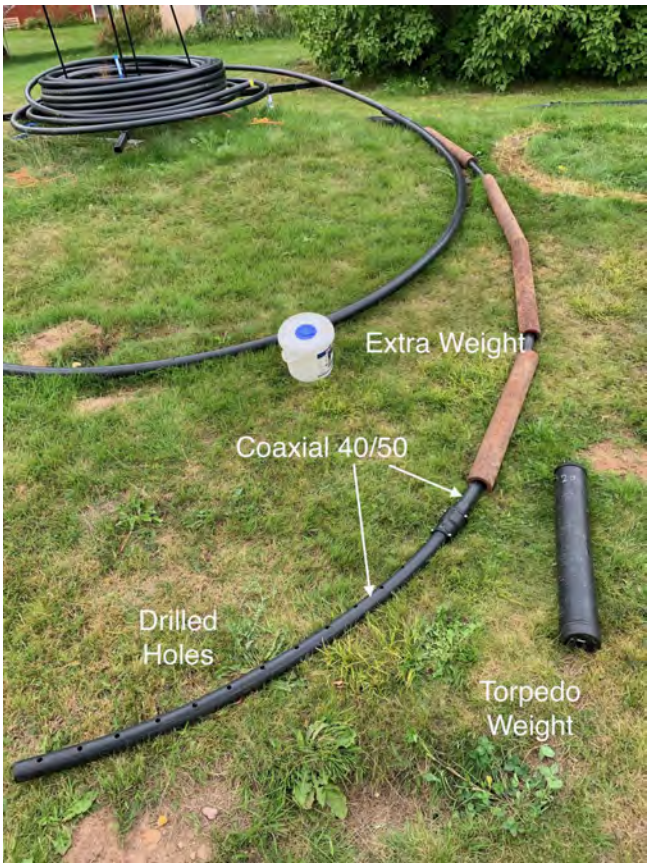


**Figure 1.7:** Picture of the end of the central pipe for the Live-in-Labs system

(excluding the laminar flow transient for c100 and the outlier of c170). To test the quadratic trend in figure 1.9, a regression is performed for the three installations between the quantities $\Delta P_{exp} - \Delta P_{th}$ and $v^2$. The plot shows that regressions based on squared velocities provide a very good fit with the experimental-theoretical difference. Another result is that the best fit for the three curves does not go through the origin. This fact may be explained as a bias in the pressure drop measurement and/or due to laminar-turbulent flow transition. To provide a measure of this potential bias, on the right-hand side of figure 1.9 we highlight the region within $\pm 5\%$ of full-scale reading with respect to the best fit line. Following this idea we can calculate the coefficient $k_1$ in the following expression through linear regression

$$\Delta P_{exp} - \Delta P_{th} = k_1 v_i^2 + k_2 \tag{1.23}$$

and successively determine $C_0$ as $2k_1/\rho$. We might say that $k_2$ models the limitations of the measuring devices or the theory at low flow rates. The results for $C_0$ determined with this methodology are reported in table 1.3. The values of $C_0$ obtained for BHEs c100 and c170 differ significantly although the boreholes have a similar geometry. However, the coefficient per meter ($C_0/L$) for c100 and c170 are very similar (0.52 vs. 0.47, respectively). This suggests that the discrepancy comes from continuous losses rather than singular ones. In other words, the theoretical calculations may underestimate the real pressure drop regardless of singular losses. This is strengthen by the fact that $C_0$ are very high in comparison to common values for diameter reduction and enlargements ( 0.1–1). The value of $C_0$ for $c800$ is on the other hand significantly lower compared to the other two boreholes. If the difference would be due to continuous losses, we may expect $f_i = C_0 \cdot D_{int}/L$ to be similar for all three boreholes but this is not the case for c800. The geometry of $c800$ presents a larger $D_{int}/D_o$ ratio. If

the minor loss is interpreted as a sudden change of flow area, this would result in a lower minor loss compared to $c170$ and $c100$ which could offer an explanation for the observed difference. Without more data, it is hard to conclude as to the exact cause of the discrepancy between theoretical and experimental pressure drop. Results from c100 and c170 suggest that the continuous losses are underestimated but singular losses must play a role as well. If the theoretical calculations are to be used for sizing a circulation pump, it is recommended to increase the internal friction factor $f_i$ by 0.018, which is the value found for the shorter borehole c100 (corresponding to a 45% increase compared to the smooth pipe internal friction factor). Since this coefficient allegedly include singular losses, using for longer boreholes may lead to a slight overestimation of the pressure drop. This may be seen as a safety factor in the pump sizing process.

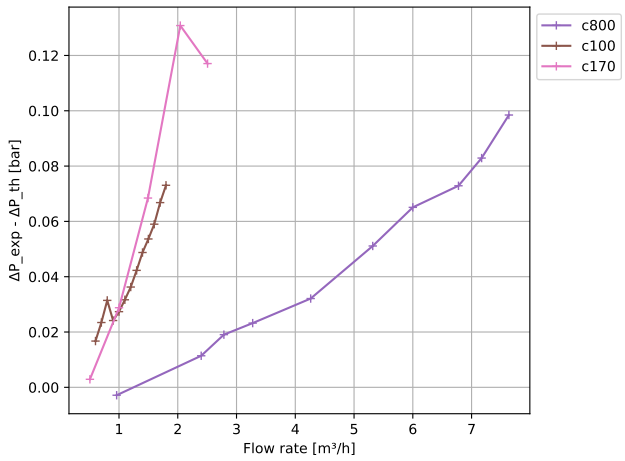


**Figure 1.8:** Difference between measured pressure loss and theoretical pressure loss considering only continuous losses.

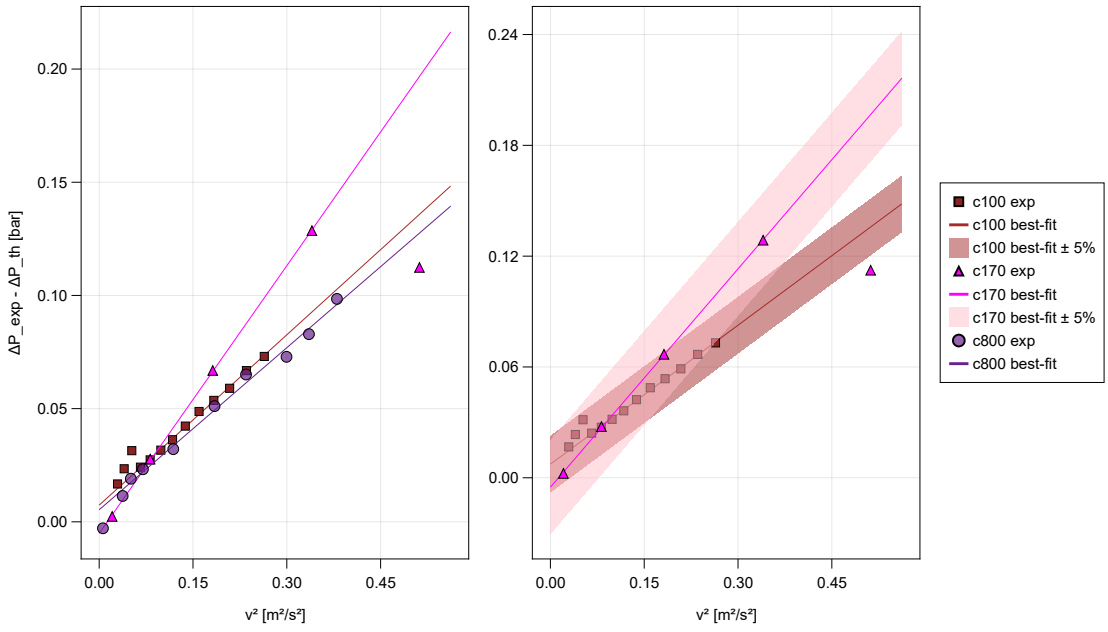


**Figure 1.9:** Difference between experimental and theoretical pressure drop vs velocity $v_{in}^2$

| Borehole | $C_0$ | $D_{int}$ | $D_{out}$ | $D_{int}/D_{ext}$ | $A_{int}/A_{ext}$ |
|---|---|---|---|---|---|
| c100 | 51.8 | 0.0352 | 0.114 | 0.309 | 0.105 |
| c170 | 79.8 | 0.0352 | 0.114 | 0.309 | 0.105 |
| c800 | 47.7 | 0.0662 | 0.150 | 0.441 | 0.260 |

**Table 1.3:** value of $C_0$ and geometrical parameter of the section (with respect to $v_{in}^2$)

### 1.4.2 Summary of the analysis

Figure 1.6 provides an overview of pressure losses for coaxial, single U-pipe and double U-pipe BHEs. The plot leads to a few observations. Double U-pipes have the lowest performance in terms of pressure drops among the design considered even though the flow is distributed over two pipes. This is due to the small diameters used (DN32). Coaxial heat exchangers show better or at least comparable pressure drop when compared to single U-pipes. Among the coaxial boreholes tested we should distinguish between $c800$ which shows a remarkably low pressure drop per meter and $c100$ and $c170$. As pointed out in the previous section such a low pressure drop is the result of more favorable cross-section geometry with a larger outer diameter and higher ratio between inner and outer diameter.

Finally, the difference between theoretical and experimental pressure drop suggests that the theory might underestimate pressure – possibly due to a wrongful smooth pipe assumption or eccentricity of the center pipe. Singular losses at the top and bottom seem to play a role, at least for short boreholes. Fully understanding where the observed difference comes from may lead to improvement in the design of coaxial BHEs.

# Chapter 2

# Thermal Response Tests: theoretical considerations

A key element for optimal design and operation of Ground Source Heat Pump (GSHP) systems is the accurate estimation of the effective ground thermal conductivity ($\lambda^*$) and the effective borehole thermal resistance ($R_b^*$).

The former indeed strongly influences the thermal response of the ground while the latter is an indication of the thermal performance of the Borehole Heat Exchanger (BHE). Both the thermal response of the ground and the thermal performance of the BHE influence the performance of the Ground-Source Heat Pump (GSHP) system. It is thus decisive to accurately estimate these parameters. The state-of-the-art method used to estimate $\lambda^*$ and $R_b^*$ is Thermal Response Testing (TRT).

The TRT method was introduced by Mogensen [16] and it consists in injecting heat in the ground by circulating a fluid inside the BHE. A typical TRT setup is shown in fig.2.1. The temperature of the circulating fluid and injected power are recorded during the test, which usually lasts around 3 days. The parameters $\lambda^*$ and $R_b^*$ can then be estimated by minimizing the Root Mean Square Error (RMSE) or Sum of the Squared Errors (SSE) between the experimental thermal response and the thermal response obtained from a parametrized model (that is the temperature change over time). This is also referred to as inverse modelling because parameters are estimated from data through a model. The parametrized model being used in 90% of TRTs [7] is the Infinite Line Source (ILS) model [4, 8].

$$\bar{T}_f - T_0 = q' \left( R_b^* + \frac{1}{4\pi\lambda^*} E_1 \left( \frac{r_b^2}{4\alpha^* t} \right) \right) \tag{2.1}$$

where

- $\bar{T}_f$ is the inlet-outlet average temperature
- $T_0$ is the initial ground temperature
- $q'$ is the constant injected power per meter of borehole
- $E_1(x)$ is the exponential integral function
- $r_b$ is the borehole radius
- $\alpha^*$ is the effective thermal diffusivity of the ground
- $t$ refers to the amount of time passed since the start of the heat injection

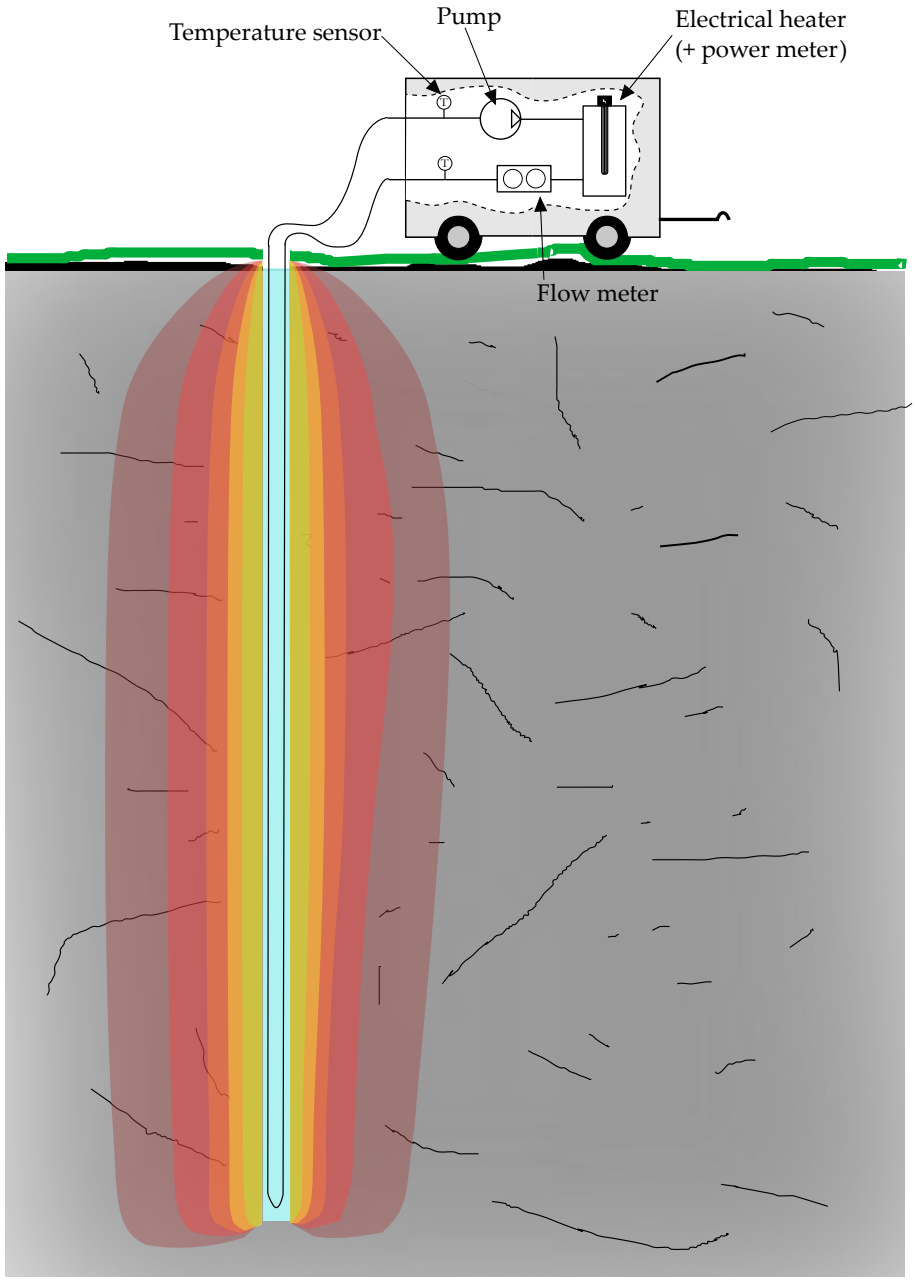


**Figure 2.1:** Typical setup for a Thermal Response Test

For large times ($t > 5r_b^2/\alpha^*$), the exponential integral in eq. 2.1 is often approximated by its first series expansion terms, such that

$$\bar{T}_f(t) - T_0 = q' \left( R_b^* + \frac{1}{4\pi\lambda^*} \left( ln \left( \frac{4\alpha^* t}{r_b^2} \right) - \gamma \right) \right) \tag{2.2}$$

This approximation is convenient since the thermal conductivity and borehole thermal resistance can be determined through a simple linear regression in logarithmic time (given all the other parameters). However, this requires the injected power to be constant over time. In practice, this is hard to achieve but exactly how constant does it need to be in order for eq. 2.2 to be valid? This is what is being investigated in the next section.

## 2.1 Disturbances and validity of the Infinite Line Source approximation

In the previous section, we claimed it is hard to keep the injected power constant. This is also highlighted in the literature, see e.g. [20, 25, 19, 7, 24, 18]. Some examples of injected power and flow rates of commercial and research TRTs are shown in fig.2.2 [3, 15]. While a constant power step is what was strived for in all TRTs except for TRT-B2, it is clear that most tests are far from having a perfectly constant heat injection.

This raise the question: how well does the ILS approximation (eq. 2.2) perform under non-ideal conditions? This was investigated in a paper written as part of this project [11].

Synthetic thermal responses were generated using another, more detailed model than the ILS that can account for short-term transient phenomena inside the borehole [9]. Two types of heat injection profile were used to generate the synthetic thermal responses: a constant profile and a "drifting" profile (see fig. 2.3 and 2.4, respectively). "Drifting" profiles can be more rigorously described as auto-correlated profiles. In some cases, white noise was even added to the true heat injection and temperature signals.

The synthetic TRTs were then interpreted using both the ILS approximation (eq.2.2) and the time-superposed ILS (see e.g. [15]) which can account for variations of injected power.

When applying a noise-free constant heat injection profile, one can observe a difference between the estimated parameters and the true parameters. This is due to the difference in model used for the generation and interpretation of data. This is referred to as "model bias" and is shown in fig.2.3. The figure show the logarithm of SSE (cost function) on the left, the heat injection profile on the top right diagram and the temperature responses on the bottom right. The estimated parameter are shown with marker on the left diagram. Note that "regression" refers to the ILS approximation while "optimization" refers to the time-superposed ILS. In this case, the model bias leads to a difference of thermal conductivity of about 7%. For $R_b$ the difference is about 6 %.

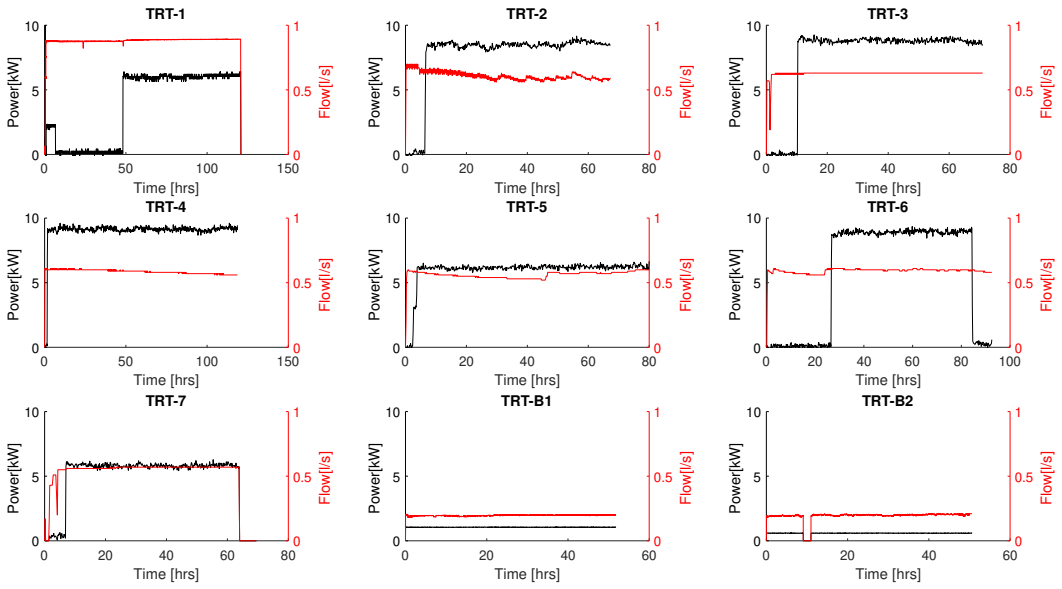


**Figure 2.2:** Examples of injected power and flow rate during commercial (TRT-1 to TRT-7) and research TRTs [3, 15]

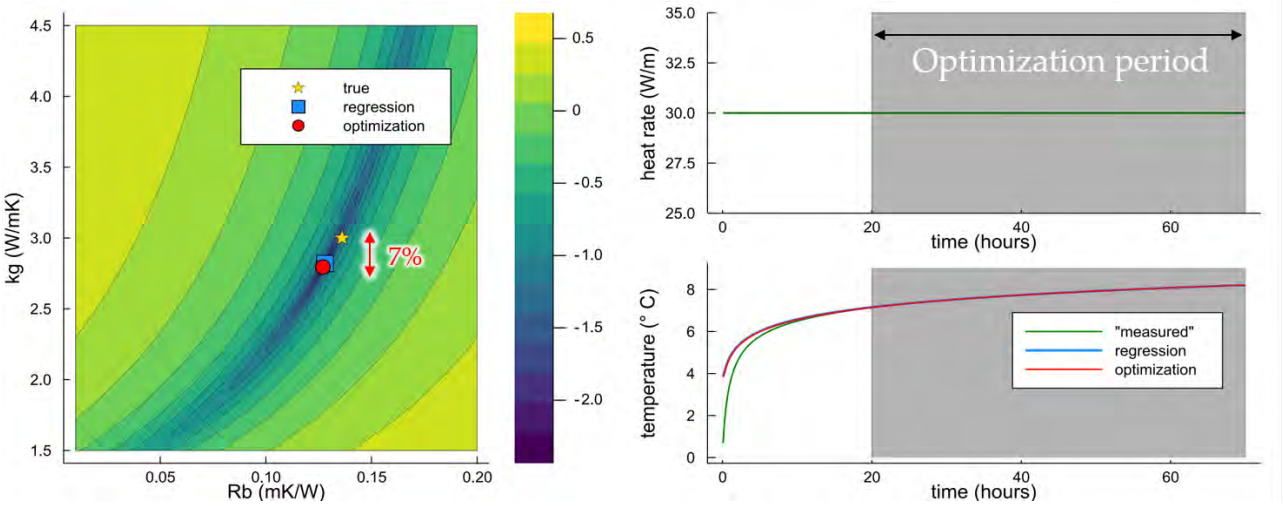


**Figure 2.3:** Parameter estimation for a noise-free constant heat rate with different generation and interpretation models [11]

**Note:** model bias is not specific to the ILS models, every model has its own bias. This reflects the fact that no model can perfectly represent the true behavior of the system. Some models have lower bias than other though.

A second result from this investigation is that the ILS approximation does not perform well if the heat injection profile is drifting in time. This can be seen in fig.2.4 where the difference in thermal conductivity is about 25% between the true value and the value obtained with the ILS approximation. For $R_b$ the difference is about 14 %. Although the drift in the heat injection profile is small (relative standard deviation of about 1.3%), the difference in estimated parameter is relatively large. This suggests that the ILS approximation is not suitable for analyzing TRTs in which the heat injection rate shows some auto-correlation in time. Moreover, the ASHRAE criterion [2] of a maximum relative standard deviation of 1.5% for the application of the ILS approximation should perhaps be revised.

Note that both the heat injection rate and the temperature are corrupted by white noise but this does not significantly affect the results in this case.

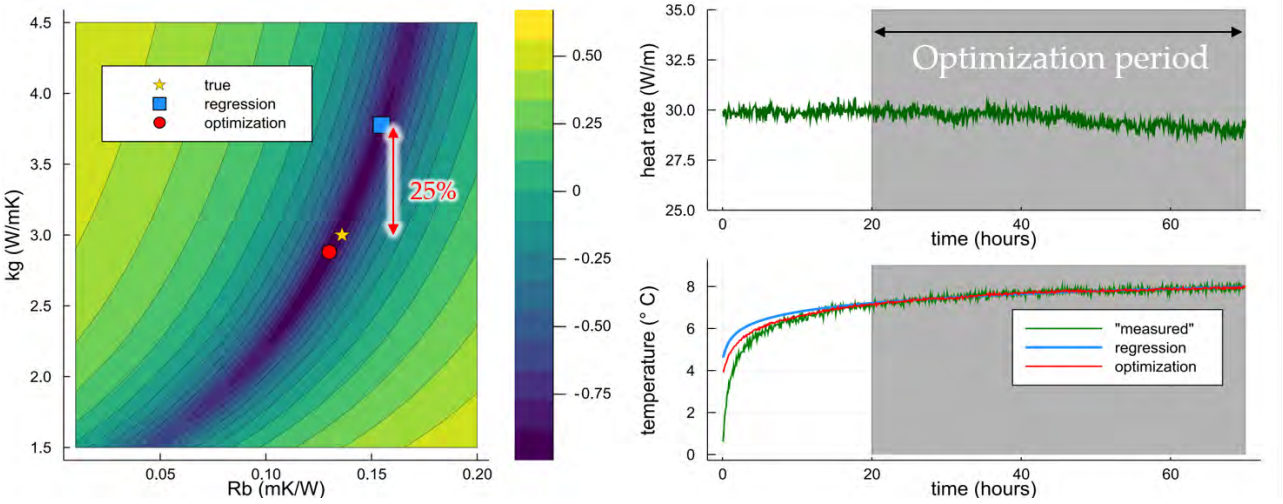


**Figure 2.4:** Parameter estimation for a noisy drifting heat rate with different generation and interpretation models [11]

When a perfect heat injection rate is corrupted by white noise, the ILS approximation performs almost as in the noise-free case. The time-superposed ILS, however, performs worse, meaning that the difference between estimated and true parameters is larger than in the noise-free case.

In all cases, the ILS models appear unable to reproduce the same short-term thermal behavior of the Javed and Claesson [9] model. Now, this could simply be a modeling discrepancy since these are synthetic TRTs but there are real examples where the same phenomenon is shown (e.g. [14, 15, 3, 5]). The short-term thermal behavior of the BHE is of importance for the operation of GSHP which may have relatively short operation cycles.

Additionally, the ILS models could have a large model bias if many of the assumptions are violated. For instance, there could be groundwater flow, the ground could be heterogeneous or the borehole tilted.

More fundamentally, it is intricate to know how large bias a given model have for a certain BHE. Large bias can lead to erroneous parameter estimation which in turn have consequences for the design and operation of the GSHP system. Understanding how large bias a given model has is very valuable but it requires knowledge about the true thermal behavior of the BHE. So, how can this true behavior be identified? The fields of system identification, machine learning and statistical leaning proposes methods to derive a system behavior solely from data. The application of some of these methods to TRT is investigated in the next sections.

## 2.2 New methodologies for TRTs

The goal of a TRT is to obtain a parametric model of the BHE based on field measurement. As seen above, the parametric model of choice for TRT is the ILS, which is the solution to the heat transfer by conduction partial differential equation in an infinite homogeneous media surrounding the borehole modeled as infinite line injecting a step of heat. The linearity of the heat equation enables using this solution as a building block to model the effect of generic load applied to the line source. The superposition in time is obtained through the convolution operation.

$$\bar{T}_f(t) - T_0 = \frac{\partial q'(t)}{\partial t} * g(t) \tag{2.3}$$

where $g(t)$ is the step response function. Systems with this property are called *linear time invariant* (LTI). In such systems the response function $g(t)$ give the complete description of the dynamics of the system. Although the ILS model adopted is a valid choice based on the physics of the problem, the phenomenon measured in the real system is often more complicated and might have specific features for each single installation. A simple example, is the characterization of the short term dynamics (minutes to hours) which is not feasible through ILS.

A methodology that could be used to address this problem is relaxing the hypothesis that we make on the model but still consider that our system behaves as an LTI system. Instead of searching the parameters yielding the best-fit between the model and the data, we are looking for the *function $g$ itself*. No constrains on the shape of the function are imposed with the exception of constraints on its smoothness, which is a property that we expect in this physical system. These family of methodologies are also known is literature as non-parametric models, and are used in the machine learning and statistical learning literature.

### 2.2.1 Spectral methods

It is often convenient to analyze LTI systems in the frequency domain and one of the reason is the ease and efficiency in performing the convolution operation. Convolution between two functions $u$ and $v$ can be computed in the frequency domain as the product of their Fourier Transform $\tilde{u}$ and $\tilde{v}$ given that their transform exist.

In the previous section we have seen the central role of convolution to model heat transfer in borehole systems. In addition to the formulation of equation 2.3, this phenomena can be expressed as a convolution involving the impulse response $h(t) = \dot{g}(t)$ with either of the formulations provided in equation 2.4 and equation 2.5.

$$\Delta T(t) = \bar{T}_f(t) - T_0 = q'(t) * h(t) \tag{2.4}$$

$$\Delta \dot{T}(t) = \dot{\bar{T}}_f(t) = \dot{q}'(t) * h(t) \tag{2.5}$$

The impulse response can be therefore computed in the frequency domain as, for instance

$$\widetilde{h}(\xi) = \frac{\widetilde{\dot{T}_f}(\xi)}{\widetilde{\dot{q}'}(\xi)} \tag{2.6}$$

This operation, also known as inverse filtering is an example of a non-parametric approach for the estimation of the response of the system.

In practice we operate with discrete samples and the signals are sampled during a finite time frame. The dual operation of the Fourier Transform for discrete time is the discrete Fourier Transform (DFT). Equation 2.6 can be therefore formulated in terms of DFT [17].

$$\mathcal{F}(h(t)) = \frac{\mathcal{F}(\dot{\bar{T}}_f(t))}{\mathcal{F}(\dot{q}'(t))} \tag{2.7}$$

While there is apparently no big difference between the continuous and the discrete time case, there are some important facts that have a great impact. In particular, signal that are bounded in time are unbounded in their frequency representation and vice-versa. This is very important since every signal that we sample in reality is sampled during a finite time-frame and as a result an infinite number of frequencies is required to represent it. For this reason, the Discrete Fourier Transform of the input signal 2.7 will have some component at all frequencies no matter the choice of input signal $\dot{q}'$. It is therefore important to make sure that our input signal has high level of excitation at all frequencies to avoid having very small number at the denominator yielding to errors in the estimation.

A possible solution to this problem is forcing $\mathcal{F}(h(t))$ to 0 for all the frequencies where the DFT of the input signal has a modulus below a given tolerance. This approach, known as pseudo inverse filtering, yields to a biased estimation since we are ignoring a portion of the energy in the power spectrum of the input signal.

Another issue that affects spectral methods is the so-called transient error or *spectral leakage*. This kind of error appears when using a finite number of data to represent non-periodic input signal. As a result additional terms appears in the frequency. Traditionally an estimate is obtained by smoothing the raw DFT estimate. Other more sophisticated method such as *windowing* and *Local Polynomial Method* (LPM) have been introduced to reduce the effect of *frequency leakage* on the estimation. The first one consist in convolving our data with a suitable window that reduce the effect of leakage, while the latter one consists in an actual estimation of the *leakage* and has proven to be superior in terms of mean square error compare to other traditional smoothing methods.

### 2.2.2 Regularized Least-Square

The continuous time problem of equation 2.4 and 2.5 can be expressed in discrete time form.

$$\Delta T(t_n) = (q' * h)(t_n) = \sum_{k=1}^{n} q'(t_n - t_k)\, h(t_k) \tag{2.8}$$

A time-domain non-parametric estimation approach is obtained by expressing the problem of equation 2.8 in matrix form.

$$\mathbf{\Delta T} = \begin{bmatrix} \Delta T(t_1) \\ \Delta T(t_2) \\ \vdots \\ \Delta T(t_n) \end{bmatrix} = \begin{bmatrix} q'(t_1) & 0 & \cdots & 0 \\ q'(t_2) & q'(t_1) & \cdots & 0 \\ \vdots & \vdots & \ddots & \vdots \\ q'(t_n) & q'(t_{n-1}) & \cdots & q'(t_1) \end{bmatrix} \begin{bmatrix} h(t_1) \\ h(t_2) \\ \vdots \\ h(t_n) \end{bmatrix} = \mathbf{Q}\ \mathbf{h} \tag{2.9}$$

At first glance, the values of $h(t_1), h(t_2), \cdots, h(t_n)$ could be obtained by simply inverting the lower triangular matrix of equation 2.9. In reality the matrix $\mathbf{Q}$ is often badly conditioned and the problem is ill-posed. This means, that matrix might be non-invertible, and if invertible, the values of $\mathbf{h}$ will be very sensitive on variation of the temperature $\mathbf{\Delta T}$. This is a problem since our measurements might be affected by noise and we might have access to a noisy version of the data $\mathbf{\Delta T_e}$

$$\mathbf{\Delta T_e} = \mathbf{Q}\ \mathbf{h} + \mathbf{e} \tag{2.10}$$

where $\mathbf{e}$ is a vector containing the measurement noise $e_1, e_2, \cdots e_n$ for each time sampled. The problem is therefore reformulated into the minimization problem of the square loss of the residual $e$

$$\underset{h}{\operatorname{argmin}} \ \|\mathbf{\Delta T_e} - \mathbf{Q}\ \mathbf{h}\|^2 \tag{2.11}$$

This is a linear regression problem which has the well know analytical solution [6]

$$\widehat{\mathbf{h}} = (\mathbf{Q}^T\mathbf{Q})^{-1}\mathbf{Q}^T\ \mathbf{\Delta T_e} \tag{2.12}$$

where $\widehat{\mathbf{h}}$ is an estimate of the impulse response. Although this method will provide us with a solution, the result will be still highly affected by noise due to the bad conditioning of the the matrix $\mathbf{Q}$. A classical approach to improve the robustness of the estimation is Tikhonov regularization. This method consists in introducing a term $\mathrm{R}(\mathbf{h})$ in the minimization problem which penalizes function that do not have certain characteristics in terms of regularity. This effectively reduce the size of the functional space $\mathcal{H}$ of possible solutions $\widehat{\mathbf{h}}$ to "simple" functions. The new problem is a perturbed version of the minimization of the empirical loss (equation 2.11) and encode two facts: the first one is that we do not trust completely our data because they might be affected by noise, and the second one is that we want to incorporate our knowledge regarding the expected smoothness of the solution in the estimated function. The amount regularization required is controlled by the parameter $\lambda$.

$$\underset{\mathbf{h}\in\mathcal{H}}{\operatorname{argmin}} \ \|\mathbf{\Delta T_e} - \mathbf{Q}\ \mathbf{h}\|^2 + \lambda\ \mathrm{R}(\mathbf{h}) \tag{2.13}$$

The trick is encoding the notion of smoothness or simplicity of the functional space $\mathcal{H}$ in the function $\mathrm{R}(\mathbf{h})$ and decide how we trade-off regularization and empirical risk term. Example of regularizers are for example the euclidian norm of h or the norm of the derivative of h. It is possible to show that given a proper choice of $\mathrm{R}(\mathbf{h})$ , the new problem 2.13 is well-conditioned and hence yield results that are less sensitive to noisy data. A neat way to

achieve the objective of encoding the functional space of function can be obtained through so-called Kernel methods. We partnered with Riccardo Sven Risuleo, postdoctoral researcher on machine learning and system identification at Uppsala University and KTH to choose the appropriate Kernel for the application. Details on the theoretical basis of the method will be published in a future publication. Results of the application of kernel methods and spectral methods on experimental data are presented in chapter 4.

### 2.2.3 Parametric estimation

Some attempts to identify parametric black-box models were undertaken and are presented in details in part A.6 of appendix A. The types of model that were identified are: Finite Impulse Response (FIR), transfer function (G), Auto-Regressive Moving Average with Extra Input (ARMAX), Box-Jenkins and Output Error. The models were identified using the system identification toolbox of Matlab a real TRT with a training and validation set.

An attempt to reproduce a second TRT, performed in the same borehole, was then realized. This is shown in fig. 2.5. The transfer function models $G_1$ and $G_2$, as well as the $ARX$ model manage fairly well to reproduce the second TRT until about 70 hours ($2.5 \cdot 10^5$ $s$) but then all models seem to converge to some steady-state value while the measured temperature keeps increasing.

The three models mentioned above manage well to reproduce the short-term thermal behavior of the thermal response. In particular, the ARX model succeeds in reproducing the short-term thermal behavior of the second power step (visible in the temperature response at about $1.2 \cdot 10^5$ $s$).

All identified models were also used to estimate the thermal conductivity and borehole thermal resistance by using the found unit step response and applying the ILS approximation method (eq.2.2). The results are shown in fig.2.6 where "ILS (Newton-Raphson)" refers to the time-superposed ILS estimation method.

While the identification of parametric models show some interesting features, more work and research needs to be perform in order to have fully functional methods.

### 2.2.4 Work under publication process

**Measurement noise on the input creates a bias in the parameter estimation**

In the field of system identification, it is a well-known fact that measurement noise on the input (here the power) will lead to biased estimation when the SSE or MSE is used as cost function. TRTs are no exception to this and this was demonstrated analytically and tested numerically. In other words, when the measured power is corrupted by noise, the set of parameters that minimize the MSE will be biased: it does not correspond to the set of true parameters even when the interpretation model corresponds to the true system (i.e. there is no model bias). Negative biases as low as -0.25 W/(m·K) (6.2%) and -$5.8 \cdot 10^{-3}$ m·K/W (2.3 %) are observed for the thermal conductivity and borehole thermal resistance estimates, respectively.

In addition to these biases, the parameter estimation features a stochastic behavior due to randomness of measurement noises. Even under the exact same test conditions, the cost function will slightly differ due to random noise components. This means that for two exactly similar tests (except for the random noise components), the cost function of each test will be different, with minimum at different locations in the parameter space. In turn, this means

that the estimated parameters will be different for the two TRTs. The magnitude of these variations of the cost function due to random noise components can be understood by looking at the standard deviation of the estimates obtained through different realizations of the same test. Population of estimates with standard deviations as high as 0.28 W/(m·K) (7.1%) and $6.4{\cdot}10^{-3}$ m·K/W (2.6 %) were found in this study.

A general trend is that the standard deviation and bias are higher for higher parameter values, with a particular dependency on thermal conductivity. To reduce the bias and spread of the estimates, having larger heat rate per meter appears to be a good strategy. Having a higher sampling frequency and/or longer tests might help reducing the spread of the estimates only. Although the bias and distribution of the estimates might not be an issue under some conditions, it is important to be aware of this extra source of uncertainty in the estimation, on top of other sources like model bias.

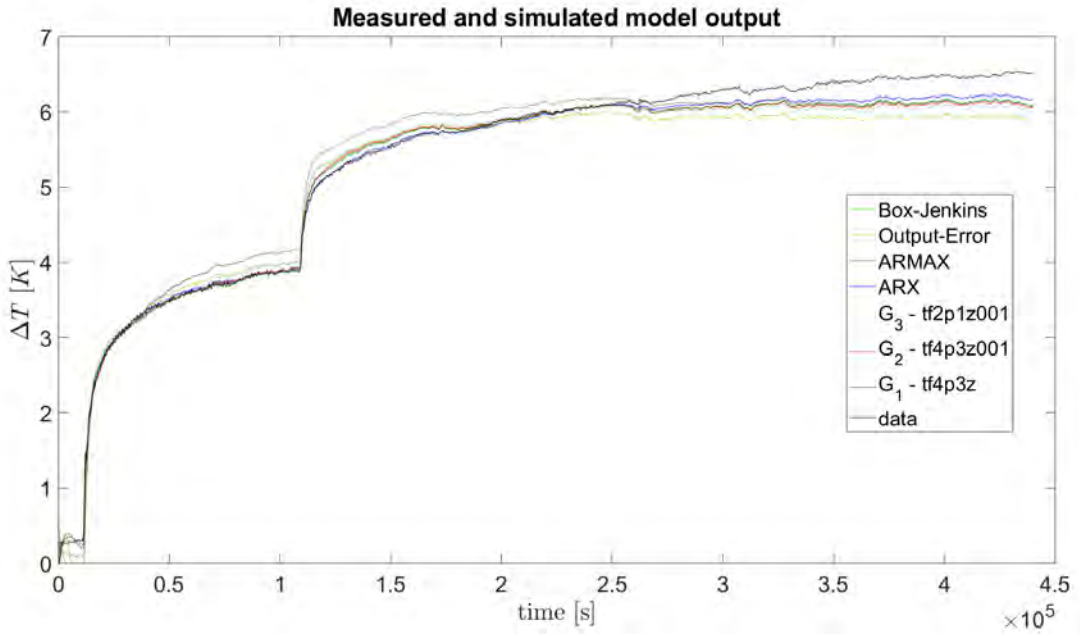


**Figure 2.5:** Reproduction of a TRT with models trained on a previous TRT in the same borehole

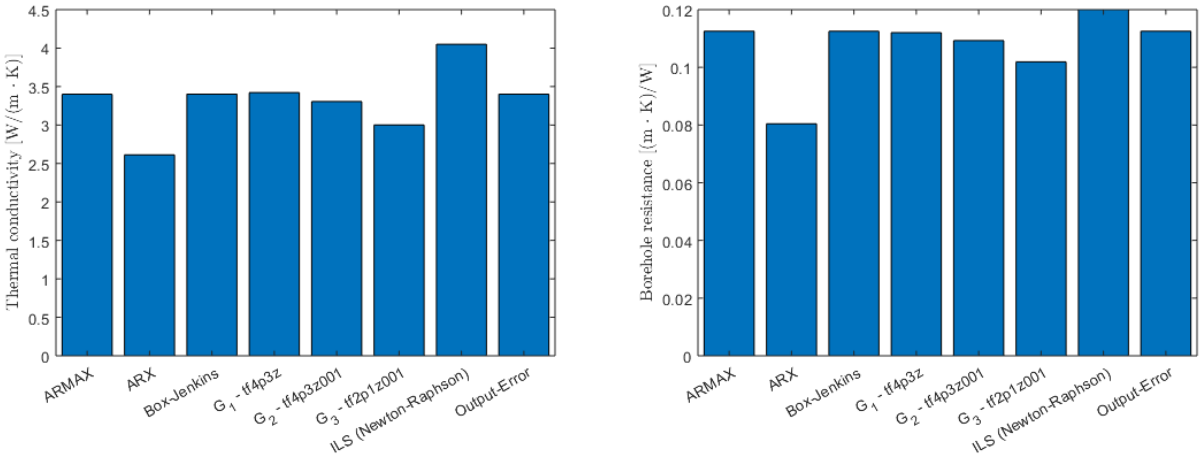


**(a)** Thermal conductivity

**(b)** Borehole thermal resistance

**Figure 2.6:** Estimated parameters for the first TRT for different models

# Chapter 3

# Test rig setup

In order to test the ideas described in chapter 2 a test rig providing the required flexibility in terms of thermal power exchange with the borehole was designed and built. The test rig is strategically located at Live-in Lab, a lab dedicated to cooperation between researchers and industry for accelerating research on the built environment. Figure 3.1 shows the facility with the test rig apparatus. The system comprehend one heat pump, piping system, valves, two heat exchangers, one water tank, sensing devices and control system. This test rig is connected to a coaxial heat exchanger that is dedicated to the research project (figure 3.2). A schematic of the test rig is given in figure 3.3. The system is designed to enable the heat pump to operate both for extraction and injection and to be able to modulate the power rate in a controlled manner. The following sections provides a descriptions of the components, the operating modes, the sensing devices, and the control system.

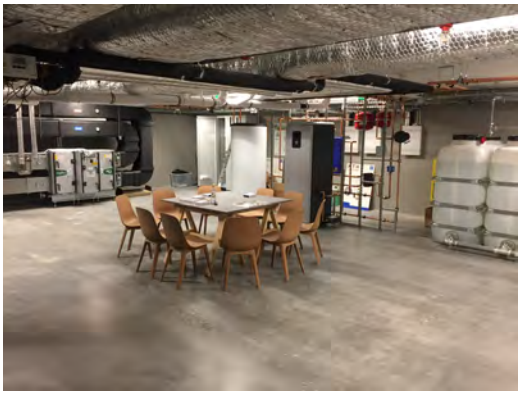

**Figure 3.1:** KTH Live-in labs

**Figure 3.2:** Top of the coaxial borehole

## 3.1 Components description

**HEAT PUMP** - The heat pump used is the commercial unit Diplomat Inverter M from THERMIA. It is a modular water to water HP of a nominal power of 12 KW, operating with R410A. It can run on 9 different gears, each one corresponding to a compressor speed. The HP can communicate with external devices using ModBusRTU protocol. It then acts as a "slave", which means it listens to orders and sends back answers to the master depending on the message.

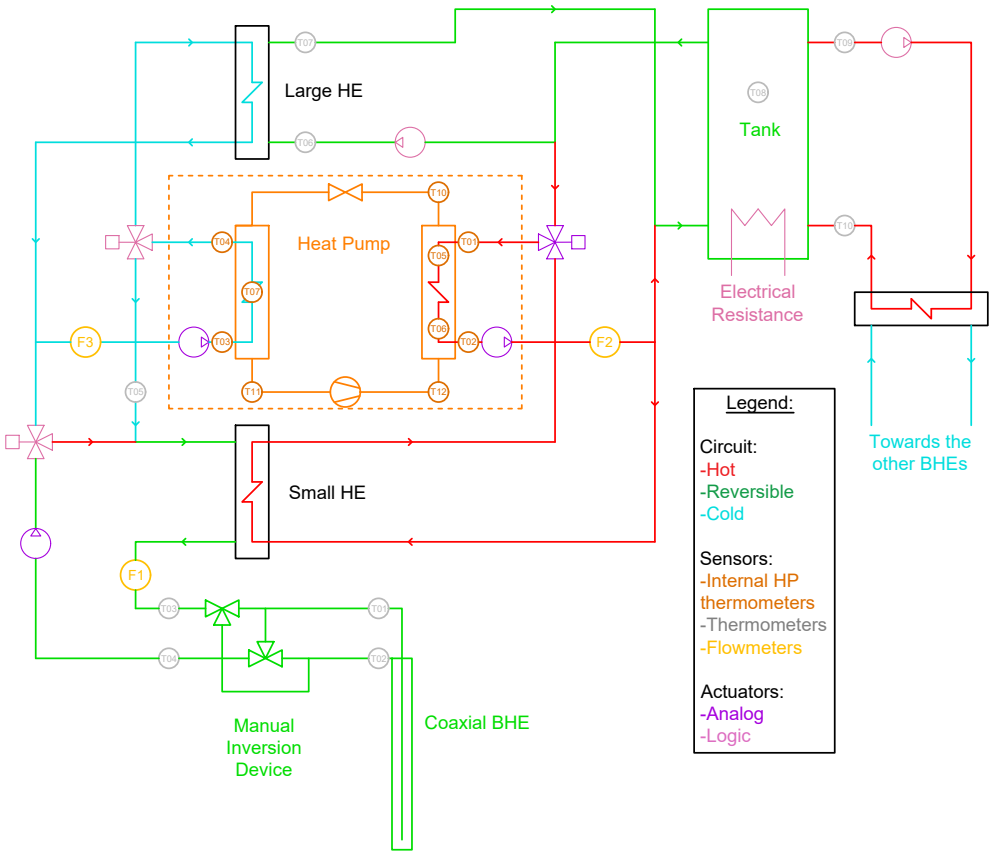


**Figure 3.3:** Hydraulic circuit

**COAXIAL BHE** - The BHE is the 100 $m$ coaxial pipe utilized in the pressure drop analysis presented in chapter 1. The BHE is made of two main elements. The first one is a central rigid tube made of High Density PolyEthylene (HDPE) with a double wall layer that traps air in order to thermally insulate the downward and upward flows, minimizing their mutual heat exchange (also known as "thermal shunt"). The second one is an outer membrane, so called Energy Capsule (EC), which is kept in direct contact with the BHE's wall by the static pressure.

**PUMPS** - The ciculation pump in the borehole loop is a Magna 3 from Grundfos. It is a variable speed pump and is controlled by a $0-10$ $V$ signal. Two pumps, one on the evaporator circuit and one on the condenser circuit came stock with the heat pump. A fourth pump from Wilo was installed in the tank loop. This pump is on/off operated via relay.

**VALVES** - There are two different Three Way Valve (TWV) actuators in the system: two "All Or Nothing" (AON) and one proportional actuator. These are displayed respectively on the left-hand side and on the right-hand side of the scheme in figure 3.3. The AON actuators are controlled directly by their power supply ($230VAC$), while the proportional actuator is controlled through the analog signal 0-10V DC. In addition to the motorized valves, two manually operated valves have been installed at the inlet of the borehole. These valves enables feeding the borehole both from the inner pipe or from the annulus.

**TANK** - A 1000 liters tank from THERMIA is used as a heat source or heat sink in the system. The main goal of the tank is reducing the amount of waste heat generated during the testing

operation. The design idea consists in storing sensible heat in the tank and use it for the needs of the building. The tank is equipped with an electrical resistance. This is utilized to prevent freezing in the tank during injection tests.

**HEAT EXCHANGERS** - Two heat exchangers, labeled as *small HE* and *large HE* in figure 3.3, are installed in the system. The first one enables feeding condenser heating power to the borehole loop while the latter one is used to feed evaporator cooling power to the tank loop.

## 3.2 Sensors

**TEMPERATURE SENSORS** - Temperature is measured at strategic points of the system using pt1000 temperature sensors. The sensors are located inside thermal pockets filled with thermal paste in order to minimize their reaction time as well as their systematic bias (due to a non-zero thermal resistance). The electrical resistance of such component vary with temperature. This resistance can be measured and a know correlation for the conversion into temperature in $0\ ^{\circ}C$. pt1000 are calibrated to have a resistance of $1000\ \Omega$ at $0\ ^{\circ}C$. The pt1000 sensors used in the current project are sensors of class A. The tolerance on the resistance corresponds to $0.15 + 0.002|t|\ [^{\circ}C]$ with $t$ the real temperature in Celsius.

**FLOW METERS** - The three flow meters used are RBEF-E Mini Magnetic Inductive flow meters. This device produces a $4 - 20\ mA$ analog output. The advantages of such flow meters are the near absence of intrinsic pressure drop (they contain no moving part) and the fact that they are programmable. For instance, the flow corresponding to $20\ mA$ can be modified, as well as the fluid density.

## 3.3 Control system

As described in the previous section the system comprehend a variety of sensing devices and actuators. These devices are operating with analog signals such as 0-10V or 4-20 mA, but also with the digital signal MODBUS RTU. In order to handle all these type of signals a Bekhoff PLC unit was used. The Beckhoff system is modular and can be customized to handle the kind of input/output required. The PLC can be used as a standalone system to control all the units and record data. This setup requires the programming of all the operation via the proprietary software TWINCAT3. To achieve more flexibility in the programming a raspberry PI unit running python was used as a controlling device and the PLC unit was used as an interface to manage the I/O communication. This setup introduced some latency, but the gained ease of use and the ability to use python libraries in the control algorithm outweighted the disadvantages. In the control program, the user can assign a time dependent set curve for the heat injected. The set-point is achieved by operating a single actuator, e.g. the proportional three way valve controlling the amount of shunt, by means of a virtual PID. The PID was tuned using experimental data. Details on the control implementation and tuning can be found in the master's thesis by Vautrin [22].

## 3.4 Operating mode

### 3.4.1 Injection mode

In injection mode the operational scheme described in figure 3.3 can be simplified to the one of figure 3.4. The ground is used as a heat sink from the HP's point of view and the tank water as a heat source. This type of test implies a cooling of the tank. This effect is not desirable, if the cooling load cannot be dissipated towards the outdoor environment, since it may cause freezing and also make the control much more challenging. For these reasons, an electrical resistance was installed. In addition, it is essential to control the circulation pump between the tank and the *Large Heat Exchanger* in such a way that the evaporator doesn't become too hot risking to approach the heat pump operational limits causing the shutdown of the unit.

### 3.4.2 Extraction mode

In the extraction mode (figure 3.5), the ground is, this time, used as a heat source (which is the case in heating-dominated climates like Sweden). Here, the heat is transported from the BHE, passes into the HP and goes into the tank. In this configuration, the tank heats up. Similarly to the injection case, temperature stability is desirable from a control perspective. For this reason, another heat exchanger is required to dump excess heat from the water tank. A heat exchanger was set up to dump the heat in the circuit connected to a borehole field of 11 boreholes which is providing heat to 3 student houses. This design allows effectively to use the heat generated during test to recharge the ground. Unfortunately the installation of this component took place in a late stage of the project and it was not possible to run extraction tests. Yet, this mode could be tested in future work.

## 3.5 The test rig implementation journey

The overall process, from the concept, to the construction to the actual operation of the test rig was a journey. In this section we acknowledge the work done by each person that actively participate to achieve this goal.

The test rig design was designed by Willem Mazzotti and Alberto Lazzarotto. The assembly of the unit was partly performed by contractors but a significant part of the work was done by Adrien Vautrin, Willem Mazzotti and Alberto Lazzarotto. The installation and calibration of the temperature sensors was performed by Adrien Vautrin and Willem Mazzotti. The set-up of the control unit and connection to all the sensing devices and actuators was performed by Adrien Vautrin. The implementation of the control algorithm was performed by Adrien Vautrin and Thierry Richert. Moreover, Jonas Anun Vogel, director of the Live-in Lab facility provided support along the journey, an was a key figure for the success of the implementation of the test-rig.

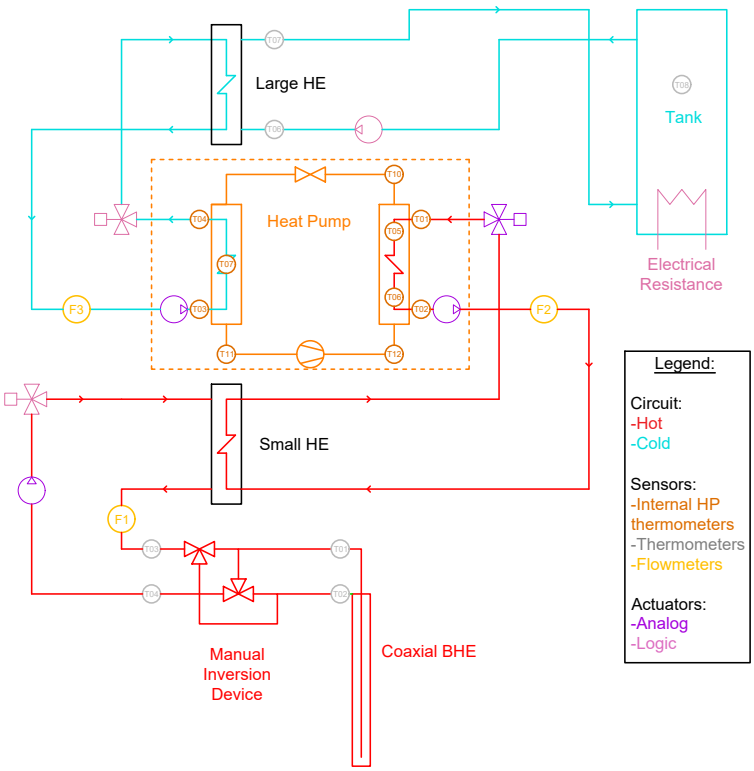


**Figure 3.4:** Pure injection

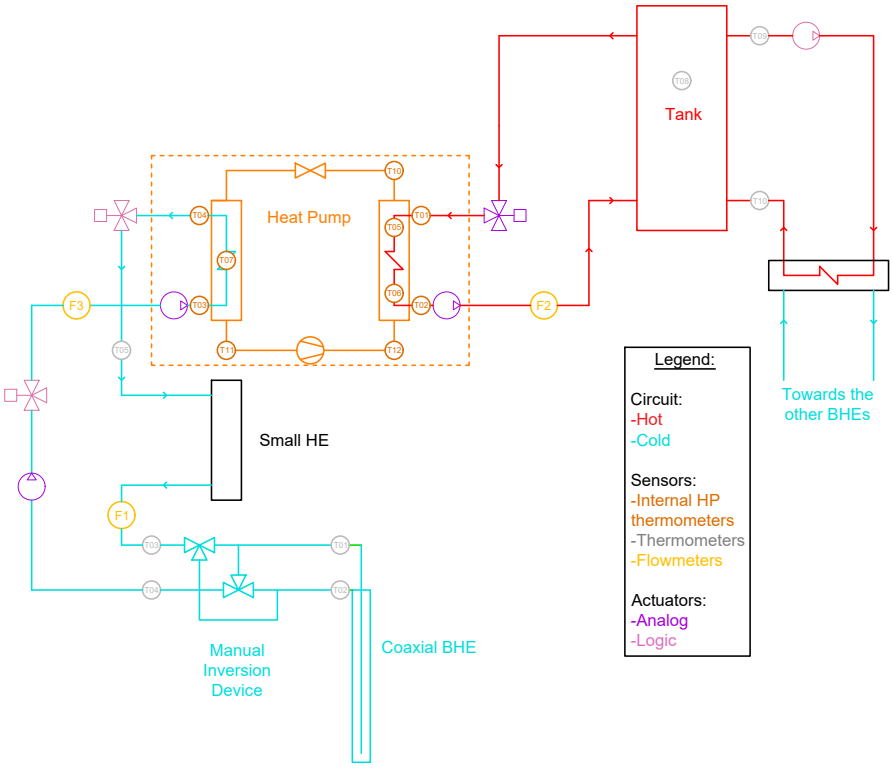


**Figure 3.5:** Pure extraction

# Chapter 4

# Testing and analysis

In this chapter we present the results of four tests carried out at the Live-in Lab facility and their analysis based on the theory discussed in chapter 2. Figure 4.1 shows the plots of heat injected and inlet/outlet fluid temperature in the borehole loop for the four datasets. Each dataset correspond to one test labeled by signal type, and flow. The tests were performed for a time-span between 50 and 100 hours. Two signal types were utilized for the input signal, the error function (erf) and the multi-level pseudo random signal (mlprs). The first signal resemble a step function while the latter signal is very irregular and has the benefit of triggering multiple transients during a single test. The tests were performed at two flow-rates 1.2 $m^3/s$ and 0.8 $m^3/s$. These datasets are utilized for response identification and validation of the model.

## 4.1 Model identification

In the identification phase the datasets were utilized to characterize the temperature response of the borehole system. Both spectral methods and kernel methods as introduced in chapter 2. Each of the four datasets was utilized for learning with both methods therefore a total of 8 models were produced.

For spectral methods it was found that it was effective to determine the impulse response as a transfer function between the derivative of the load injected and the derivative of the temperature as expressed in equation 2.5. This could be the result of a more even spectrum in the the signal $\dot{q}$ as compared to the signal $q$. The spectral method utilized for this experiment is quite basic and does not take into account of phenomena such as spectral leakages. Smoothing of the raw frequency of the DFT of the transfer function $\widetilde{h}$ was applied. The amount of smoothing is effectively a regularizer and control the complexity of the function estimated but introduced bias in the estimation. The tuning of the regularization was done for each training-set by experimenting with different parameters values of smoothing and selecting the one yielding the best match between estimated temperature and measured temperature.

The estimated function $\widehat{h}$ and $\widehat{g}$ are plotted in figure 4.2. Only the 3 models generated with dataset1, dataset2 and dataset4 were kept. The methodology applied to dataset 3 did not provide meaningful result and was discarded. Model1 shows a good fit over the whole time-frame of the test and a low bias, while model2 and model 4 have a good fit only in the initial part of the test and then diverge.

For the kernel-method the estimation was done by solving the problem of equation 2.4. Also in this case the regularization was tuned to match estimation with measured data. The resulting models are showed in figure 4.3. All the models produced gave a good match

between measured temperature and model temperature for the training set.

## 4.2 Validation

In the validation phase we take our identified models and we test them on new unseen datasets to measure their ability of providing a reliable prediction. Each model was generated using a single dataset. This means that other three datasets are available for testing. The testing consists in comparing estimated temperature with measured temperature. The estimated temperature $T_m$ is calculated via convolution of the step response of each model and the derivative of the load as illustrated in chapter 2. This procedure have been performed for each dataset and the results and are shown in figure 4.4, 4.5, 4.6, and 4.7. The plots shows that also on unseen data the results produced with any of the model tested perform well in the initial phase of the transient. For medium to long time frames, models 2 and 4 obtained with spectral methods are the one showing the largest bias. Such bias might be reduced by utilizing more advanced spectral methods addressing the issue of spectral leakage. The models produced with kernel-methods produced more robust results over a larger time-range covering almost the full length of the experiments performed.

These results show that using non-parametric models for the prediction of short time response-function is a viable methodology to accurately model the real behavior of the system. It is important to notice that a good estimate of the response was obtained both from the classic step signals but also from more complicated signals such as mlprs. This is an important result because it shows that it is not necessary to have access to a long continuous tests to produce useful estimate. This is especially true when it comes to short-term responses that are very relevant for the design and optimization of control strategies.

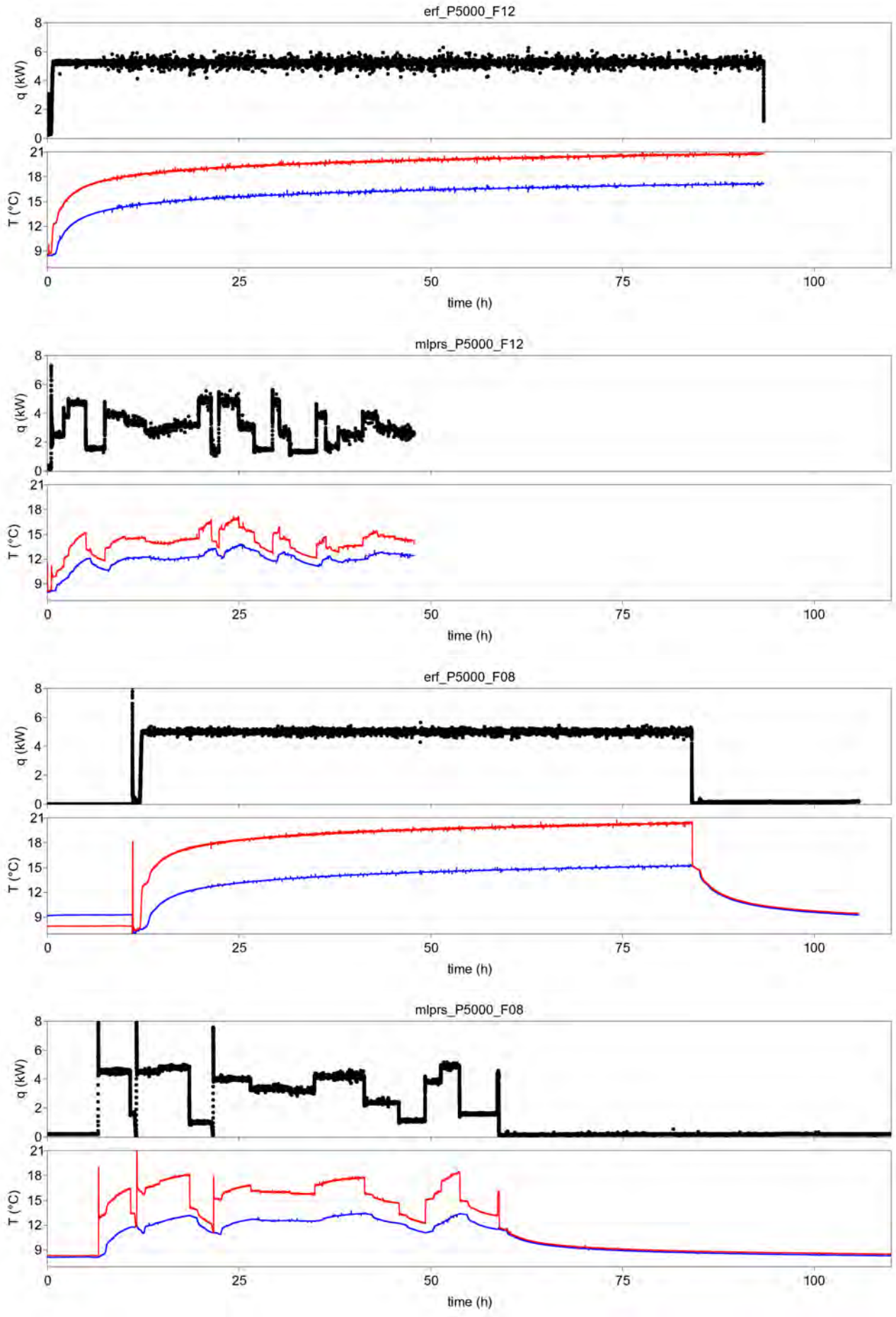


**Figure 4.1:** datasets plot

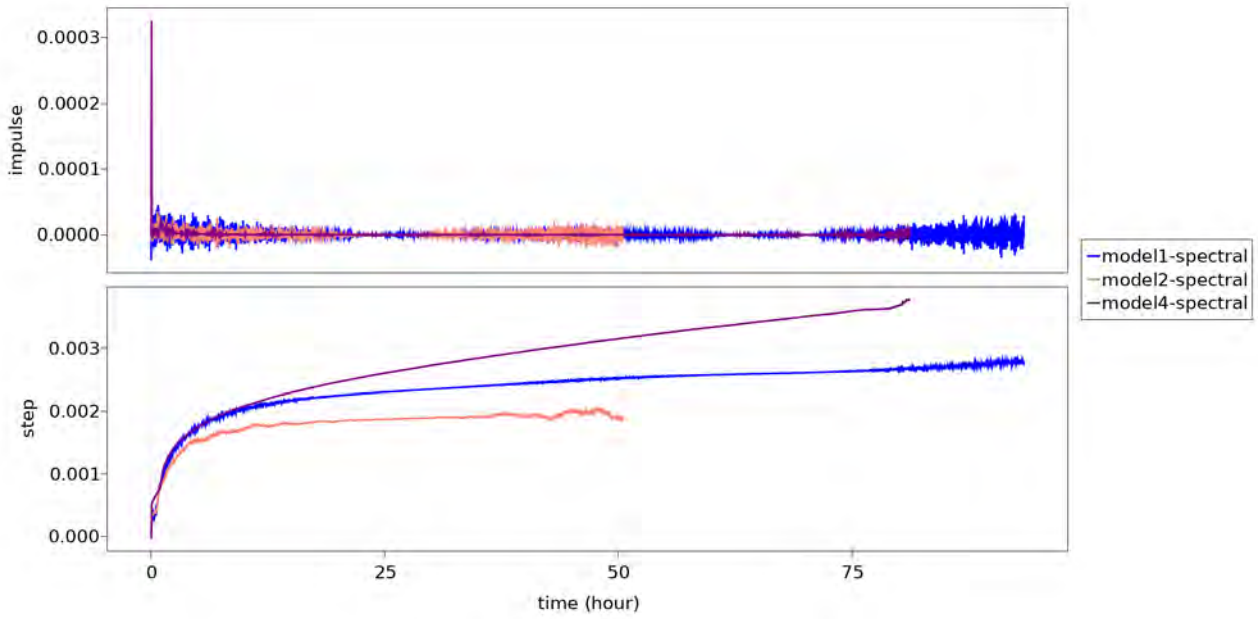


**Figure 4.2:** Impulse response and step response obtained using spectral methods

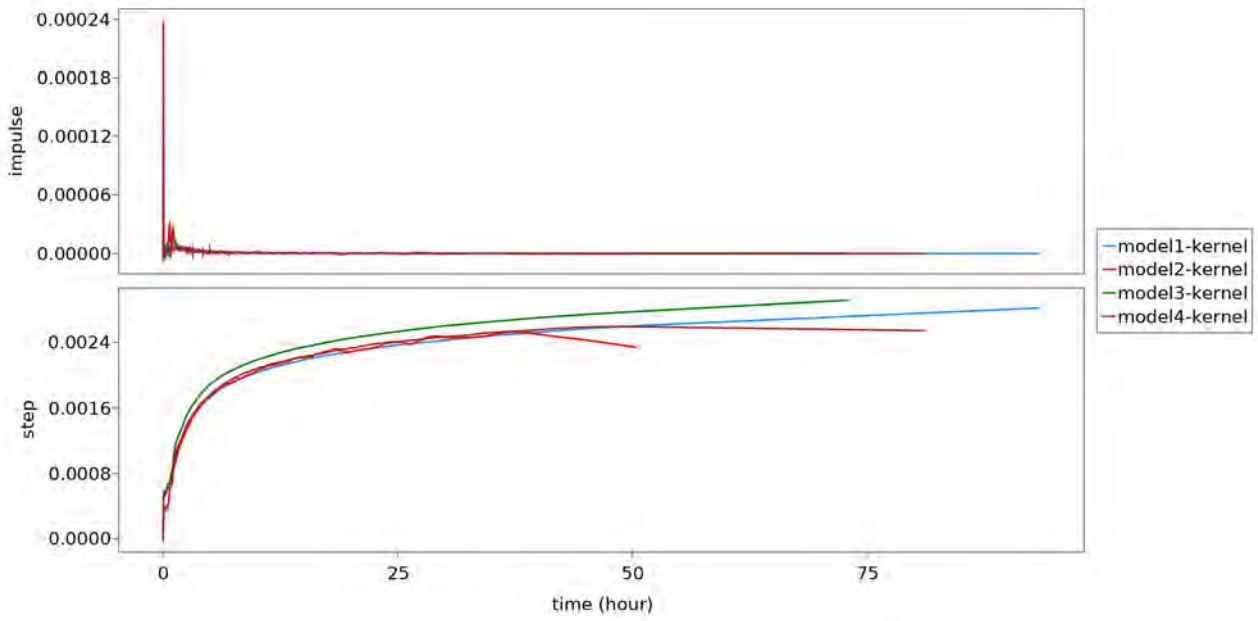


**Figure 4.3:** identification kernel

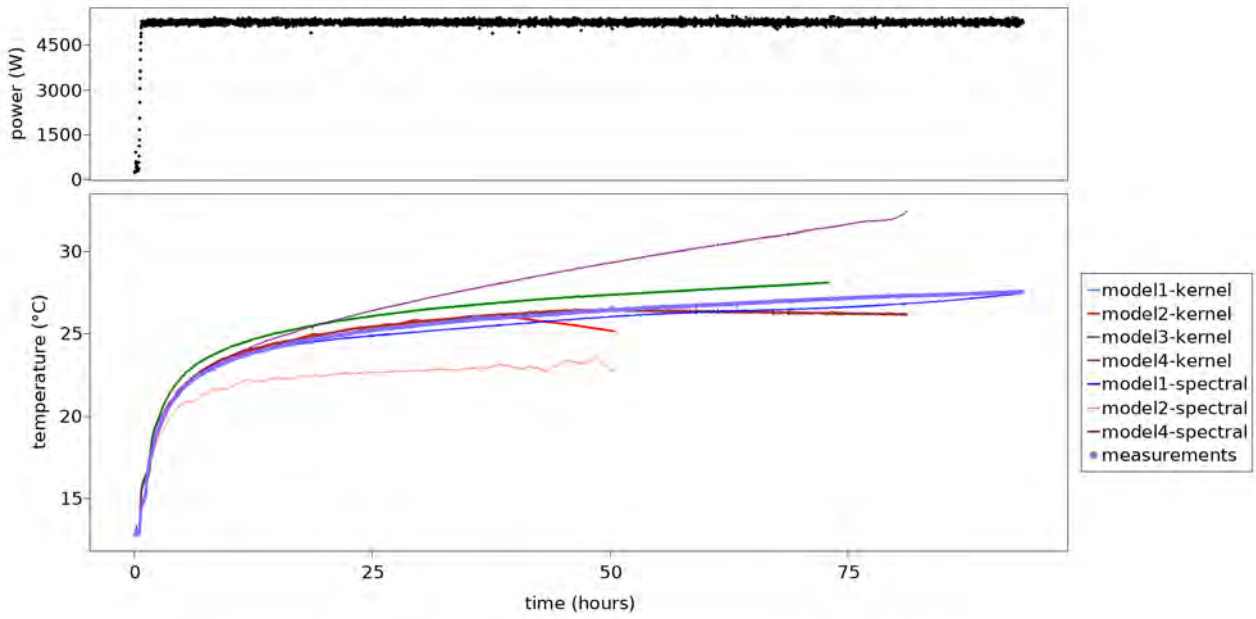


**Figure 4.4:** Validation on dataset 1

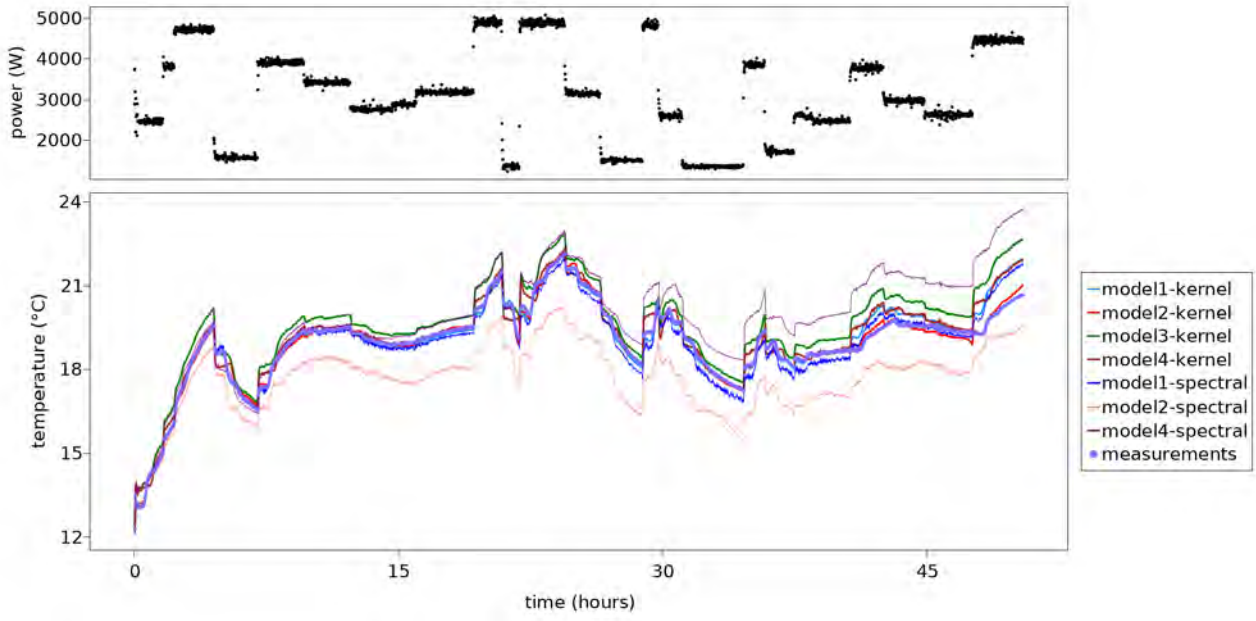


**Figure 4.5:** Validation on dataset 2

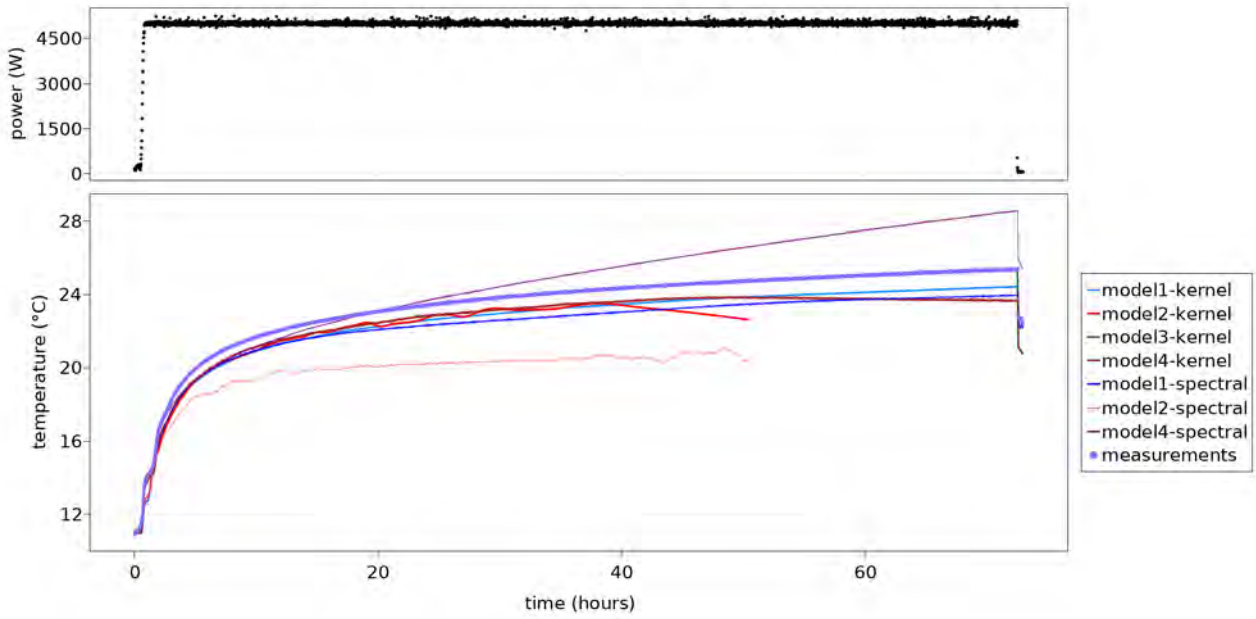


**Figure 4.6:** Validation on dataset 3

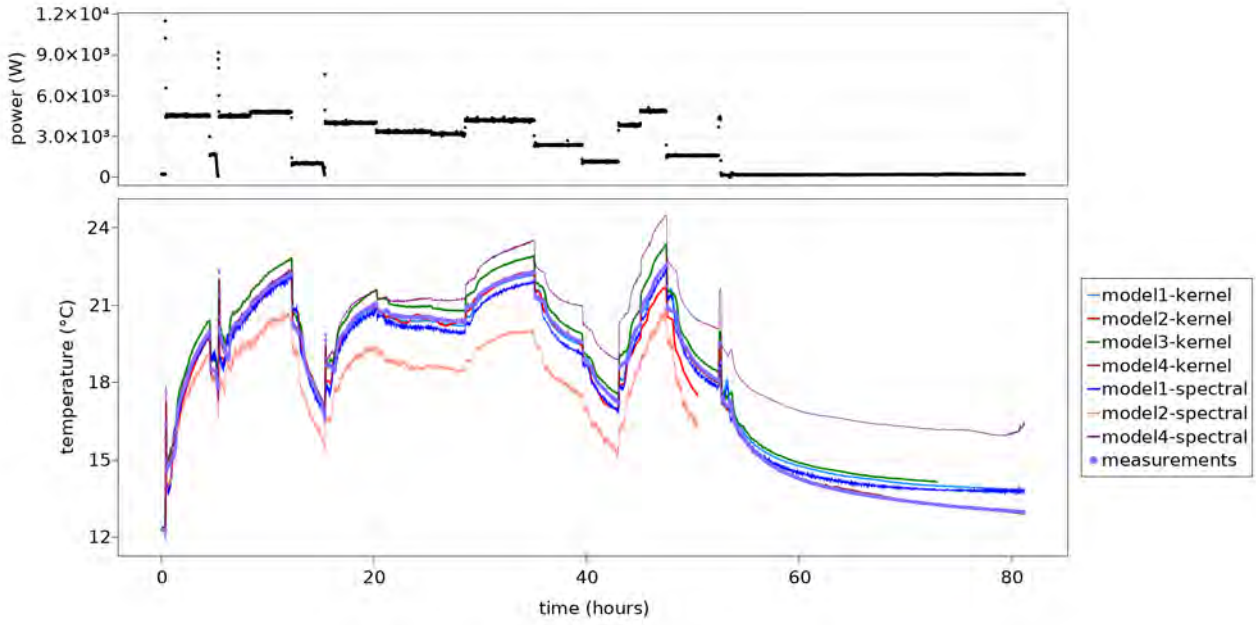


**Figure 4.7:** Validation on dataset 4

# Chapter 5

# Monitoring of ground source heat pumps

Monitoring GSHP installations is important for improving our understanding about these systems as well as improving their performance. Two installations have been monitored within this project. The first one is a research test rig at the KTH Live-in Lab, consisting of a 12 kW heat pump and a 100 m long coaxial BHE. This is the installation described in chapter 3.

As for the second installation, it is the GSHP system of the property *Forskningen 2* consisting of three modern buildings on the KTH campus. As a matter of fact, one of these three buildings host the KTH Live-in Lab and the first and second systems monitored can actually be hydraulically coupled. For the second site, part of the work was realized within the framework of the *Swedish Long-term performance monitoring of larger GSHP systems* project coupled to the International Energy Agency Annex 52 (Energimyndigheten's grant number 45979-1).

One of the design goals for the monitoring project was the detailed measurement of the performance of the geothermal system. A second design goal was taking advantage of a particular feature of the monitored sites, i.e. the borehole field consist of boreholes with lengths ranging between 100 meter and 350 meters, which is a radically different design when compared to standard commercial system where usually the borehole have all the same length. This peculiarity provides the opportunity of comparing borehole of different lengths in operation within the same system.

## 5.1 The monitoring sites

### 5.1.1 The buildings

Since the first installation was already introduced in detail in chapter 3, this part will focus on the second installation. The two installations are located in the same group of buildings, and the context is anyway similar in both cases.

The three buildings of *Forskningen 2* are located on the Royal Institute of Technology (KTH) main campus in central Stockholm, Sweden. The three buildings consist of 302 student apartments (rental) and have hosted students since 2017. The three buildings have a total net floor area of about 6330 $m^2$. Each building is composed of six floors. The buildings were designed as energy plus buildings. In other words, they are supposed to produce more energy than they consume over a (normal) year. The buildings are located in a cold climate and are thus heating dominated. The Domestic Hot Water (DHW) demand represents a large part of the total energy needs of the buildings. Space heating and DHW are provided via

GSHPs. The heat is supplied to the apartments via centralized Air Handling Units (AHUs). The system does not have an auxiliary heating system although heat recovery on wastewater is performed and use to pre-heat DHW. In order to smooth out peak demand from the DHW system, 8 $m^3$ of water tank storage are used.

Cooling is not actively provided although air supplied through ventilation may be conditioned via the borehole heat exchangers. The roof is equipped with PV cells as can be seen in fig.5.1. The buildings are equipped with a comprehensive set of sensors: indoor CO2 levels, relative humidity, temperature, electrical meters, etc.

**Figure 5.1:** Photos and illustration of the three buildings in Forskningen 2. Illustration: Semrén & Månsson. Pictures: KTH Live-In Lab.

### 5.1.2 The ground heat exchanger

The ground source system consists of 12 closed-loop boreholes. Of these 12 boreholes, one is used mainly for research and is in general not used by the system. This borehole is the 100 m long borehole with coaxial BHE presented in chapter 3. Pictures of the coaxial BHE under installation are shown in fig.5.3. The other boreholes are equipped with more traditional U-pipes heat exchangers (PE40). Except for the 100 m "research borehole", boreholes are not designed to be vertical as can be seen on fig.5.2. Instead, they spread out from the machine room essentially in all directions. Both the actual (measured) and design positions are shown in fig.5.2 for each borehole. In addition to being inclined, boreholes also have different lengths. The lengths, inclination and orientation angles for each boreholes are reported in table 5.1. Some of the boreholes are equipped with fiber optics, see section 5.2.2 for more details

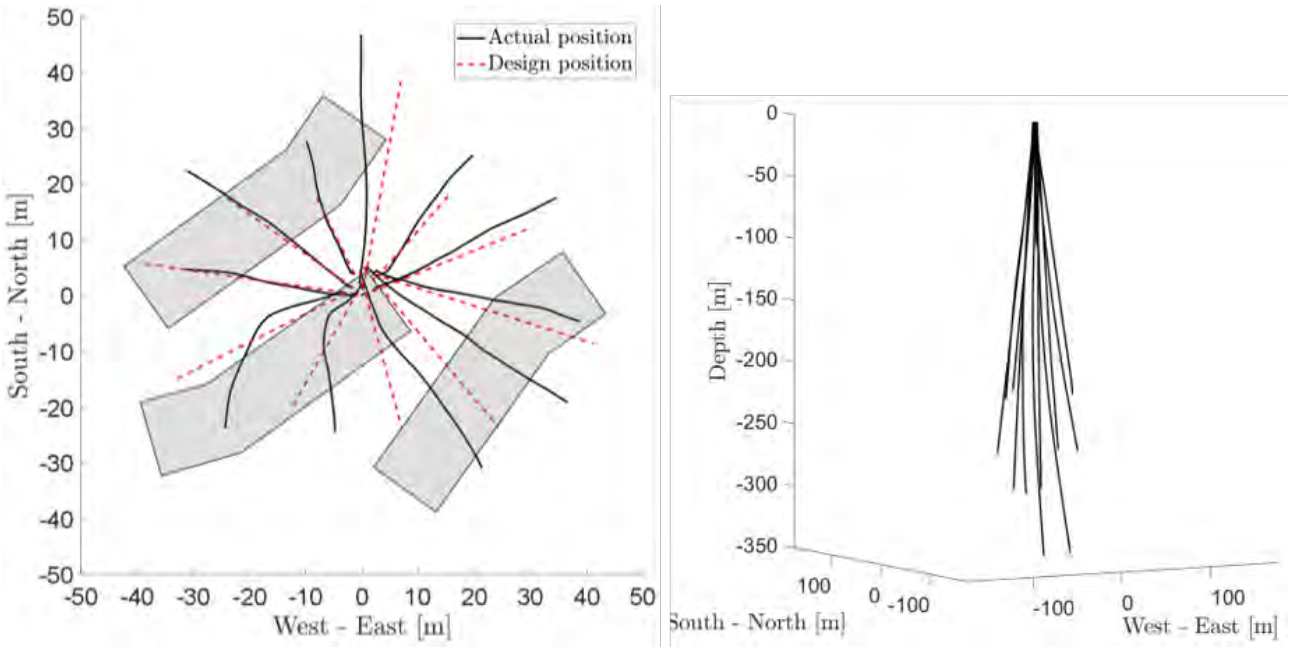


**Figure 5.2:** Top view (left) and 3D view (right) of the borehole field in Forskningen 2

**Table 5.1:** Borehole design lengths, inclinations and orientations

| Borehole | Length [m] | Inclination [°] | Orientation [°] |
|---|---|---|---|
| 1 | 100 | 0.0 | - |
| 2 | 225 | 10.0 | 10 |
| 3 | 225 | 10.4 | 105 |
| 5 | 225 | 10.0 | 280 |
| 6 | 300 | 4.0 | 40 |
| 7 | 270 | 6.3 | 70 |
| 8 | 270 | 7.2 | 135 |
| 9 | 350 | 4.0 | 162 |
| 10 | 350 | 4.0 | 212 |
| 11 | 300 | 6.3 | 248 |
| 12 | 270 | 6.3 | 310 |
| 13 | 300 | 4.0 | 340 |

**Note:** there was no borehole #4 in the original nomenclature. The orientation angle is counted clokwise with the North as reference position (0°).

The borehole field is located on a hill, and it is relatively close to the subway and to a subsurface cavern. These facts lead to a relatively low groundwater level which was measured at 43 m below the surface. In order to avoid having low, or even negligible, heat transfer between the surface and the groundwater level, all the boreholes are therefore grouted over this section. Only the research borehole is not grouted over this section since the coaxial BHE should allow for somewhat efficient heat transfer within the "dry" section. The main features of the ground source and BHEs are presented in table 5.2 and table 5.3, respectively.

The heat pump system consist of three heat pump units, each containing two vapor-compression cycles. The cycles can be qualified as non-conventional since they include a vapor injection line from the condenser outlet to the compressor. The vapor injection limits

**Figure 5.3:** Pictures of the coaxial borehole heat exchanger during installation

the discharge temperature at the compressor outlet, which can otherwise be a problem for high-temperature loads such as DHW production. The heat pumps units have reported Seasonal Coefficients Of Performance (SCOPs) of 4.33 and 2.86 according to EN 14825.

**Table 5.2:** Main characteristics of the ground source system

| | |
|---|---|
| Ground heat exchangers | Inclined boreholes |
| Loop type | Closed loop |
| Ground composition | Metamorphic rocks |
| Groundwater level below ground | 43 m |
| Undisturbed ground temperature | 9.8°C (8.0°C used for design) |
| Design ground thermal conductivity | 3.4 W/(m·K) |
| Design volumetric heat capacity | 2.2 MJ/(kg·K) |

**Table 5.3:** Main characteristics of the ground heat exchanger

| | |
|---|---|
| Number of boreholes | 11 + 1 research borehole |
| Borehole length | 100 - 350 m |
| Total borehole length | 3185 m |
| Av. distance between neighboring boreholes | 10 m |
| Borehole geometric distribution | "Spider / Sunflower" |
| Borehole diameter | 115 mm |
| Borehole filling material | Groundwater and grout |
| Borehole heat exchanger type | Single U-tube, coaxial (research borehole) |
| Design effective thermal resistance | 0.05 m·K/W |
| Pipe characteristics | PEM DN40 PN8 |
| Secondary fluid type | Water-ethanol 28%-wt |

## 5.2 The monitoring set-up

### 5.2.1 Data and sensors

The system has been monitored since the start of operation in September 2017. Since the site is the original testbed of the KTH Live-in Lab, the buildings are equipped with an extensive set of sensors. A subset of all sensors of interest for this work are presented in table 5.4. During the project we had access to data aggregated over hourly intervals during the period between May 2019 to the beginning February 2020. Consequently, the data analyses presented in this report are only preliminary results and will be integrated in future work.

**Table 5.4:** Subset of the system instrumentation of interest for this work

| Measurement point | | Nomenclature |
|---|---|---|
| Source side | Boreholes return temperature (outlet) | KB00-GT41 |
| | Boreholes supply temperature (inlet) | KB00-GT42 |
| | Heat pumps supply temperature (inlet) | KB00-GT43 |
| | Heat pumps return temperature (outlet) | KB00-GT44 |
| | AHU supply temperature (inlet) | KB1-GT11 |
| | AHU return temperature (outlet) | KB1-GT41 |
| | Pressure drop over heat pumps | KB00-DP |
| | Pressure drop over AHUs | KB1-DP |
| Heat pumps (# = 1,2,3) | Heat pump electricity use | VMP#-MQ51 KW |
| | Hot gas discharge temperature (circuit 1 or 2) | VMP#-THG41(-42) |
| | Inlet evaporator (fluid side) | VMP#-KB SUP. MBV |
| | Outlet evaporator (fluid side) | VMP#-KB RET. MBV |
| | Inlet condenser (fluid side) | VMP#-VB RET. MBV |
| | Outlet condenser (fluid side) | VMP#-VB SUP. MBV |
| Load side | Space heating return temperature (outlet) | VS00-MQ41 GTR |
| | DHW return temperature (condenser) | VS02-MQ41 GTR |
| | DHW return temperature (desuperheater) | VS03-MQ41 GTR |
| | DHW tank (1-8) mid-height temperature | VVB-GT51(-58) |
| | Heat pump condenser return temperature (outlet) | VS00-GT1# |
| | Heat pump desuperheater return temperature (outlet) | VS03-GT1# |
| | Energymeter space heating | VS00-MQ41 |
| | Energymeter DHW condenser | VS02-MQ41 |
| | Energymeter DHW desuperheater | VS03-MQ41 |
| DHW | Cold water flow rate (total) | KV1-GF41 |
| | DHW flow rate | Q-VV 5MIN |
| | Energymeter wasterwater heat recovery | KV1-MQ41 |
| AHU 1 | Supply temperature | LB01-GT1 |
| | Return temperature | LB01-GT2 |
| | Outdoor temperature | LB01-GT3 |
| | Exhaust temperature | LB01-GT4 |
| | Current and voltage extraction fan | LB01-FF |
| | Current and voltage supply fan | LB01-TF |
| | Supply air flow rate | LB01-GP1 |
| | Extracted air flow rate | LB01-GP2 |
| | Supply temperature subsystems 1-8 | LB01-GT11(-18) |
| Electricity | Electricty production solar cells (inverters 1-9) | 3x5004 (pa1-9) |
| | Auxiliary electricity use of the energy plant | EM1-KW |

### 5.2.2 Distributed Temperature Sensing

A special feature of the monitoring system is the fiber optic cables installed in boreholes 1, 3, 6, 10 and 12. Together with a Distributed Temperature Sensing (DTS) equipment, these fiber optic cables allow monitoring the temperature inside the boreholes in a distributed manner along their length. Except for borehole 1, the fiber are installed outside the BHE, that is between the pipe and the borehole wall (in an undetermined location within this space). Unfortunately, the cables in borehole 3 and 6 were buried together with the borehole wellhead under asphalt and are not accessible at the time of writing.

This is a brief and largely simplified explanation of how a DTS equipment based on Raman scattering works. A LASER is used to send a single frequency light beam inside the fiber optics. As photons travel through the fiber, they will occasionally collide with the fiber glass molecules. Most of the collisions are elastic, i.e. the photons produced by the collisions will have the same incoming frequency. However, there is a non-zero probability that a shift in frequency, either positive or negative, will occur upon collision. This is referred to as Raman scattering. The probability of occurrence of these shifts is temperature dependent. Thus, temperatures along the length of the fiber can be inferred by measuring these shifts for different times after the initial LASER impulsion.

### 5.2.3 Flow rate, energy and temperature for each borehole

The boreholes were planned to be particularly well-monitored and 5 of the 12 boreholes were consequently equipped with energy-meter, measuring flow rate and temperature difference. Unfortunately, these energy-meters have not been connected to the central data acquisition system of the building so no data were recorded. Due to this problem it was not possible to measure the power injected in each individual borehole. This issue can hopefully be fixed for further research activities and will help in fully achieving one of the initial goals of the monitoring project, and provide a more complete comparison picture regarding performance of longer and shorter boreholes.

## 5.3 Data processing and analysis

### 5.3.1 Building energy features

The main characteristics of the building heating and DHW loads are presented in table 5.5. The cooling and pre-heating potentially provided to the buildings via the ventilation system are not yet accounted for. DHW needs seem to be the dominant part of the total loads for the building as can also be observed in fig. 5.5. The heating signature of the three buildings are presented in fig. 5.4 with 95% confidence intervals (2.5th and 97.5th percentiles) and median indicator. The relative position of the median and mean may indicate potential outliers which could create a bias in the mean. The error bars are quite large, perhaps due to the limited amount of data on which the graph is based.

**Table 5.5:** Overall buiding loads charactersistics

| | |
|---|---|
| Start of evaluation period | 2019-05-26 |
| End of evaluation period | 2020-02-03 |
| Building space heating load met by system [MWhth] | 169 |
| Building cooling load met by system [MWhth] | - |
| DHW load met by system [MWhth] | 304 |
| Thermal energy extracted from the ground [MWhth] | 343 |
| Thermal energy injected to the ground [MWhth] | - |
| Thermal balance ratio (extracted/rejected) | - |
| Heating load (incl. DHW) met by ground source (%) | 100 |
| Cooling load met by ground source (%) | - |

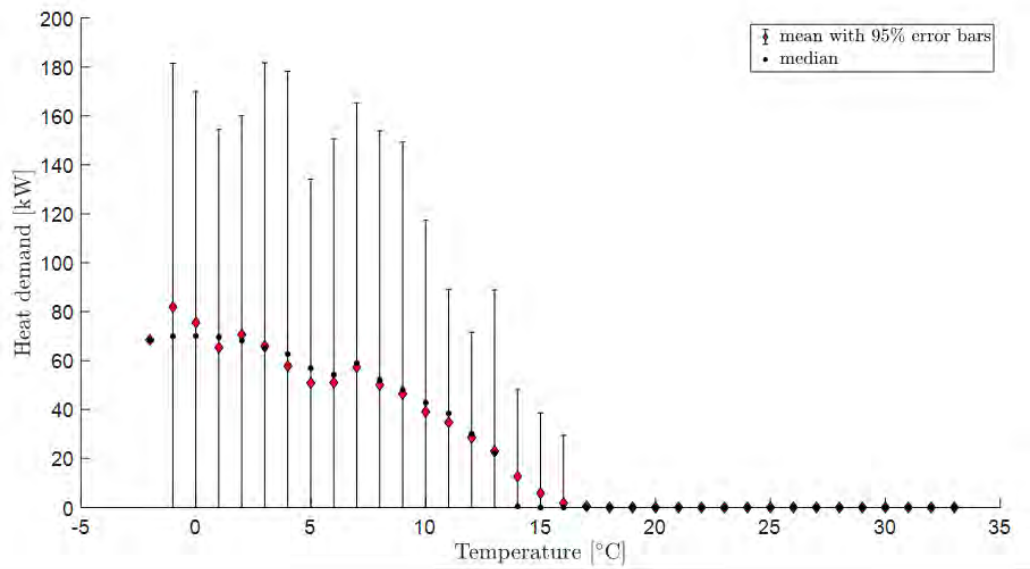


**Figure 5.4:** Building energy signature (heating)

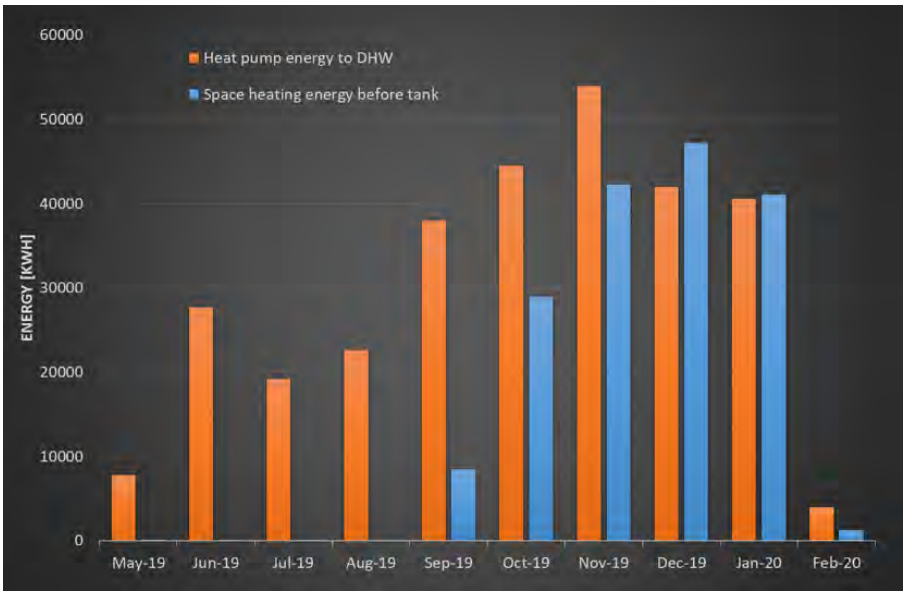


**Figure 5.5:** Monthly heating and DHW loads over the monitoring period

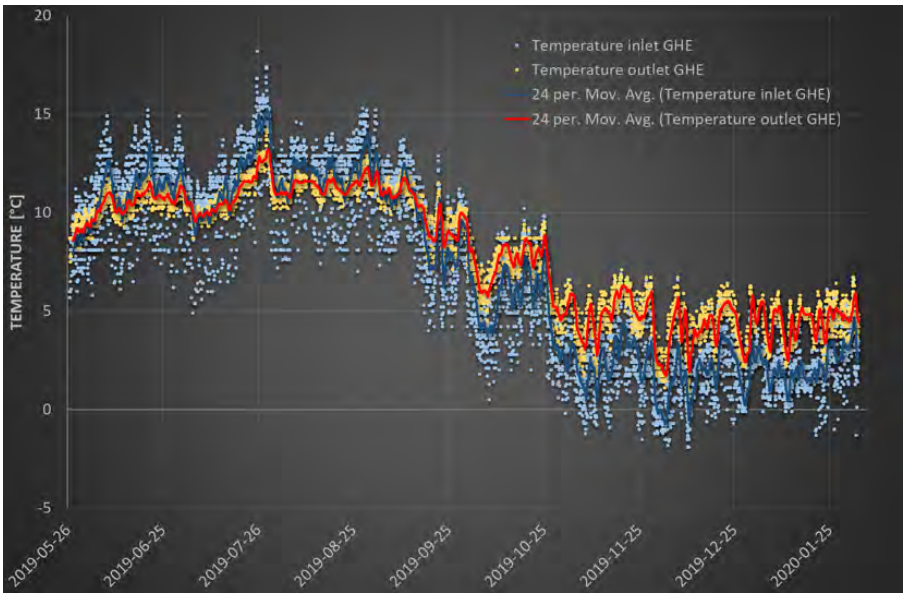


**Figure 5.6:** GHE entering and exiting temperatures and their daily moving average over the monitoring period

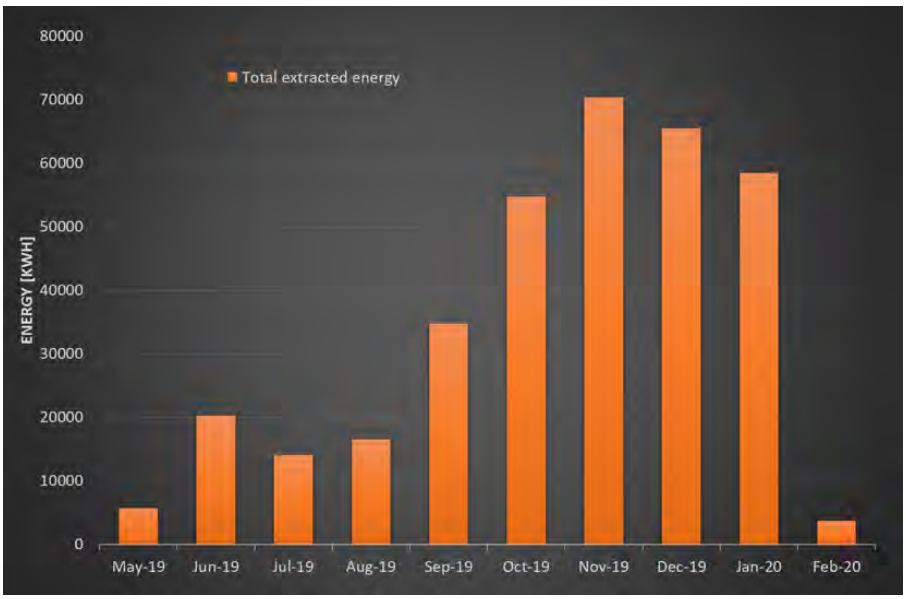


**Figure 5.7:** Monthly extracted energy by the heat pumps

### 5.3.2 GHE performance

The inlet and outlet temperature of the ground heat exchanger over the monitoring period are presented in fig. 5.6. The figure also features the daily moving average over the whole period. The lowest temperature reached is -1.9°C. Based on the temperature profiles summertime, it is likely that cooling is provided through the Ground Heat Exchanger (GHE). The fact that the ventilation is always on also reinforce this hypothesis. Further estimations are however required to assess exactly how much cooling or pre-heating is provided. The lack of information about the flow rate towards the ventilation is in particular problematic.

The monthly amounts of extracted heat by the heat pumps is presented in fig.5.7. The amount of heat extracted by the heat pumps should be close to the amount of heat extracted from the ground although it is possible, in theory, that the heat pumps produce simultaneously heating (for DHW) and cooling.

In addition, the extracted energy is a calculated, and not measured, value. The extracted energy is calculated as such

$$Q_2 = Q_1 - E_c(1 - \xi) \tag{5.1}$$

where

- $Q_2$ is the amount of heat extracted by the heat pumps (evaporator heat)
- $Q_1$ is the amount of heat supplied by the heat pumps (condenser heat)
- $E_c$ is the electrical energy consumption of the compressors
- $\xi$ is the percentage of heat lost through the compressors' envelope.

Here $\xi$ is assumed as 5%.

A scatter plot of GHE outlet temperatures vs. outdoor temperatures is displayed in fig. 5.8. The black dotted line is the $y = x$ line. It is interesting to notice that the GHE outlet is most of the time lower than the outdoor temperature, even during periods where heating is needed (e.g. between 10°C and 15°C, see fig. 5.4). This indicates that Air Source Heat Pumps (ASHPs) with the same characteristics of the GSHP would perform better than the GSHPs. However, ASHPs usually have a larger pinch point over the evaporator and the fan might consume more electricity than the GSHP circulation pump. When cooling is potentially needed (about 25°C to 30°C), the GHE temperature is always lower than the outdoor air temperature and sometimes even low enough to provide direct cooling (just circulating in the GHE).

### 5.3.3 DTS measurements

As previously stated, fiber optic cables are installed in some of the boreholes (between the pipe and the borehole wall). Visualizations of the resulting measurements are shown in

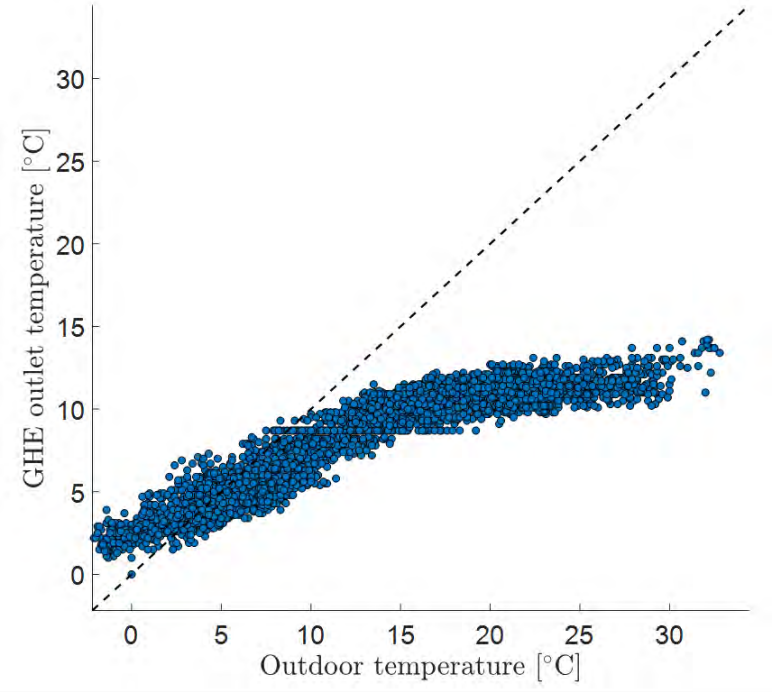


**Figure 5.8:** GHE outlet temperature vs outdoor temperature

fig.5.9a and 5.9b for borehole 10 and 12, respectively. The temperature profiles are shown for the autumn period in 2019. Note the slightly different timescale for the two different plots.

In both graphs, the start of the heating season can be clearly identified. Temperatures in the 350 m long borehole are in general higher, this is both visible in time and at the bottom of the boreholes. Both measured boreholes present a warmer section around 25m depth. Since the boreholes are close to each other in the upper section, these warmer sections perhaps have a common cause that is still undetermined.

A similar graph for the research borehole (#1) is shown in fig. 5.10 for the month of December 2019. The temperature profiles over time look quite different since the borehole is not in use continuously. One can clearly see two heat injection periods - the red and orange stripes - and two heat recovery periods - in shades of blue. The two injection periods actually correspond to the end of the test *erf_P5000_F12* and a *mlprbs* test (not presented in part 4), respectively.

Qualitatively, it can be seen that some sections recover slower than other. For instance, around 30 - 40 m below the ground level and at the bottom of the borehole. Inversely, there are two sections that seem to recover faster, namely around 10 m and 60 m below the ground level.

### 5.3.4 Heat pump system performance

The hourly COP of the heat pumps during space heating (a) and DHW (b) production is shown in fig. 5.11. The COPs are color-coded. Note that data were filtered for COP higher than 10 and that only non-simultaneous space heating and DHW productions are shown (filter of 5 kW). Because of the large spread of COP and temperature values, it is perhaps hard to observe a clear tendency. One can notice that COPs are in general lower during DHW production even for similar temperature levels. For space heating, COPs seem to increase with increasing evaporator inlet temperature as can be expected. The influence of the condenser inlet temperature is however harder to see.

Note that the manufacturer-rated COPs are of 4.33 and 2.86 for temperature levels of 0/-3°C – 30/35°C and 0/-3°C – 47/55°C. The Monthly Performance Factors (MPFs) of the heat pumps ($MPF_1$) during the monitoring period are presented in fig. 5.12 along with $MPF_4$, $MPF_{4+}$ and $MPF_5$. $MPF_4$ includes the circulations pumps on the source and sink side of the heat pump system as well as between the storage tanks and the AHUs. $MPF_{4+}$ includes in addition, heat recovery from wastewater to the MPF calculations. As for $MPF_5$, it includes the energy consumption of the AHUs fans.

The MPFs appear quite stable over time, without any large difference between summer and winter periods. A possible explanation is that COP during space heating production is higher than during DHW production. So, although the source temperature is lower during the winter period (see fig. 5.6), lower condensation inlet temperature due to more space heating production act as a compensation for the PFs. This is particularly visible for the months of September and October which are the first months with space heating needs and also show a small step in PF compared to previous months.

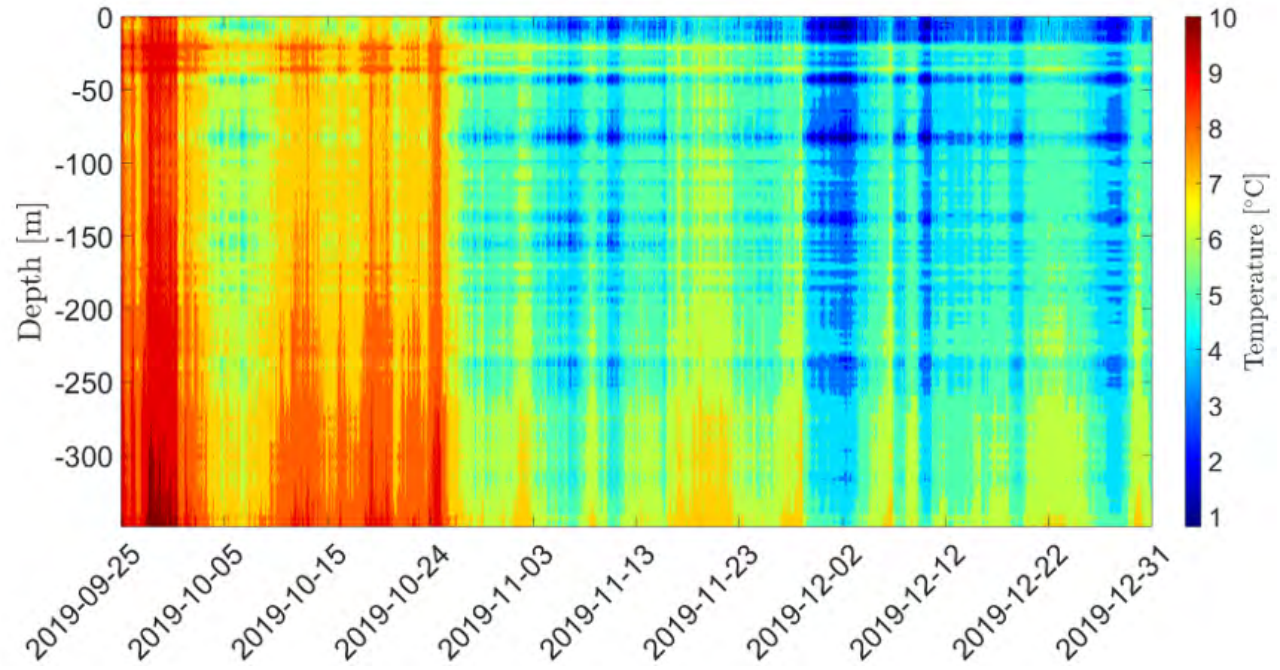


**(a)** Borehole 10

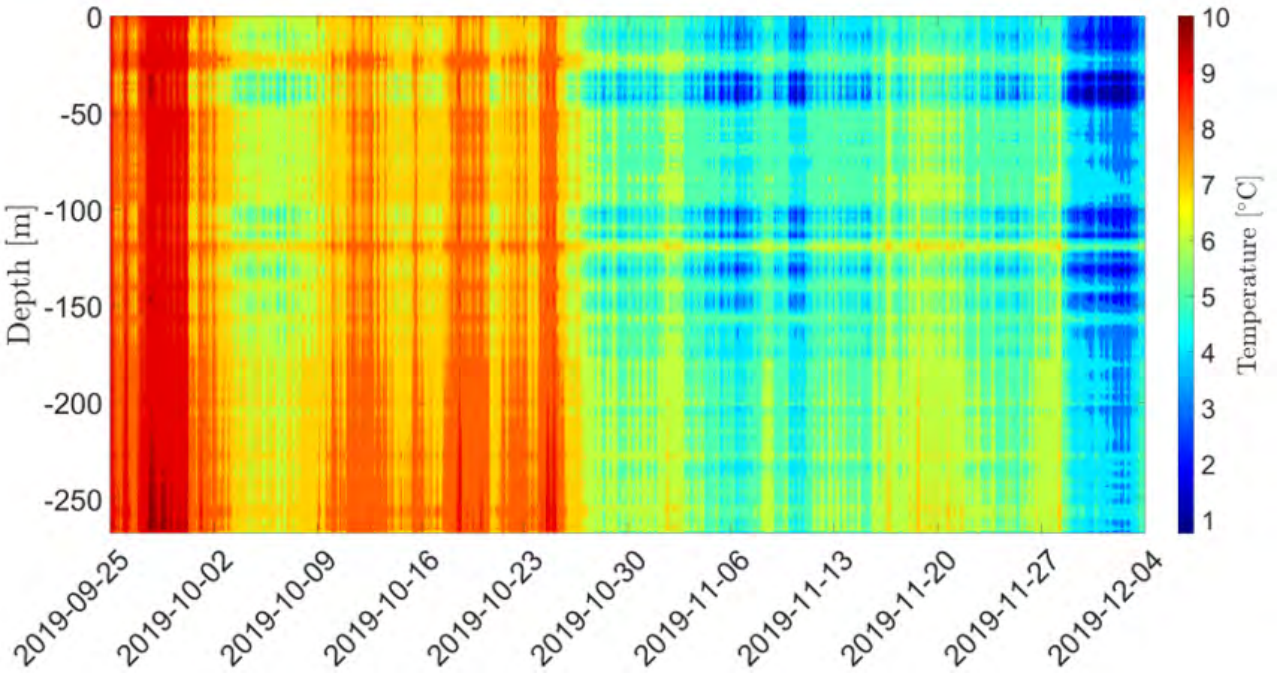


**(b)** Borehole 12

**Figure 5.9:** Contour plots of the measured underground temperature profiles during autumn 2019

The following assumptions are made for the calculation of these MPFs:

- the sensor EM1-KW (see table 5.4) include all circulation pumps inside the machine room
- the wasterwater heat recovery is assumed to have a negligible energy consumption in comparison to other circulation pumps (for $MPF_{4+}$)
- the energy consumption of the ventilation fan is attributed to space heating only when

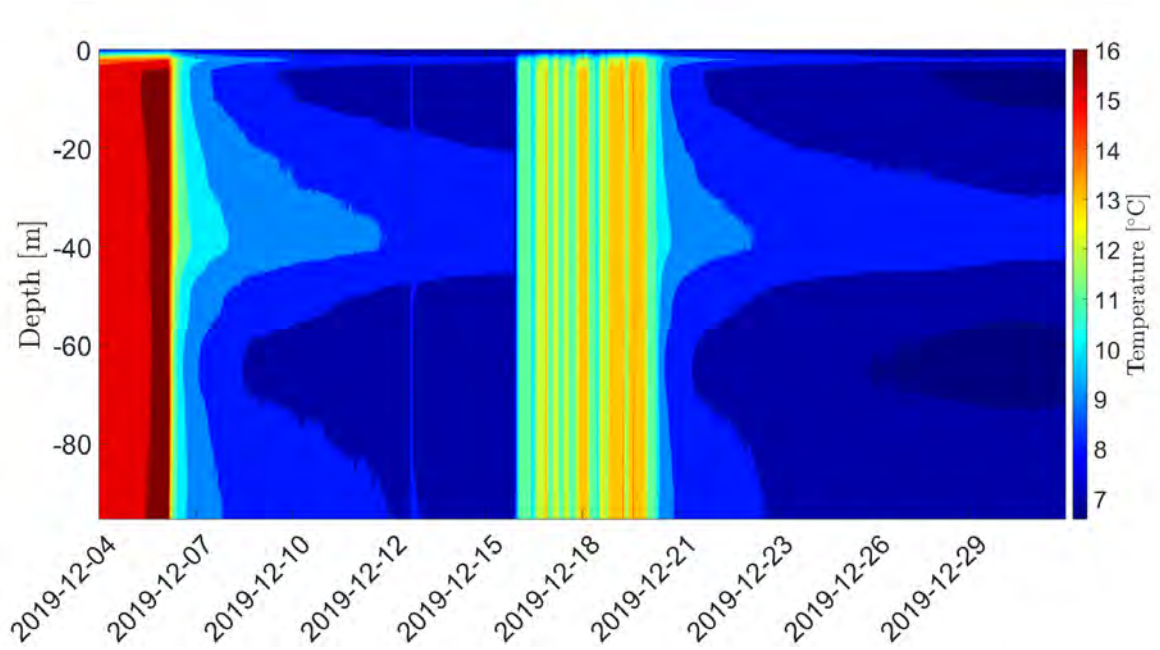


**Figure 5.10:** Contour plot of the temperature profile in the research borehole during December 2019

heat pumps are producing heat for space heating

- solar cells are not included in MPF5

Including the sensor EM1-KW leads to a reduction of about 20% between $MPF_1$ and $MPF_4$. The difference between $MPF_4$ and $MPF_{4+}$ is small and could even be smaller if the pump consumption could be differentiated (from other pumps).

Including the fan energy consumption for the heat distribution within the buildings decreases the MPF by about 13% during the autumn/winter (from $MPF_4$ to $MPF_5$).

## 5.4 Conclusion

Monitoring of the heat pump systems KTH Live-in Lab and *Forskingen 2* have been carried out and data analysis for year 2019 has been performed. The monitoring setup has been utilized to analyze major features characterizing the design and operation of the system such as the building signature, energy exchanged with the borehole field and temperature of the secondary fluid in the borehole loop. Moreover, performance have been evaluated at various level of the system in terms of MPF.

The goal of comparing performance of long and short borehole was partially achieved through the analysis of DTS data but further work will be necessary to include power meter data providing the individual power exchanged in the boreholes of the system. The basic infrastructure for this work is already in place and it could be used in future project. The results observed using the DTS equipment showed a warmer region around 25 meters below the ground surface and a trend of increase in temperature as depth increases below 100 meters of depth.

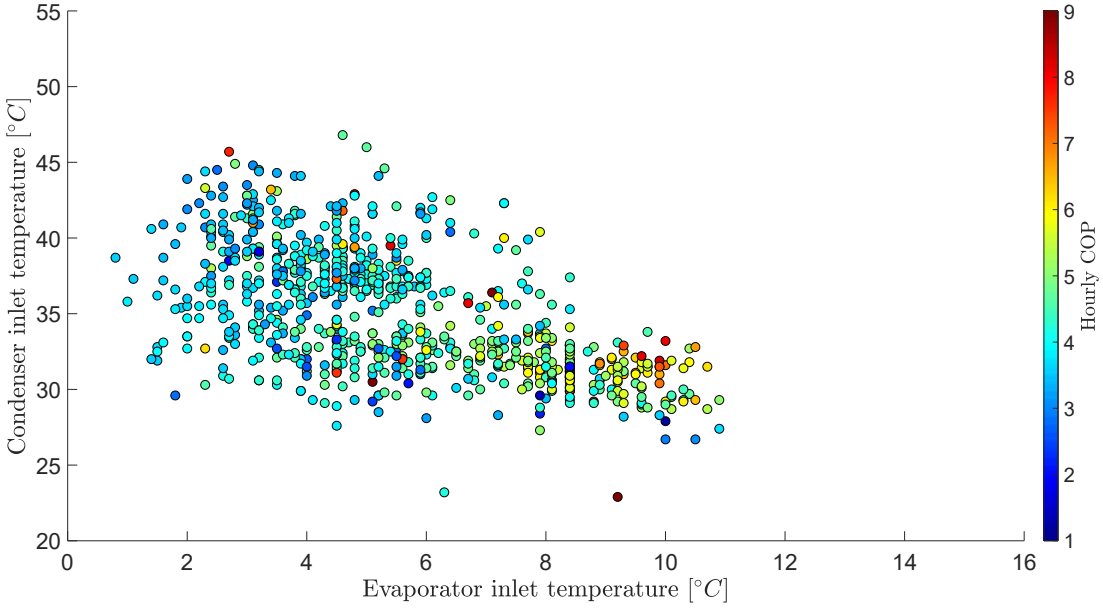


**(a)** Space heating

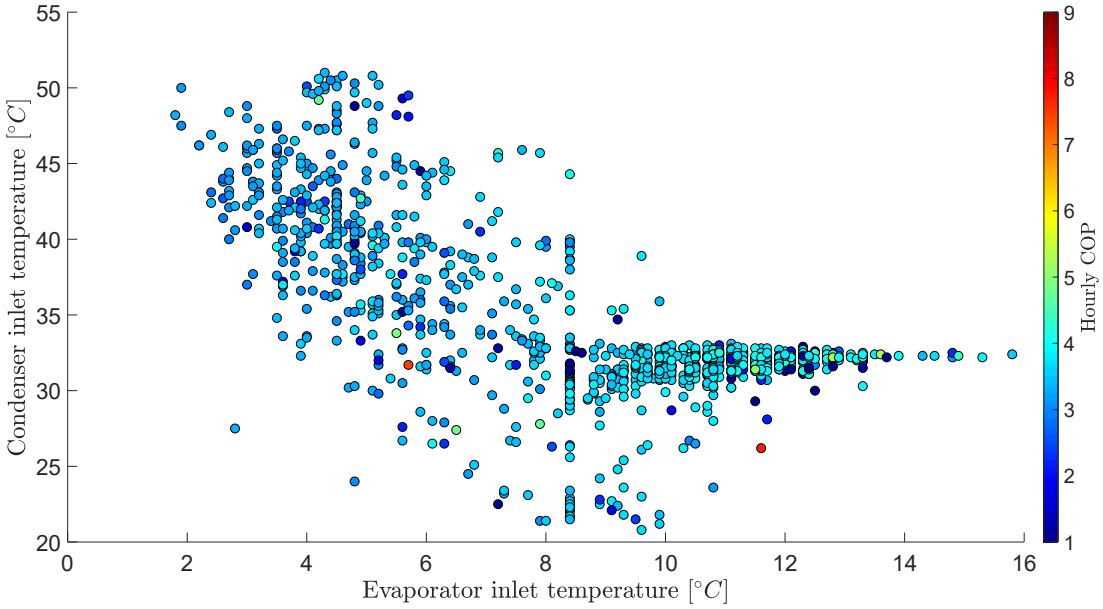


**(b)** Domestic Hot Water

**Figure 5.11:** Hourly COP for different evaporator and condenser inlet temperatures (filtered for COP higher than 10)

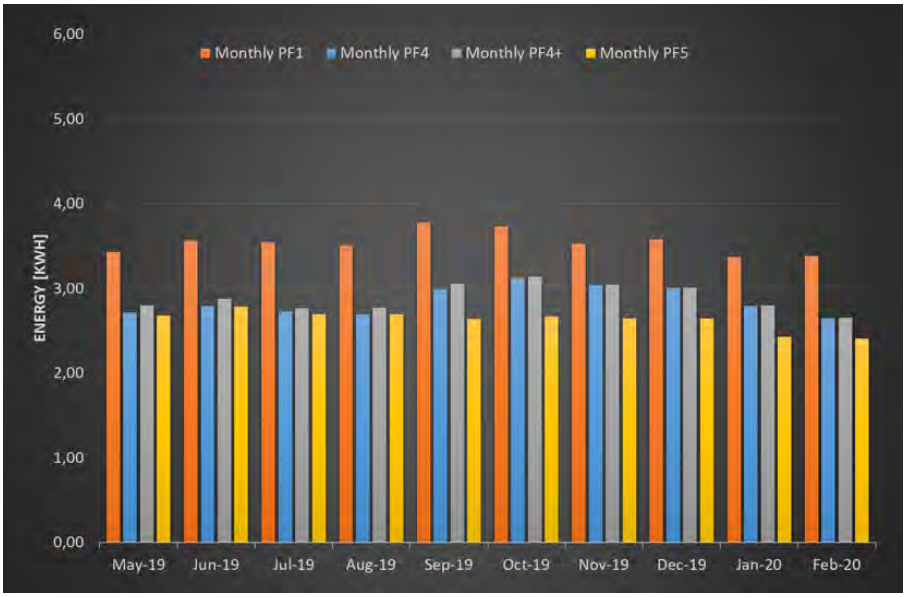


**Figure 5.12:** Heating Monthly Performance Factors for different system boundaries

# Bibliography


[1] K. Andersson. Technology for an environmentally friendly ground source heat pump. page 34, 2018.

[2] ASHRAE. *2015 ASHRAE Handbook - Heating, Ventilating, and Air-Conditioning Applications (SI Edition)*. ASHRAE, Atlanta, 2015. ISBN 978-1-936504-94-7. URL https://app.knovel.com/hotlink/toc/id:kpASHRAEI1/ashrae-handbook-heating/ashrae-handbook-heating.

[3] R. A. Beier, M. D. Smith, and J. D. Spitler. Reference data sets for vertical borehole ground heat exchanger models and thermal response test analysis. *Geothermics*, 40 (1):79–85, Mar. 2011. ISSN 03756505. doi: 10.1016/j.geothermics.2010.12.007. URL http://linkinghub.elsevier.com/retrieve/pii/S0375650511000022.

[4] H. S. Carslaw and J. C. Jaeger. *Conduction of heat in solids*. 1959. URL http://adsabs.harvard.edu/abs/1959chs..book.....C.

[5] W. Choi and R. Ooka. Interpretation of disturbed data in thermal response tests using the infinite line source model and numerical parameter estimation method. *Applied Energy*, 148:476–488, June 2015. ISSN 0306-2619. doi: 10.1016/j.apenergy.2015.03.097. URL http://www.sciencedirect.com/science/article/pii/S0306261915003992.

[6] T. Hastie, R. Tibshirani, and J. Friedman. *The elements of statistical learning: data mining, inference and prediction*. Springer, 2 edition, 2009. URL http://www-stat.stanford.edu/~tibs/ElemStatLearn/.

[7] IEA ECES Annex 21. IEA ECES 2013 Annex21 Thermal Response Test Final Report. Technical report, International Energy Agency, 2013. URL http://media.geoenergicentrum.se/2017/11/IEA_ECES_2013_Annex21_FinalReport.pdf.

[8] L. Ingersoll and H. Plass. Theory of the ground pipe heat source for the heat pump. *ASHVE Transactions*, 54(7):339–348, 1948.

[9] S. Javed and J. Claesson. New analytical and numerical solutions for the short-term analysis of vertical ground heat exchangers. *ASHRAE Transactions*, 117(1):3, 2011. URL http://publications.lib.chalmers.se/publication/149378.

[10] O. C. Jones Jr. and J. C. M. Leung. An Improvement in the Calculation of Turbulent Friction in Smooth Concentric Annuli. *Journal of Fluids Engineering*, 103:615–623, 1961.

[11] A. Lazzarotto and W. Mazzotti Pallard. Thermal response test performance evaluation with drifting heat rate and noisy measurements. In *Proceedings*, page 9, The Hague, 2019.

[12] L. Ljung. On the Estimation of Transfer Functions. *IFAC Proceedings Volumes*, 18(5): 1653–1657, July 1985. ISSN 1474-6670. doi: 10.1016/S1474-6670(17)60805-X. URL http://www.sciencedirect.com/science/article/pii/S147466701760805X.

[13] L. Ljung. *System identification theory for the user*. Prentice-Hall information and system sciences series. Prentice Hall, Upper Saddle River, N.J., 2nd ed.. edition, 1999. ISBN 978-0-13-244193-3.

[14] W. Mazzotti, J. Acuña, A. Lazzarotto, and B. Palm. Deep Boreholes for Ground-Source Heat Pump : Final report. Project report, KTH Royal Institute of Technology, Stockholm, Sweden, 2018. URL http://urn.kb.se/resolve?urn=urn:nbn:se:kth:diva-239937.

[15] W. Mazzotti, H. Firmansyah, J. Acuña, M. Stokuca, and B. Palm. Newton-Raphson method applied to the time-superposed ILS for parameter estimation in Thermal Response Tests. In *Research Conference Proceedings*, Stockholm, Sweden, 2018. doi: 10.22488/okstate.18.000039. URL https://shareok.org/handle/11244/301578.

[16] P. Mogensen. Fluid to duct wall heat transfer in duct system heat storages. *Document-Swedish Council for Building Research*, (16):652–657, 1983.

[17] R. Pintelon and J. Schoukens. *System Identification: A Frequency Domain Approach*. Wiley, 2012. ISBN 9781118287392. URL https://books.google.se/books?id=3lGJWtjGDzsC.

[18] D. Rolando. *Modelling of temperature response factors and experimental techniques for borehole heat exchanger design in geothermal heat pump applications*. PhD Thesis, University of Genova, Genova, Italy, 2015.

[19] D. Rolando, J. Acuna, and M. Fossa. Heat Extraction Distributed Thermal Response Test: A Methodological Approach and In-situ Experiment. 2017. doi: http://dx.doi.org/10.22488/okstate.17.000536. URL https://shareok.org/handle/11244/49337.

[20] J. D. Spitler and S. E. A. Gehlin. Thermal response testing for ground source heat pump systems—An historical review. *Renewable and Sustainable Energy Reviews*, 50: 1125–1137, 2015. ISSN 1364-0321. doi: 10.1016/j.rser.2015.05.061. URL https://www.sciencedirect.com/science/article/pii/S1364032115005328.

[21] T. Söderström and P. Stoica. *System identification*. Prentice-Hall, Inc., USA, 1988. ISBN 978-0-13-881236-2.

[22] A. Vautrin. Development of a new test method for the thermal characterization of borehole heat exchangers. page 58, 2019.

[23] P. Welch. The use of fast Fourier transform for the estimation of power spectra: A method based on time averaging over short, modified periodograms. *IEEE Transactions on Audio and Electroacoustics*, 15(2):70–73, June 1967. ISSN 0018-9278. doi: 10.1109/TAU.1967.1161901. URL http://ieeexplore.ieee.org/document/1161901/.

[24] H. J. Witte, G. J. Van Gelder, and J. D. Spitler. In situ measurement of ground thermal conductivity: a Dutch perspective. *Ashrae Transactions*, 108:263, 2002.

[25] C. Zhang, Z. Guo, Y. Liu, X. Cong, and D. Peng. A review on thermal response test of ground-coupled heat pump systems. *Renewable and Sustainable Energy Reviews*, 40: 851–867, Dec. 2014. ISSN 1364-0321. doi: 10.1016/j.rser.2014.08.018. URL http://www.sciencedirect.com/science/article/pii/S1364032114006947.

# Appendix A

# System identification applied to Thermal Response Tests - Parametric and non-parametric methods

*by Willem Mazzotti Pallard and João Carvalho*

## A.1 Thermal Response Tests and Ground-Source Heat Pump systems

Ground-Source Heat Pump (GSHP) systems are among the most efficient systems to heat and cool buildings. GSHPs have the potential to greatly reduce energy consumption and carbon dioxide emissions in the building sector. The most common type of GSHP systems, at least in Sweden, consists of one or several vertical Borehole Heat Exchangers (BHEs) coupled to a heat pump system. The heat pump(s) is in turn connected to a waterborne distribution system inside the building. A schematical GSHP system is shown in Fig. A.1

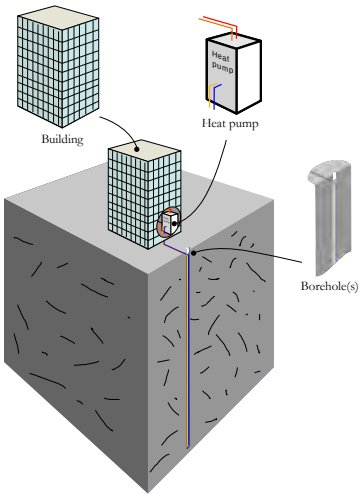


**Figure A.1:** A typical GSHP system comprised of a heat pump which circulates a refrigerant, and a borehole from which it collects or dissipates heat.

GSHP systems with BHEs perform well from an energy standpoint, when properly designed. The design is a sensitive point for these systems because of the slow transient

nature of heat transfer in the ground. Unlike other building energy systems that have somewhat yearly periodic operation, the operation of GSHP systems with vertical BHEs will remain transient over the lifetime of the installation. Therefore, using accurate long-term heat transfer models is essential for the design of GSHP systems. At least equally important is the value of the parameters that such models utilize, among which the thermal properties of the ground and the thermal performance of the BHEs.

In particular, the thermal conductivity of the ground and the borehole thermal resistance are of such importance that an in-situ test is often performed before the design stage in order to estimate them. The state-of-the-art in-situ method used to estimate those two parameters is a Thermal Response Test (TRT). A TRT consists in injecting heat at a constant rate in the ground (i.e. a power step), via circulation in a BHE, while recording the temperature response of the fluid circulating inside the BHE. A typical TRT setup is shown in Fig. A.2. From the recorded temperature response and heat load history, an inverse modelling procedure is then applied to estimate the ground thermal conductivity and effective thermal resistance. This estimation procedure has, in most cases, a deterministic approach and effects of noise, and sometimes even signal variations, are often disregarded. In general, a step heat load is applied as input to the system, although this is based on tradition rather than having a theoretical basis. It is to be determined if the information content of this input is sufficient for the estimation of the usual parameters. Moreover, literature has pointed out to difficulties in estimating more than two parameters because of cross-correlations. One can ask what input heat load could be used to extract more information from the test?

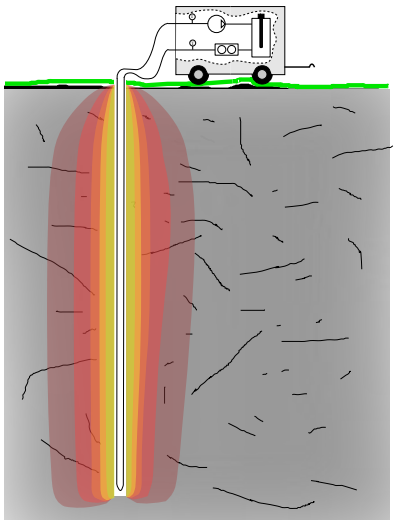

**Figure A.2:** A typical TRT apparatus

## A.2 Infinite Line Source model

The most common model used to interpret TRTs is the Infinite Line Source (ILS) model. It assumes that the heat injection in the ground originates from a line and occurs in an infinite medium. Hence, it assumes that heat diffusion occur only radially around the line source.

In that setup, the solution to the heat diffusion equation is given by (A.1) as shown in [4]

and [8].

$$\Delta T = q\left(R_b^* + \frac{1}{4\pi\lambda^*}E_1\left(\frac{r_b^2}{4\alpha t}\right)\right) \tag{A.1}$$

With the following list of variables:

- $q = \frac{Q}{H}$ where $Q$ is the injected heat, through the circulating fluid and $H$ is the effective depth of the borehole.
- $r_b$ borehole radius.
- $\alpha$ thermal diffusivity "$\frac{\lambda^*}{\rho c}$".
- $\lambda^*$ ground thermal conductivity.
- $R_b^*$ borehole thermal resistance $\frac{T_{avgfluid}-T_b}{q}$.
- $E_1$ exponential integral $\int_x^\infty \frac{e^{-u}}{u}du$.

The "starred" terms refer to the "effective" terms, which can be interpreted as lumped properties. For instance, the thermal conductivity might slightly vary with depth due to different geological layers but the temperature response can be interpreted as if the ground was homogeneous with a certain thermal conductivity. It is latter that is called effective thermal conductivity. Note that the effective terms are strongly linked to the interpretation model.

The ILS model does not represent well the short-term (0-10 hours) behavior of heat transfer inside and around the boreholes. This is because heat is not effectively dissipated on a line; moreover, the BHE has a different thermal behavior than the surrounding ground. The ILS model can however be used to reproduce the long-term behavior of a TRT (from 20 hours forward). Note that a TRT lasts usually between 50 to 100 hours but the heat transfer regime is still far from steady-state at these time scales (up to hundreds of years), rather the temperature changes logarithmically with time.

### A.2.1 Approximations

Looking closer at the formula for $E_1(x) = \int_x^\infty \frac{e^{-u}}{u}du$, this function has a drawback that it cannot be computed exactly, therefore we need to employ an approximation. Namely, by integrating the Taylor expansion of the integrand $\frac{e^{-u}}{u}$ we get the approximation:

$$E_1(x) \approx -\log(x) - \gamma - \sum_{i=1}^{\infty}\frac{(-x)^i}{i\cdot i!} \tag{A.2}$$

where $\gamma$ is the Euler-Mascheroni constant, and in practice we drop the sum terms, as these represent the higher order terms of the Taylor expansion. In the context of the ILS model, this can be done for large times (small $x$). This approximation is convenient not only because it is close to the exact formula for $E_1$ (see Figure A.3), but also because it is linear in the logarithm of $x$ and in $q$.

Under this approximation the formula for the system response becomes:

$$\Delta T \approx q\left(R_b^* + \frac{\log(4\alpha r_b^{-2}) - \gamma}{4\pi\lambda^*}\right) + \frac{q}{4\pi\lambda^*}\log(t) \tag{A.3}$$

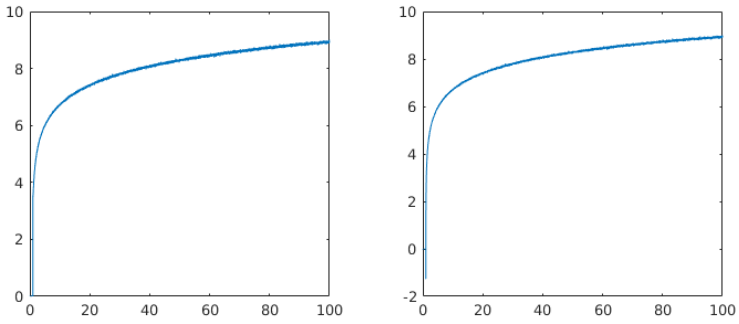


**Figure A.3:** example simulation of the TRT test using equation A.1 (left) and the approximation through equation A.2 (right).

Which is an affine function, as pointed out before. However, since it is of the form $y = mx + b$, it results in only two parameters, the slope $m$ and the intercept $b$, and since the slope is of the form $\frac{q}{4\pi\lambda^*}$, we can use it to determine the ground thermal conductivity (since we know $q$), but since the intercept depends on both the borehole thermal resistance and the thermal diffusivity $\alpha$ this method is not enough to determine the full range of parameters governing equation (A.1). However, if we make the assumption that we can reliably measure $\alpha$ given $\lambda$ (that is we know the ground density $\rho$ and its thermal capacity $c$) we can calculate the thermal resistance of the borehole $r_b$ from the value of $b$.

## A.3 TRT in a system identification framework

In order to apply system identification methods to TRT, it is useful to express the TRT process in a block diagram. Such a block diagram is presented in Fig. A.4 with the injected power per meter of drilling, $q$ (note the difference with the shift operator, also $q$), as input and the fluid temperature increase over time, $\Delta T$, averaged between inlet and outlet, as output. Here the 0 subscript refers to the "true" value. It should be noticed that the presented block diagram is a simplification of the real problem; for instance, it is not rare that the power is calculated using the temperature or there could be some disturbances from the environment (e.g. ambient air temperature changes).

Another observation that can be made is that there is measurement noise on both the input and the output. As we have seen, this is a problem because it leads to a biased least-square estimator due to the the noise on the input signal. This can be understood be developing the

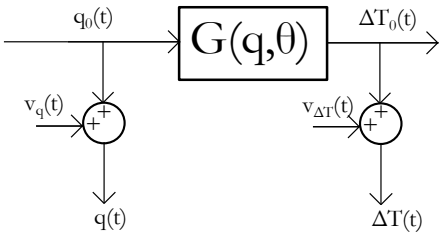


**Figure A.4:** A block-diagram representation of a Thermal Response Test.

expression for the MSE

$$MSE[\tilde{G}] = E\left[\left\|\Delta T - \tilde{G}q\right\|^2\right]$$
$$MSE[\tilde{G}] = E\left[\left\|v_{\Delta T}\right\|^2\right] + E\left[v_{\Delta T}^T(\Delta T_0 - \tilde{G}q)\right] + E\left[(\Delta T_0 - \tilde{G}q)^T v_{\Delta T}\right] + E\left[\left\|\Delta T_0 - \tilde{G}q\right\|^2\right]$$

Assuming that the noises on the input and output are independent, we find that

$$MSE[\tilde{G}] = E\left[\left\|v_{\Delta T}\right\|^2\right] + E\left[\left\|\Delta T_0 - \tilde{G}q_0 - \tilde{G}v_q\right\|^2\right]$$
$$MSE[\tilde{G}] = \lambda_{v_{\Delta T}} + \left\|\Delta T_0 - \tilde{G}q_0\right\|^2 + E\left[\left\|\tilde{G}v_q\right\|^2\right]$$

where the $l^2$-norm is used, $\Delta T$ and $q$ are time vectors of the same length and the $v_{\Delta T}$ are assumed identically distributed. As seen, we end up with a variance and a bias term. The latter should be minimum when the estimator $\tilde{G}$ is the true system operator $G_0$. However, due to the noise $v_q$, the bias term will be minimized for another value than $G_0$. If $\tilde{G}q$ represents the convolution of an impulse response with the input heat flux, the MSE will favor impulse response with lower norm. For instance, if the $v_q$ elements are independent and identically distributed (iid), then the last term in the previous expression reduces to

$$\lambda_{v_q} \sum_{t=1}^{N} \sum_{i=1}^{t} g_i^2 = \lambda_{v_q}(N g_1^2 + (N-1)g_2^2 + ... + g_N^2) = \lambda_{v_q} \left\|\tilde{G}\right\|_F^2$$

the last equality being true if $\tilde{G}$ is a lower Toeplitz matrix with first column $[g_1\ g_2\ ...\ g_N]^T$ and where $\|X\|_F$ refers to the Frobenius norm of matrix $X$.

Assuming that the ILS model is correct and assuming that we are able to measure the temperature response at the borehole wall (i.e. the borehole thermal resistance can be neglected), the impulse is given by the time derivative of the exponential integral term in (A.1) which is

$$g(t) = \frac{1}{4\pi\lambda^* t} e^{-\frac{r_b^2}{4\alpha t}} \tag{A.4}$$

So the value of the Frobenius for different thermal conductivity values can be computed over a specified time range (here chosen as 100 hours since this is a usual test duration). The Frobenius norm of ILS-based impulse response $\tilde{G}$ is shown in Fig. A.5. Fig. A.5 shows that the Frobenius norm decreases with increasing thermal conductivity and, thus, input noise will lead to overestimated values of the thermal conductivity if the MSE is used as cost function. Nevertheless, the absolute value of $\left\|\tilde{G}\right\|_F^2$ is small so the bias introduced by the input noise should also be small if the input and output noise are of the same order of magnitude. This is verified numerically for a given set of realistic parameters, shown in table A.1. The average estimated $\tilde{\lambda}^*$ for 500 realizations is found to be 3.016 $W \cdot m^{-1} \cdot K^{-1}$ which is only deviating about 0.5% from the true value. Using instead an "exaggerated" input noise variance of 25 $W^2/m^2$, the bias leads to an overestimated thermal conductivity of 3.104 $W \cdot m^{-1} \cdot K^{-1}$, corresponding to a 3.5% deviation.

Although the introduced bias does not seem to be large for the conditions of table A.1 and given the assumption of iid noise elements, it is desirable to get rid of the input noise burden. To obtain an unbiased estimator under the assumptions previously mentioned and given the knowledge of the input noise variance $\lambda_{v_q}$, one could use $MSE[\tilde{G}] - \lambda_{v_q}\left\|\tilde{G}\right\|_F^2$ as

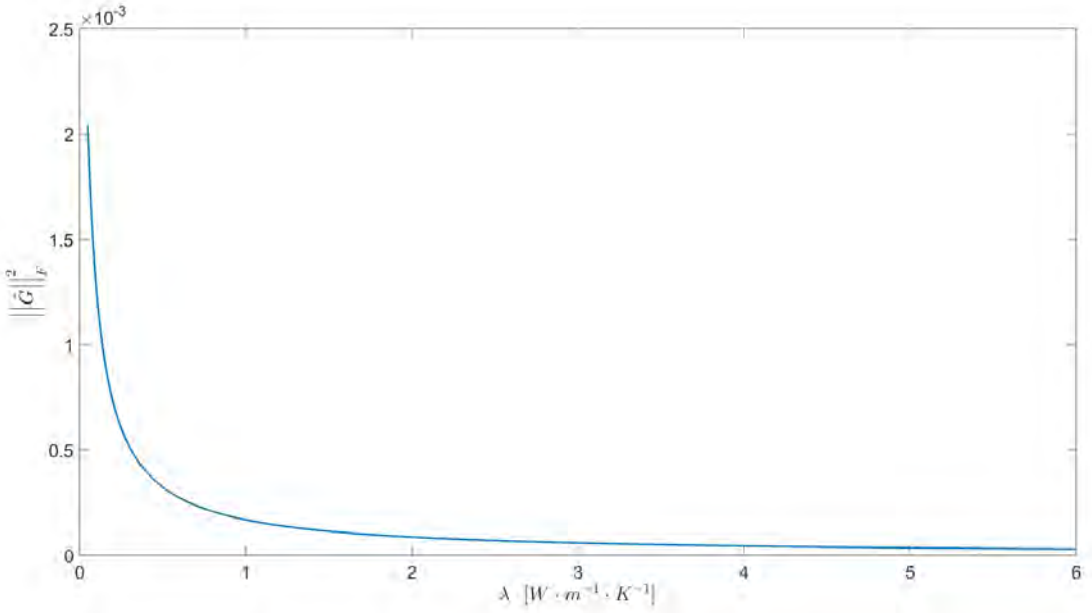


**Figure A.5:** Frobenius norm of ILS-based impulse response for different thermal conductivity values (calculated over 100 hours with 30 s interval)

**Table A.1:** List of parameters used to evaluate the bias introduced by input noise

| $\lambda^*$ | $\rho c_p$ | time range | $r_b$ | $q$ | $v_{\Delta T}$ | $v_q$ |
|---|---|---|---|---|---|---|
| $W \cdot m^{-1} \cdot K^{-1}$ | $J \cdot m^{-3} \cdot K^{-1}$ | hrs | $m$ | $W/m$ | - | - |
| 3 | $2.16 \cdot 10^6$ | $0 - 100$ | 0.0575 | 30 | $N(0, 0.05)$ | $N(0, 4)$ |

cost function. However, it is also helpful to filter out the noise from the input power for other reasons than obtaining an unbiased estimator. In order to do that, input data is processed in several different ways (in the different parts of the project work). The way input data is processed is specified in the respective sections. It should kept in mind that boreholes are in general quite long (≈100s of meter) with residence times (the time it takes for the fluid to circulate round) between 10 min to a couple of hours. Moreover, the ground around the borehole is very large (theoretically infinite), and has a very high thermal inertia so that any fast variation of input power will be dampen by the system. Hence the system acts as a natural low-pass filter.

## A.4 TRT data and input informativeness

### A.4.1 TRT data

The data from two real TRTs are used in this study. The two tests are performed in the same borehole, 335 m deep (active depth, i.e. the length over which heat transfer is effectively happening, of 331.7 m), with about two weeks interval between the tests. During the first TRT, the borehole is filled with groundwater while it is filled with grouting material (a material that makes the borehole as watertight as possible) during the second test. Each TRT is a heat injection test and last for about 120 hours, more details about the test can be found in [14].

The input (heat flux) and output (temperature response) for the first and second TRT are presented in Fig. A.6a and Fig. A.6b, respectively. One can note that these TRTs do not correspond to the common test conditions because the input heat flux is far from a power step for either of the tests.

Note the sampling patterns are irregular and different for each test. During the first TRT, data is sampled every 5 minutes for most of the test while the sampling rate is about 50-60 seconds for the second TRT.

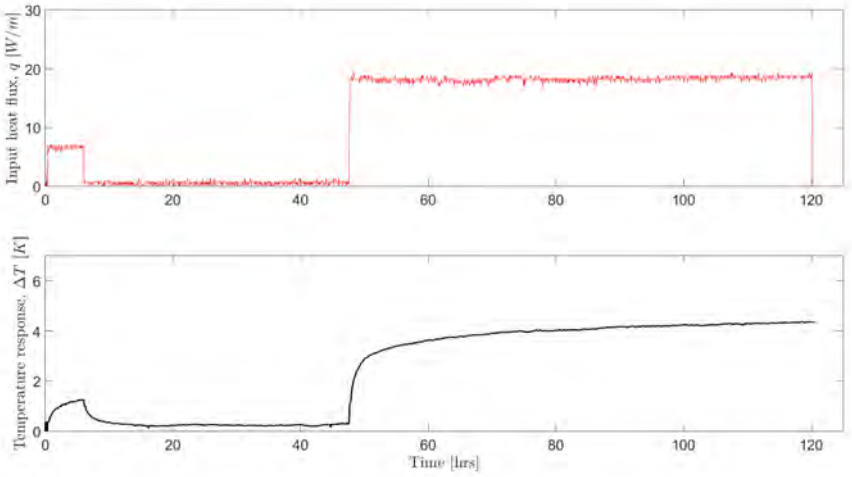


**(a)** First TRT: water-filled borehole

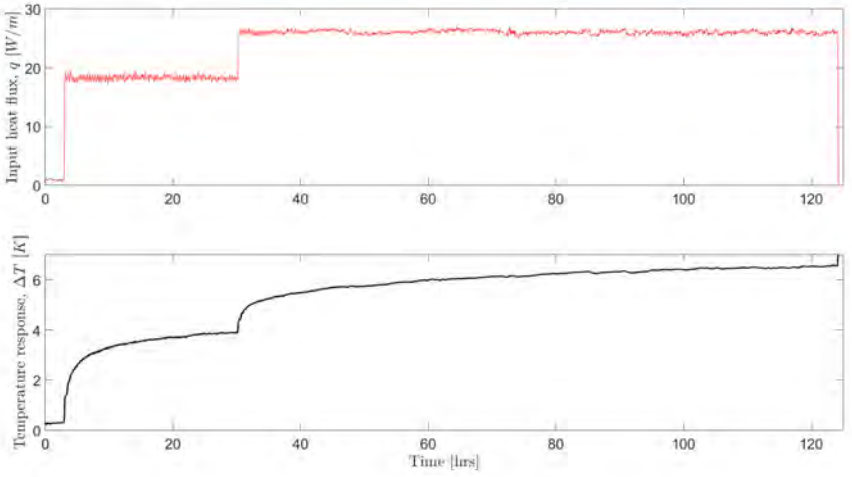


**(b)** Second TRT: grouted borehole

**Figure A.6:** Input heat flux and temperature response for both TRTs

### A.4.2 Input informativeness

Although it is well-accepted that TRTs should be performed with a constant power step [20, 25, 2], there does not seem to exist any theoretical reason behind this choice, besides the simplification of the exponential integral into a logarithmic term (see section A.2.1). The later simplification is convenient because it allows to use linear regression as a way to estimate the thermal conductivity and borehole thermal resistance. Applying a constant power step most likely comes from the original proposal of Mogensen [16] and has then been perpetuated as a tradition since then.

We therefore decided to investigate the informativeness of such a step input here. To analyze the informativeness of the input, we look at the joint input and output vector $z = [q\ \Delta T]^\intercal$. Namely, the input is informative enough if:

$$\phi_z(\omega) > 0$$

Under the assumption that the process is quasi-stationary. By definition, a process $Q$ is quasi-stationary if [13]

$$E[q(t)] = m_q(t) \quad , \quad |m_q(t)| \leq C \quad , \quad \forall t \tag{A.5}$$

$$E[q(t)q(r)] = R_q(t,r) \quad , \quad |R_q(t,r)| \leq C \quad , \quad \forall (t,r) \tag{A.6}$$

$$\lim_{N\to\infty} \frac{1}{N} \sum_{t=1}^{N} R_q(t, t-\tau) = R_q(\tau) \quad , \quad \forall \tau \tag{A.7}$$

where the expectations are with respect to the stochastic term in $q$. Let's assume that the input power can be represented as $q = q_0 + v_q$ (i.e. decomposed between deterministic and stochastic terms like the Wold decomposition), then $E[q(t)] = q_0(t)$ and $E[q(t)q(r)] = q_0(t)q_0(r) + cov(v_q(t), v_q(r))$ where the mean of $v_q(t)$ is assumed to be zero for all $t$. Hence eq.(A.5) and (A.6) hold in our case. To show that eq.(A.7) also holds, we can observe that $q(t) = 0\ \forall t < 0\ and\ \forall t > n$, because the test has a finite duration (between 0 and n). Thus eq.(A.7) reduces to

$$\lim_{N\to\infty} \frac{1}{N} \sum_{t=max(\tau,1)}^{N} \left[q_0(t)q_0(t-\tau) + cov(v_q(t), v_q(t-\tau))\right] = R_q(\tau) \tag{A.8}$$

and the limit exists.

### A.4.3 Informativeness for noisy data

Firstly, the matrix spectrum of $z$ is determined for raw input and output data, that is, including noise. This was done using the *cpsd* function in Matlab (Cross Power Spectral Density) which calculates the Fourier transform of the given input at discrete normalized frequencies ($\omega T$). Since these frequencies are discrete, it is not possible to verify that $\phi_z$ is positive-definite for all $\omega$ but it is possible to exclude informativeness if any of the computed $\phi_z(\omega)$ is not positive-definite. The obtained power spectral density for input and output in both tests is shown in Fig. A.7.

The positive definiteness of each $\phi_z(\omega)$ is checked through the Cholesky decomposition, using the *chol* function in MATLAB, but also using eigenvalues and the determinant of the

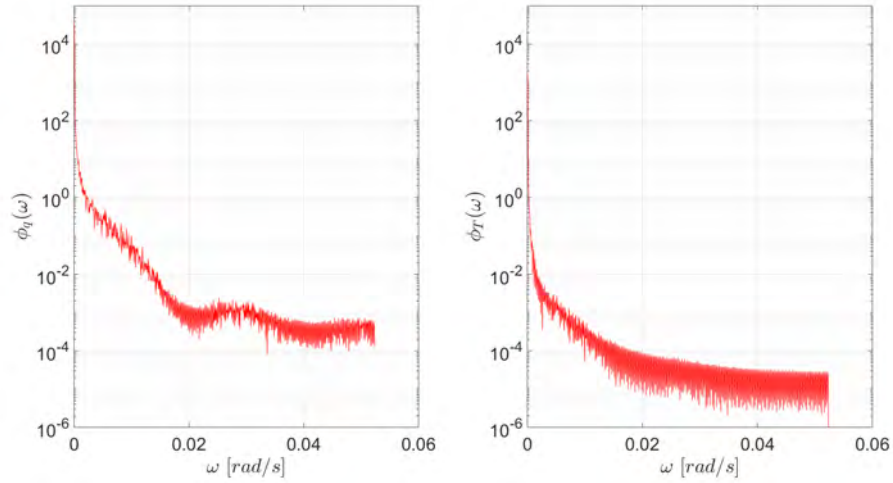


**(a)** First TRT: water-filled borehole

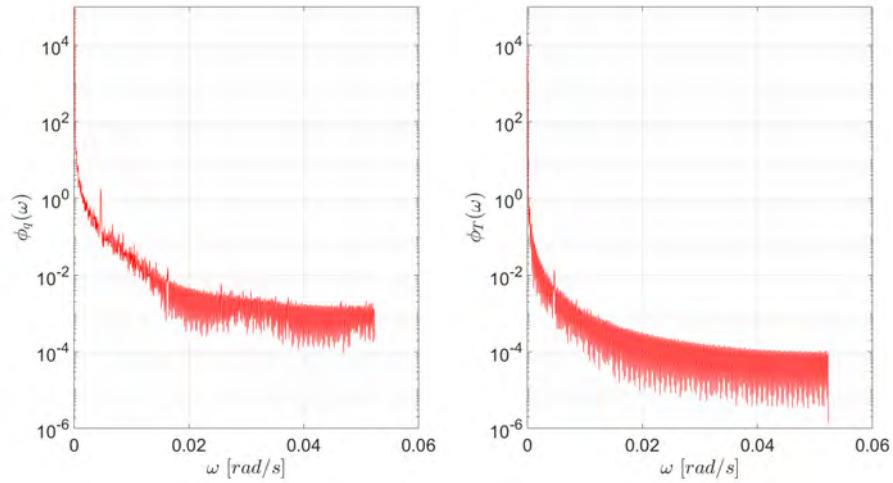


**(b)** Second TRT: grouted borehole

**Figure A.7:** Power spectral densities of the input power and output temperature increase for both the first and second TRT

minors. For all three checking methods, the cross-spectral matrix $\phi_z(\omega)$ is found to be positive definite for the discrete set of $\omega$ obtained from data from both TRTs. However, these checking methods may return a positive result for numerical reasons. For instance, the eigenvalues are close to zero for high frequencies, see fig.A.8. A way to avoid this issue would be to consider that eigenvalues are effectively 0 when lower than some $\epsilon > 0$. It is nevertheless not straightforward how to choose such a limit.

Moreover, when measurement noise is included in the analysis, we might be considering some frequencies to which the system is not effectively excited. The input power seems to be persistently exciting whereas it might simply an effect of measurement noise. Data was pre-filtered with a low-pass filter but this did not lead to better approximations. One thing that can be noticed is that there seems to be information content at low frequencies, that is the part in which we are interested (the thermal conductivity will typically

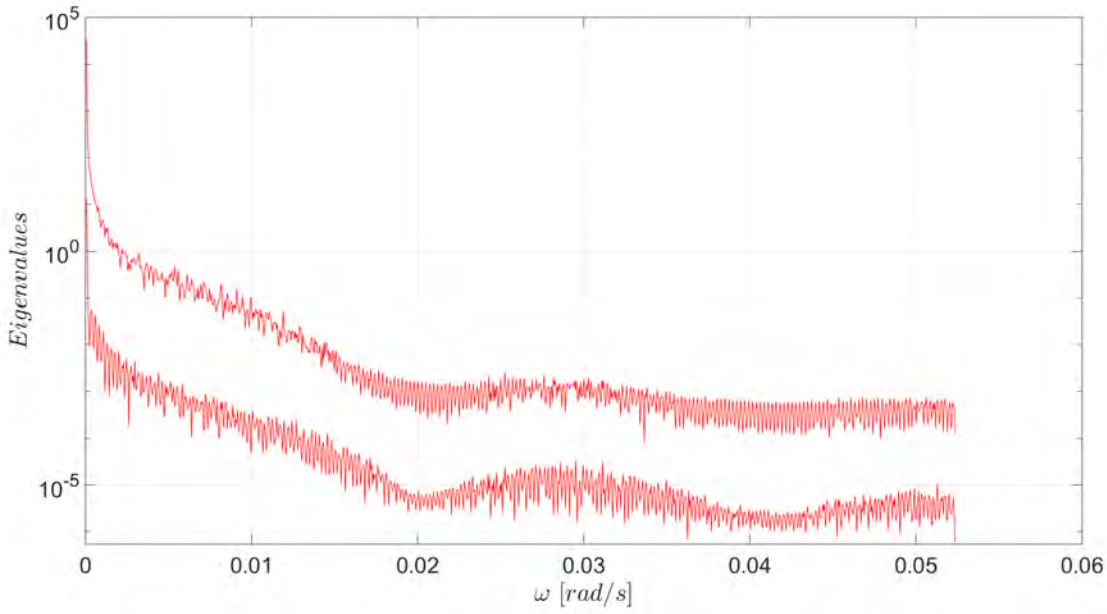


**Figure A.8:** Eigenvalues of the matrices $\phi_z(\omega)$ for the first TRT

### A.4.4 Informativeness of a theoretical step

In order to better understand informativeness for an input power that is a perfect step, the problem is studied theoretically. The perfect step power is modelled using the Heaviside step function, $H(t)$

$$q(t) = aH(t) \tag{A.9}$$

The auto-correlation coefficients can then be calculated as (see eq.A.8)

$$R_q(\tau) = \lim_{N\to\infty} \frac{1}{N} \sum_{t=max(\tau,1)}^{N} a^2 = \lim_{N\to\infty} a^2 \frac{N - max(\tau,1) + 1}{N} = a^2 \tag{A.10}$$

Thus, the power spectral density of the input power can be written as

$$\phi_q(\omega) = \sum_{\tau=-\infty}^{\infty} a^2 e^{-i\omega\tau} = a^2 \left(1 + 2\sum_{\tau=1}^{\infty} cos(\omega\tau)\right) \tag{A.11}$$

Hence, $\phi_q(\omega)$ is not well-defined unless $\omega = \frac{\pi}{2} \pm \pi k \quad k = 0, 1, ...$ in which case $\phi_q(\omega) = a^2$. In other cases, the summation term will either diverge (for $\omega = 2\pi k$), be equal to 0, 1 or -1. Numerically, for a finite number of terms, the sum of cosinus converges to 0 for any $\omega \neq \pi \pm 2\pi k$ and $\omega \neq \pm 2\pi k$ so that the power spectral density of the Heaviside step function seems to be positive for all $\omega > 0$. Therefore, a Heaviside step function as power input seems to be persistently exciting.

According to theorem 2.2 in [13], we have that

$$\phi_{\Delta T}(\omega) = \left|G(e^{i\omega})\right|^2 \phi_q(\omega) \tag{A.12}$$

$$\phi_{\Delta T q}(\omega) = G^*(e^{i\omega})\phi_q(\omega) \tag{A.13}$$

$$\phi_{q\Delta T}(\omega) = \phi^*_{q\Delta T}(\omega) \tag{A.14}$$

where we have assumed that $G$ is stable. Thus, in our case

$$\phi_z(\omega) = \begin{bmatrix} \phi_q(\omega) & \phi_{q\Delta T}(\omega) \\ \phi_{\Delta T q}(\omega) & \phi_q(\omega) \end{bmatrix} = \phi_q(\omega) \begin{bmatrix} 1 & G(e^{i\omega}) \\ G^*(e^{i\omega}) & \left|G(e^{i\omega})\right|^2 \end{bmatrix} \tag{A.15}$$

which have eigenvalues 0 and $\phi_q(\omega)(1 + \left|G(e^{i\omega})\right|^2)$. Therefore, $\phi_z$ is positive semi-definite and we cannot conclude on informativeness using this method. Note the previous developments are valid for any linear system which can be characterized by $y(t) = H(q)u(t)$ with a quasi-stationary input and a stable transfer function.

## A.5 Non-parametric identification

### A.5.1 Spectral approach

A perhaps naive approach to estimate the transfer function is to calculate it from the frequency domain input and output. This is sometimes referred to as empirical transfer function estimate [12]. This can be done through the spectral densities or through the Fourier Transform (using a Fast Fourier Transform (FFT) algorithm).

$$G(e^{i\omega}) = \frac{\phi_{\Delta Tq}(\omega)}{\phi_q(\omega)} \tag{A.16}$$

or

$$G(e^{i\omega}) = \frac{F_{\Delta T}(\omega)}{F_q(\omega)} \tag{A.17}$$

Using eq.A.17, we obtain the transfer function shown in fig.A.9. Note that zero-padding is not applied in that case since the resolution in frequency is not important for these specific tests.

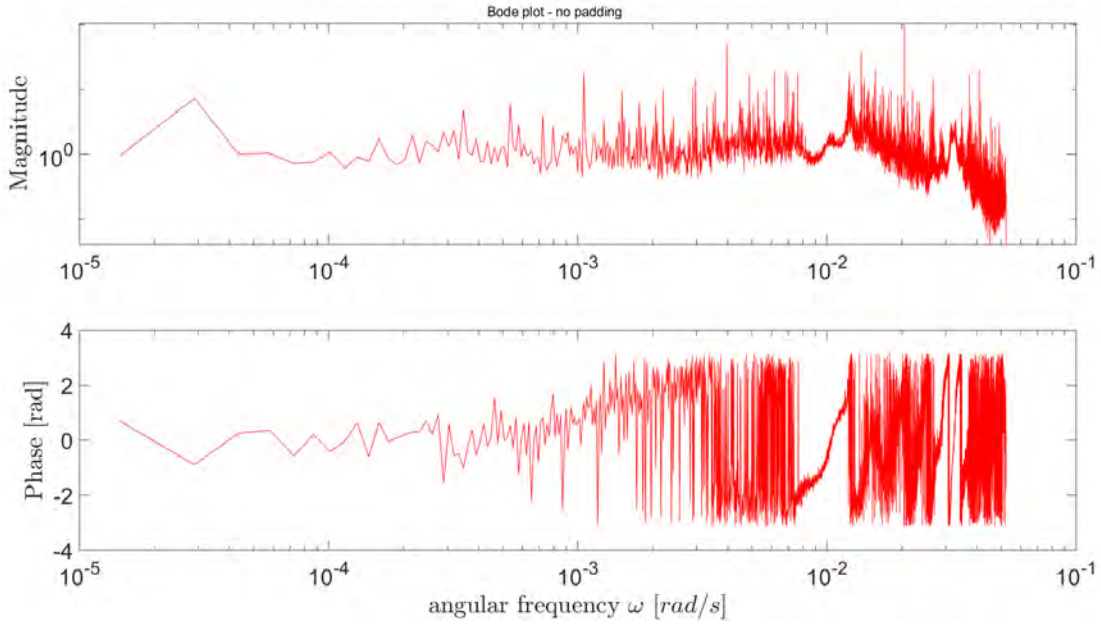


**Figure A.9:** Bode plot of the empirical transfer function estimate for the first TRT, using eq.A.17

As noted here and in the literature (e.g. chapter 3 in [21] and [12]), the previous method usually leads to poor results. Söderström and Stoica [21] propose to give less weight to the terms with large lags in the estimation of the power spectral density. In fact, this is performed by default when using the Matlab function *cpsd*. It uses Welch's algorithm [23] coupled to a Hamming window. The Bode plot of the transfer function obtained from the default power spectral density estimation is shown in fig.A.10a. This transfer function seems to be a better estimation of the true behavior of the system in the sense that we expect the system to behave as low-pass filter.

Several other lag windows were tried for the estimation of the power spectral density but no conclusive results. These lag windows are a way to perform a weighted average of the autocorrelation function when calculating the spectrum. The design of lag window filter was

not extensively studied during this work although it could lead to improvement in the power spectral density estimations.

Another proposition to improve the empirical transfer function estimate is discussed in [12]. The author suggests, among other things, that pre-filtering data is a way to obtain more accurate results. Since it is mostly low frequencies that are interesting for us, a low-pass was applied to data before estimating the power spectral density. The high limit for the low-pass filter was chosen as $\omega = 0.005\ rad/s$ which is about 10 min, i.e. the residence time of the system (the time it takes for the fluid to circulates in the BHE).

The resulting transfer function is shown in fig.A.10b. The Matlab function *impulseest* is used to produce impulse and step responses in the time domain as well as a smoothed Bode plot. This is shown in fig.A.11. There are several issues with this transfer function. Firstly, the step response is not initiated at 0; this is inherent to the transfer function having some constant magnitude for large frequencies (instead of diverging towards $-\infty$ as would be expected). Secondly, the step response reaches steady-state within one hour. In reality steady-state is reached for times much longer than one hour (typically hundreds of years). Since the TRT is only about 100 hours, it is hard to catch this behavior but maybe some condition could be set on the transfer function, e.g. non-zero derivative of the magnitude for $\omega \to 0$. We can already foresee that this will also be a problem for a FIR approach unless the time from which the impulse response is mapped to zero is very large.

The previous non-parametric identification techniques were also tried using the Matlab identifcation toolbox. Others method were also briefly investigated, e.g. correlation (FIR), smoothed Fourier Transform, without further success.

Additionally different filtering techniques and filtering parameters were applied to input data (e.g. filtering to even lower frequencies or filtering only the input power).

Another tested approach was to whiten the noise on input and output data. As may be seen in A.6, the noise is quite "digital", probably due to the resolution of the acquisition unit. Nevertheless, even this approach did not lead to any conclusive identification.

The obtained step and impulse responses, as well as a smooth Bode plot for the second TRT is shown in A.12. The same issues as for the first TRT are encountered although the frequency domain data appears to be neater than for the first TRT, as shown in the Bode plots in fig.A.13a and A.13b, for non-filtered and filtered data (low-pass 0.005 rad/s), respectively.

In the next section, a FIR approach based on the ILS model is developed.

### A.5.2 FIR approach

Alternatively, we can see $\Delta T$ as a (discrete) transfer function:

$$\Delta T(t) = G(q)q(t)$$

And in this instance it is useful to consider the step response of the system, that is, the response to an input of the form $q(t) = q_0 H(t - t_0)$ where $H$ is the Heaviside function. In this instance, equation (A.1) gives us the output of the step response as:

$$\begin{aligned} q_0(R_b^* + \frac{1}{4\pi\lambda^*}E_1(\frac{r_b^2}{4\alpha t_k - t_0})) &= \Delta T(t_k) \\ &= G(q)q(t_k) \\ &= g(0)q(t_k) + g(1)q(t_{k-1}) + \cdots + g(k)q(t_0) \end{aligned}$$

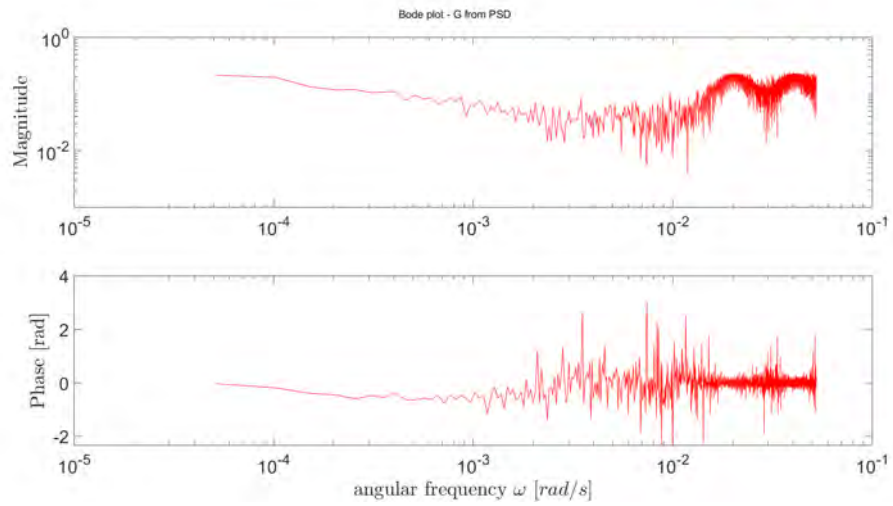


**(a)** non-filtered data

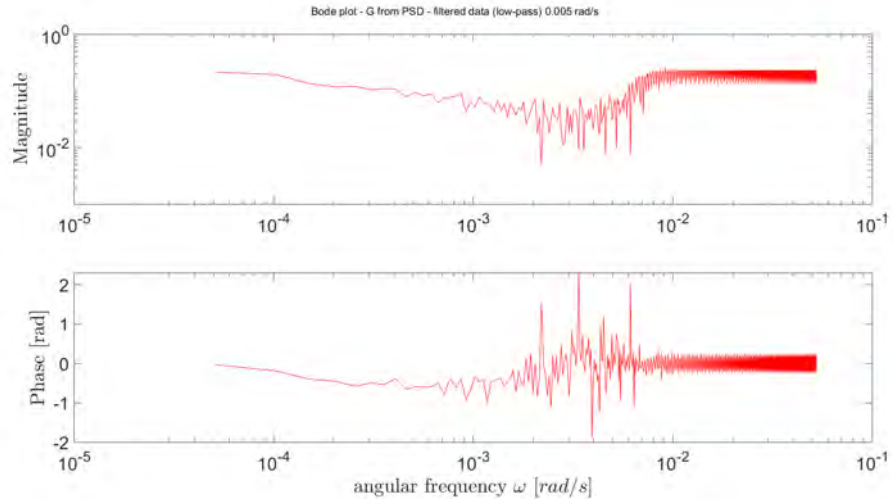


**(b)** filtered data with a low-pass limit set as 0.005 rad/s

**Figure A.10:** Bode plots of the empirical transfer function estimates for the first TRT, using eq.A.16 with Welch's algorithm and a Hamming window

And since $q_0$ is the difference in power before and after time $t_0$, we see this instead as the response to an impulse in the one-step-difference of the input power $\Delta q(t_k) = q(t_k) - q(t_{k-1})$. This evidences the structure of the response as:

$$\begin{aligned} q_0(R_b^* + \frac{1}{4\pi\lambda^*}E_1(\frac{r_b^2}{4\alpha t_k - t_0})) &= \Delta T(t_k) \\ &= \tilde{G}(q)\Delta q(t_k) \\ &= \tilde{g}(0)\Delta q(t_k) + \tilde{g}(1)\Delta q(t_{k-1}) + \cdots + \tilde{g}(k)\Delta q(t_0) \\ &= \tilde{g}(k)q_0 \end{aligned}$$

And so, taking $\tilde{g}(k) = q_0(R_b^* + \frac{1}{4\pi\lambda^*}E_1(\frac{r_b^2}{4\alpha t_k - t_0}))$, and $\tilde{G}(q) = \sum_{k=0}^{\infty}\tilde{g}(k)q^{-k}$. Since any zero-order-hold input can be composed as the a linear combination of step functions, this can be used to extrapolate a general input as

$$\Delta T(t_k) = G(q)q(t_k) = (\tilde{G}(q)(1 - q^{-1}))(q(t_k))$$

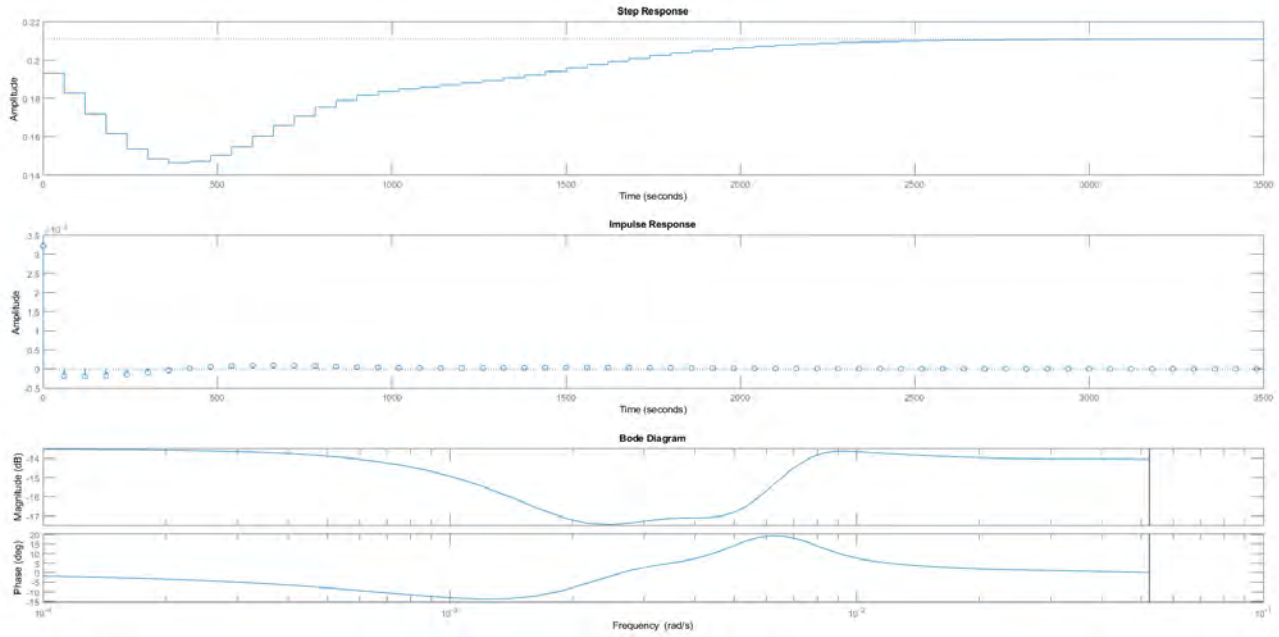


**Figure A.11:** Estimated step and impulse responses as well as smooth Bode diagram for the first TRT

Furthermore when we plot the coefficients of $\tilde{G}(q)$ for the example parameters considered in Figure A.3 we obtain the graph in Figure A.14 of the coefficients for $\tilde{G}(q)$ and $G(q)$.

## A.6 Parameter identification

The usual way of determining the parameters of interest follows by provoking a step response at a fixed power, and plotting $log(t)$ versus $\Delta T$. However, due to the low responsiveness of the system, this approach requires very long test times (circa 100 hours) in order to obtain a useful estimate of the ground thermal parameters. Due to system failures that may be beyond the control of the operator, a test may fail to produce a step response for the required period of time. Moreover, exciting the system with a perfect power step is in practice very hard: the input power is always subject to measurement noise and disturbances from the environment. Fig. A.6 shows data collected from two real tests in which the system failed to perform as intended. By using a FIR approach as proposed above (or another identified model), it is possible to use the full range of output from a non-perfect-step input, in order to obtain an estimate of the ground parameters. By identifying a model (parametrized or not) to a TRT one can then reproduce the response to a perfect input unit step and applied the linear regression with the logarithm of time shown in eq.A.3.

### *A.6.1 Parameter identification through FIR model*

We tried therefore to identify the system in question by employing a high order FIR model with no zeros (i.e. $G(q) = A(q)/B(q)$ with $B(q) = 1$).

This model assumption also allows us to use common system identification theoretic tools to gauge the response of the learned model against the idealized system using, for example, the systems frequency response. In Figure A.15 we show the bode plot of the idealized system from figure A.14.

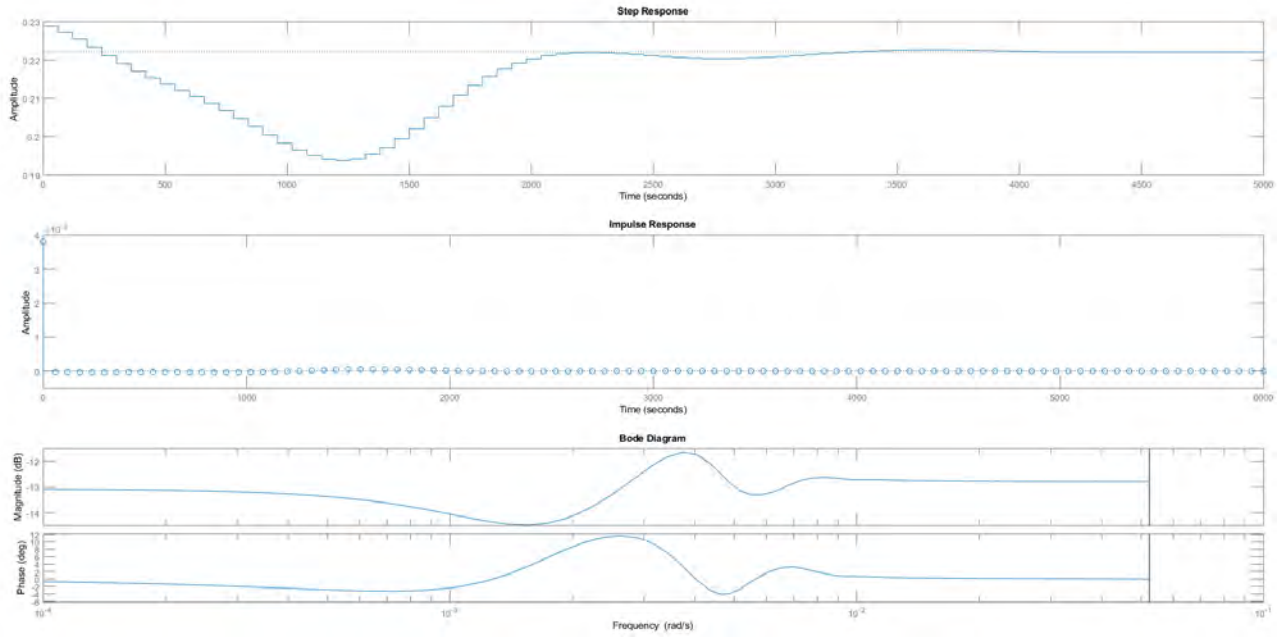


**Figure A.12:** Estimated step and impulse responses as well as smooth Bode diagram for the second TRT

From analyzing Figure A.15 we can see that the frequency response has support on frequencies below 0.01 rad/s and has no peaks. We expect this shape to be maintained across the range of parameters of a TRT system, and therefore we can use this criterion (smooth frequency response with a support bounded by below) to eliminate candidate systems which do not meet this criteria.

### A.6.2 Transfer function models

Continuous time transfer function models of different order were identified to the first TRT. The number of poles and zeros were arbitrarily chosen and the best fitting models are presented here. All transfer functions are rational functions and the selected transfer models are such

- $G_1(s) = \frac{a_3s^3+a_2s^2+a_1s+a_0}{b_4s^4+b_3s^3+b_2s^2+b_1s+b_0}$
- $G_2(s) = \frac{a_3s^3+a_2s^2+a_1s+a_0}{b_4s^4+b_3s^3+b_2s^2+b_1s+b_0}$ with fitting over the frequency range 0-0.01 rad/s
- $G_3(s) = \frac{a_1s+a_0}{b_2s^2+b_1s+b_0}$ with fitting over the frequency range 0-0.01 rad/s

Data from TRT1 is segregated into a training set and a validation as shown in A.16. This specific segregation is chosen so that the models accurately reproduce the long-term behavior of the TRT which is dominated by heat transfer in the ground (it can take up to 10-20 hours before the ground significantly affects the thermal response). A tuned frequency range was chosen because it is mostly the long-term behavior of the system that is of interest. Moreover, pre-filtered input data was used (low-pass 0.005 rad/s).

Note that rational transfer function in the Laplace domain can be inversed back into the time domain by using partial fraction decomposition so that

$$\frac{P(s)}{Q(s)} = \frac{c_1}{s-r_1} + \frac{c_2}{s-r_2} + ... + \frac{c_n}{s-r_n} \tag{A.18}$$

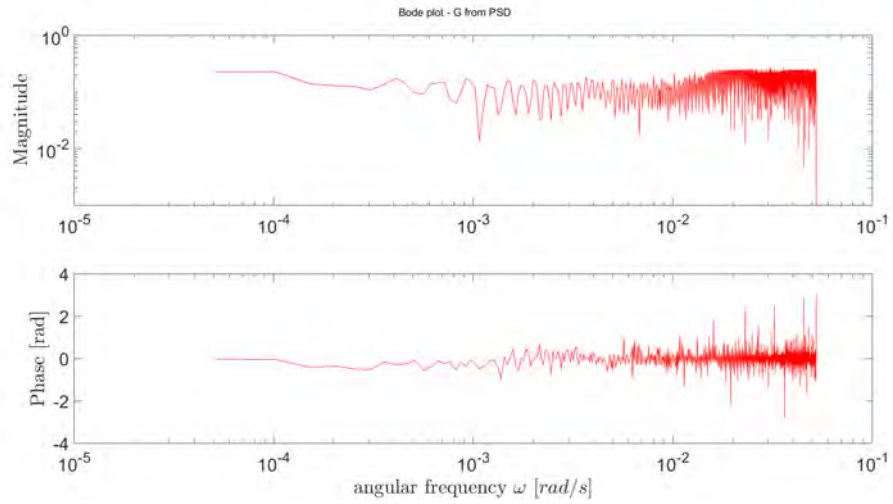


**(a)** non-filtered data

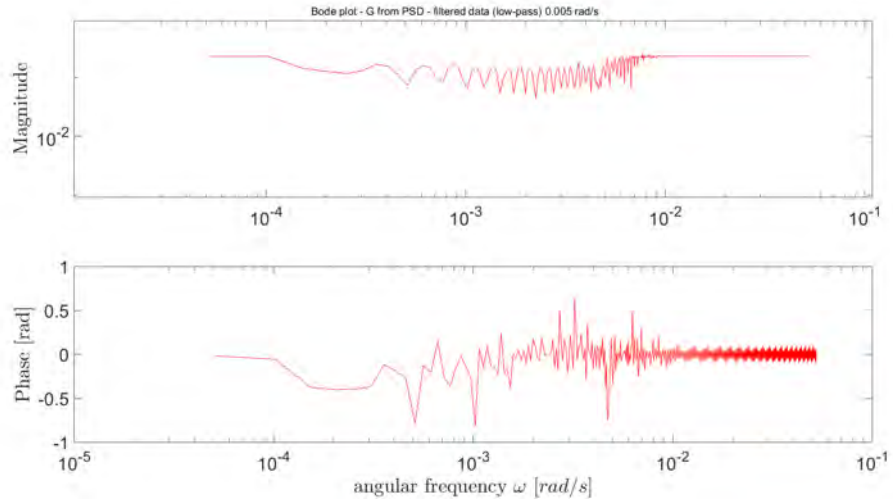


**(b)** filtered data with a low-pass limit set as 0.005 rad/s

**Figure A.13:** Bode plots of the empirical transfer function estimates for the second TRT, using eq.A.16 with Welch's algorithm and a Hamming window

with $Q(s) = (s - r_1)(s - r_2)...(s - r_n)$ where $r_1, ...r_n$ are distinct roots of $Q$ and $deg(P) < deg(Q)$.

The identification process led to the following parameters value:

- $G_1(s)$ : $a_3 = 1.2790 \cdot 10^{-4}$ $a_2 = 1.3003 \cdot 10^{-7}$ $a_1 = 1.3365 \cdot 10^{-11}$ $a_0 = 1.8845 \cdot 10^{-16}$
  $b_4 = 1$ $b_3 = 0.0027$ $b_2 = 1.0772 \cdot 10^{-6}$ $b_1 = 7.5849 \cdot 10^{-11}$ $b_0 = 7.9725 \cdot 10^{-16}$
- $G_2(s)$ : $a_3 = 4.5365 \cdot 10^{-5}$ $a_2 = 2.4348 \cdot 10^{-7}$ $a_1 = 2.5200 \cdot 10^{-11}$ $a_0 = 3.0906 \cdot 10^{-16}$
  $b_4 = 1$ $b_3 = 0.0032$ $b_2 = 2.1133 \cdot 10^{-6}$ $b_1 = 1.3967 \cdot 10^{-10}$ $b_0 = 1.3030 \cdot 10^{-15}$
- $G_3(s)$ : $a_1 = 6.5256 \cdot 10^{-5}$ $a_0 = 1.9679 \cdot 10^{-9}$
  $b_2 = 1$ $b_1 = 4.4805 \cdot 10^{-4}$ $b_0 = 8.4542 \cdot 10^{-9}$

The roots found for each $G$ are real and negative which indicates that the impulse response in the time domain is just a sum of decaying exponential terms and the transfer functions are

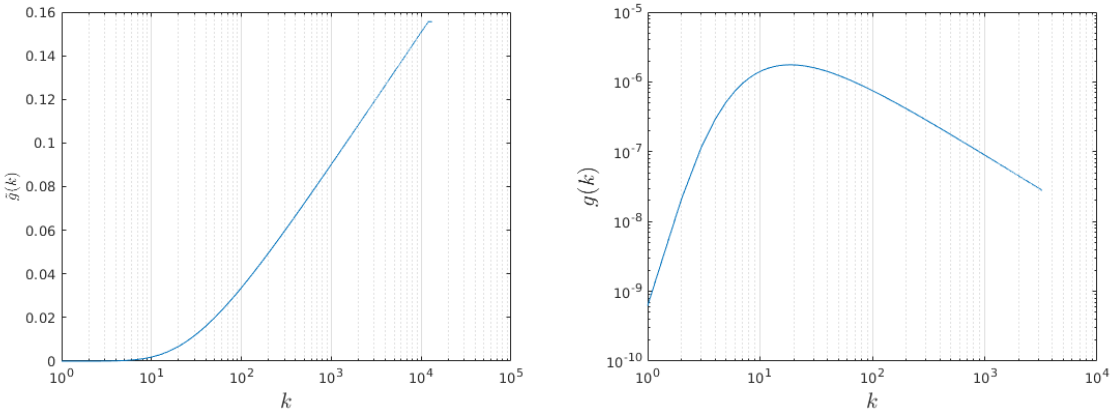


**Figure A.14:** Plot of the coefficients for the transfer functions $\tilde{G}(q)$ and $G(q)$ respectively. The horizontal axis is $k$ and the vertical axis corresponds to $\tilde{g}(k)$ and $g(k)$, respectively. Essentially these plots correspond to the step and impulse responses of the system $G(q)$.

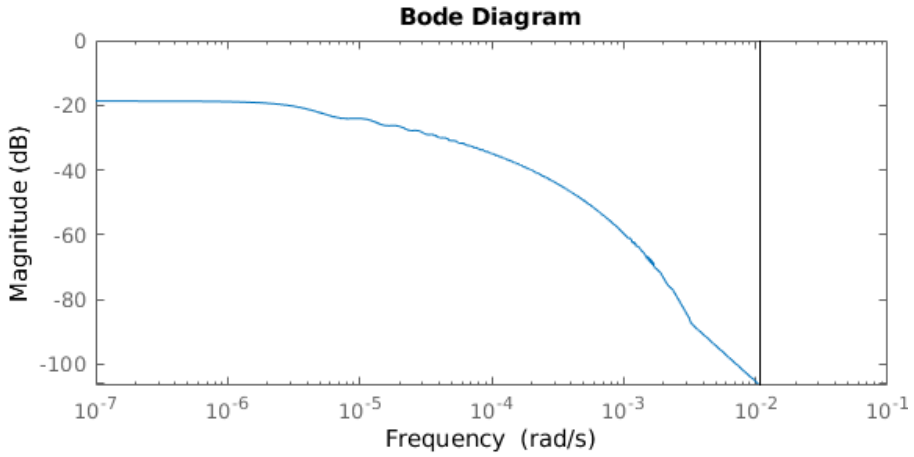


**Figure A.15:** Frequency response of the idealized system described in Section A.5.2.

stable, respectively. For instance

$$g_1(t) = 6.4954 \cdot 10^{-8} e^{-0.0022t} - 5.3802 \cdot 10^{-10} e^{-3.7915 \cdot 10^{-4} t} + 1.1155 \cdot 10^{-11} e^{-7.3604 \cdot 10^{-5} t} - 5.2956 \cdot 10^{-13} e^{-1.} \tag{A.19}$$

The step response can then be obtained by $\int g_1(t)dt$.

### A.6.3 High-order ARX

The idea behind having a high-order ARX model is to have a good representation of the long-term behavior of the test. The identified ARX model has the form

$$\sum_{k=0}^{20} a_k q^{-k} y(t) = \sum_{k=1}^{200} a_k q^{-k} u(t) + e(t) \quad with\ a_0 = 1 \tag{A.20}$$

and presents the best fit over the validation set with a best fit factor of about 74%. Note that, here, $y$ and $u$ are used for the output and input, instead of $\Delta T$ and $q$, respectively, to avoid confusion with the shift operator $q$.

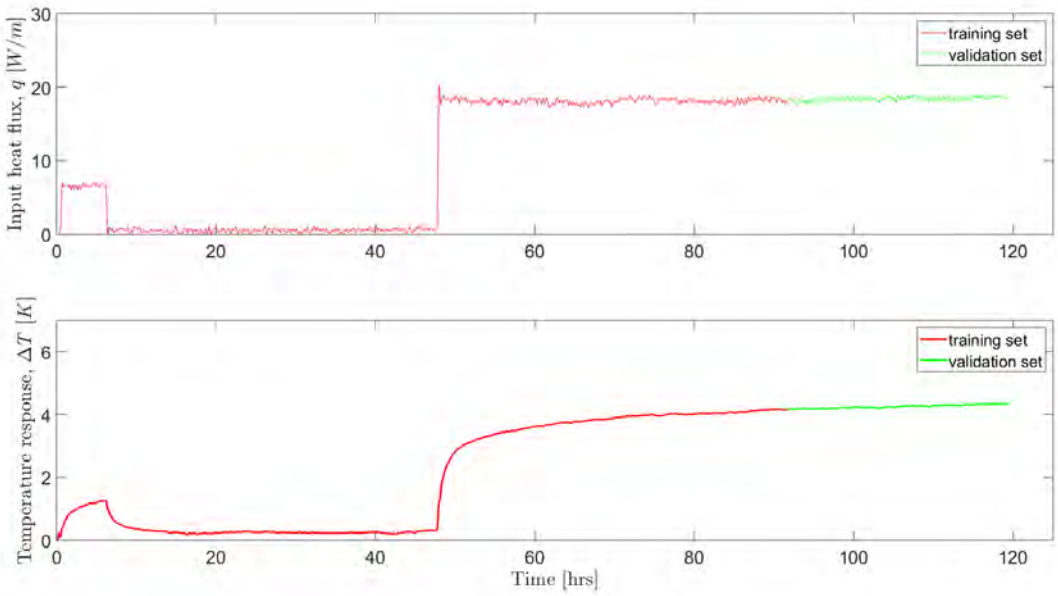


**Figure A.16:** Training and validation sets used for identification for the first TRT

### A.6.4 Low-order ARMAX, Box-Jenkins and Output error

In the perspective of trying different types of model, low order ARMAX, Box-Jenkins and Output Error models were identified. The models are described, respectively, as follows

$$(1 + a_1 q^{-1} + a_2 q^{-2}) y(t) = (b_1 + b_2 q^{-1}) u(t-1) + (1 + c_1 q^{-1} + c_2 q^{-2}) e(t) \tag{A.21}$$

$$y(t) = \frac{b_1 + b_2 q^{-1}}{1 + f_1 q^{-1} + f_2 q^{-2}} u(t-1) + \frac{1 + c_1 q^{-1} + c_2 q^{-2}}{1 + d_1 q^{-1} + d_2 q^{-2}} e(t) \tag{A.22}$$

$$y(t) = \frac{b_1 + b_2 q^{-1}}{1 + f_1 q^{-1} + f_2 q^{-2}} u(t-1) + e(t) \tag{A.23}$$

Again, $y$ and $u$ are used for the output and input, instead of $\Delta T$ and $q$, respectively, to avoid confusion with the shift operator $q$.

### A.6.5 Parameter estimation: comparison with state-of-the-art method

**First TRT**

Beside their fit to the validation set, another performance metric for the different models is how useful they are in estimating the thermal conductivity of the ground and the borehole thermal resistance.

The estimation is performed by applying linear regression of eq.A.3 to the calculated step response of each model. Note the the thermal conductivity is inversely proportional to the slope and the borehole thermal resistance is proportional to the intercept coefficient.

Unfortunately, the true value of estimated parameters is not known in our case. The results are therefore compared to those obtained with the time-superposed ILS model, i.e. the convolution product between the step response and the power increments in time (see section A.5.2). For such a model, the approximation presented in section A.2.1 are not necessarily valid and linear regression in the logarithmic time domain cannot be applied in a

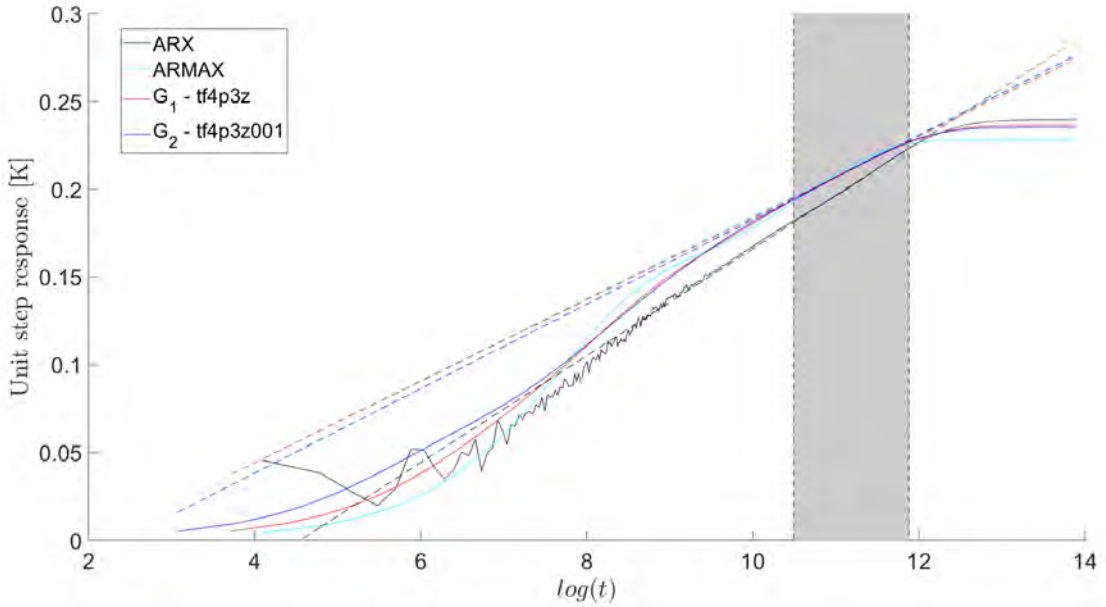


**Figure A.17:** Unit step responses for the ARX, ARMAX and the first two transfer function models (optimization period 10-40 hours) - first TRT

straightforward way. Thus, an optimization algorithm must be used to find the different parameters. Here the optimization algorithm used is the Newton-Raphson method as presented in [15]. The obtained results are tied to the chosen optimization period over which the sum of squared errors are minimized. For the first TRT, the optimization period was chosen between 65 and 120 hours (see fig.A.6a). The obtained thermal conductivity and borehole thermal resistance were of 4.05 $W \cdot m^{-1} \cdot K^{-1}$ and 0.12 $m \cdot K \cdot W^{-1}$, respectively. For the second TRT, the optimization period was chosen between 70 and 140 hours (see fig.A.6b). The obtained thermal conductivity and borehole thermal resistance were of 2.71$W \cdot m^{-1} \cdot K^{-1}$ and 0.084$m \cdot K \cdot W^{-1}$, respectively. These results are counter-intuitive in the sense that the two tests are performed in the same borehole and should therefore lead to a similar thermal conductivity. The thermal borehole resistance is expected to be different since the filling material inside the borehole was changed between the two tests (groundwater in the first test, grout in the second test). For more information about the tests and analysis, see [14].

Fig.A.17 shows the unit step responses for the ARX, ARMAX and the first two of the transfer function models ($G_1$ and $G_2$ with 4 poles and 3 zeros, see above). The grey area represents the optimization period used for the parameter estimation. The obtained linear curves (in the logarithmic time domain) are plotted with dashed lines. In fig.A.18a and fig.A.18b the final value of thermal conductivity and borehole thermal resistance, respectively, are displayed for all the different models. The obtained results are somewhat different from the time superposed ILS (ILS Newton-Raphson) and that may be due to the chosen optimization period. It is hard to compare with the optimization period chosen to perform the Newton-Raphson optimization since it is not the unit step response that is used but raw data from the TRT. Nevertheless, we can observe that the optimization period that was chosen to perform the Newton-Raphson optimization is rather late in the response (65-120 hours, corresponding to about 20-75 hours after the second power step, see fig.A.6a). From all the different models, it seems like the derivative of the unit step response with respect to $log(t)$ decreases for $log(t) > 12$ approximately. This corresponds to about 45 hours.

If a the optimization period is chosen as 20 to 75 hours after the unit step starts, the results

become quite different as shown in fig.A.19 and A.20. To further study the effect of the optimization period choice, parameter estimation was performed for varied optimization periods by either varying its start or stop time. The resulting thermal conductivity for the different models are shown in fig.A.21a for varying start time and in fig.A.21b for varying stop time. Note the different scale between the two graphs.

The first thing we can notice is that the estimation of thermal conductivity seems to be much more sensitive to the start time than stop time. This might due to the models reaching steady-state too early. Secondly, there seem to be some coherence between the models for long optimization periods. This most likely due to averaging effects but is still a positive sign. Thirdly, the high-order ARX models does not seem to be as sensitive as the other models to the change of optimization period although there is still a significant variation. The ARX model is the best model in terms of fitting the validation set (ca 74%) but has the worst fit for the whole test (ca 95%).

The model representing best the whole test is $G_1$ with a fit of 97.6%. Qualitatively, $G_1$ has a similar behavior to the time-superposed ILS model in terms of how the thermal conductivity changes with the optimization period. The fact that all models lead to a higher thermal conductivity for larger stop times may be due to models reaching steady-state too early but it may also reflects a true physical phenomenon such as convective heat transfer due to groundwater flow.

Note that the Box-Jenkins and Output Error models gives the same results in terms of the parameter estimation, presumably because the error models are disregarded when computing the step responses.

**Second TRT**

The second TRT is here used only as a validation set: no models are identified to it, rather the second TRT is used to check if the identified models with the first TRT can be generalized. Also, we expect the short-term behavior (0 20 hours) of the test to be different and this expected difference is of interest.

The performance of the different models, identified with data from the first TRT, are shown in fig.A.22. None of the models seem to be able to reproduce the long-term behavior of the second TRT. Note that, using the state-of-the-art method, the fit is good between the optimized parametrized model and data, but the parameters are significantly different than in the first TRT. This is not so strange for the borehole thermal resistance which is expected to be different because it is not the same material inside the borehole. However, the ground around the borehole is supposedly the same (since both tests are performed in the same borehole) so it is curious to find different ground thermal conductivity. This is discussed more in details in [14] but this study might be further indication that the long-term behavior actually is different, e.g. because of groundwater flow. The way models were trained can also be a reason of this discrepancy at longer times.

Surprisingly, some models ($G_1$, $G_2$ and $ARX$), successfully reproduce the short-term behavior of the temperature response although the material inside the borehole is different. This is interesting and deserve more investigation in future studies. Note that this study has focused on the long-term behavior but the short-term heat transfer is also very relevant to investigate, especially from a control optimization perspective. At the second power step, however, only the ARX model is able to properly reproduce the transitive behavior of the temperature response.

The ARX model is also able to reproduce the response until about 67 hours, which should

be enough to estimate a thermal conductivity (not done here).

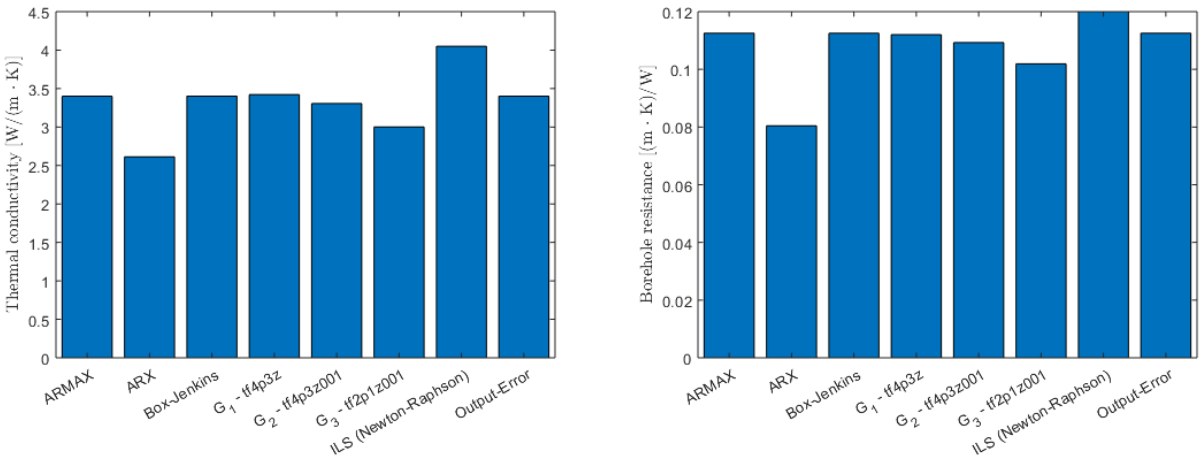


**(a)** Thermal conductivity **(b)** Borehole thermal resistance

**Figure A.18:** Estimated parameters for the first TRT for different models (optimization period 10-40 hours, except ILS Newton-Raphson)

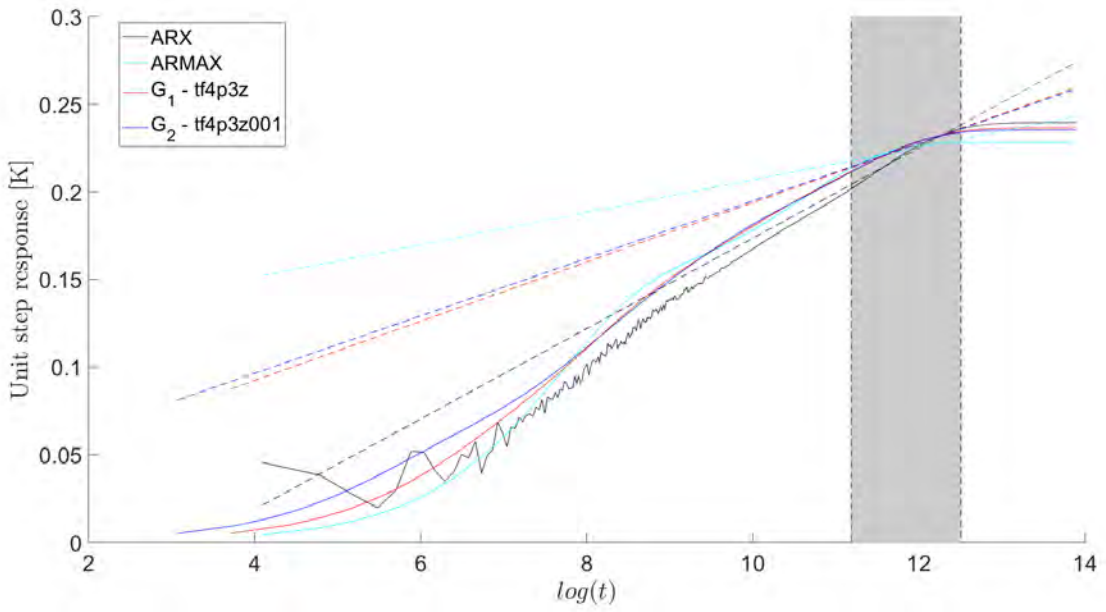


**Figure A.19:** Unit step responses for the ARX, ARMAX and the first two transfer function models (optimization period 20-75 hours) - first TRT

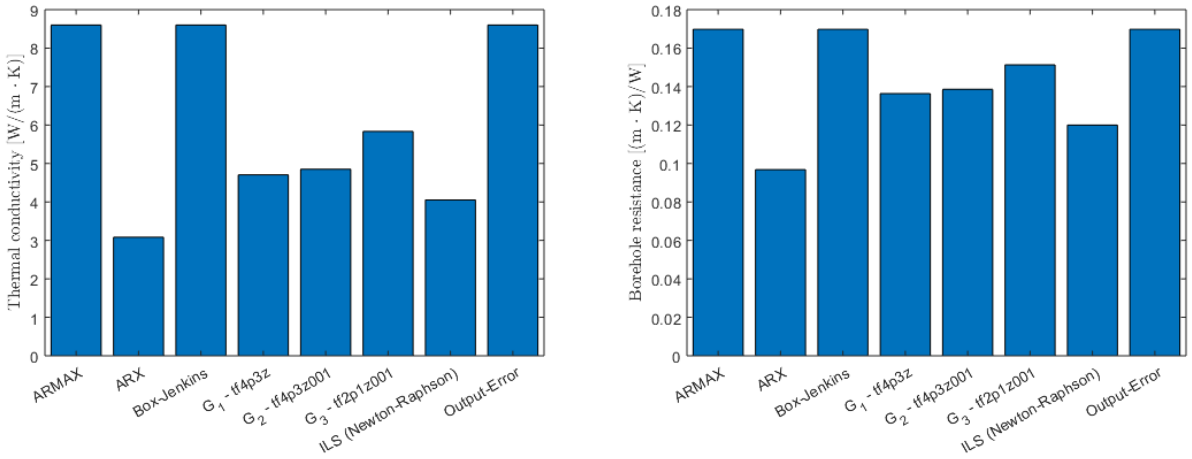


**(a)** Thermal conductivity **(b)** Borehole thermal resistance

**Figure A.20:** Estimated parameters for the first TRT for different models (optimization period 20-75 hours, except ILS Newton-Raphson)

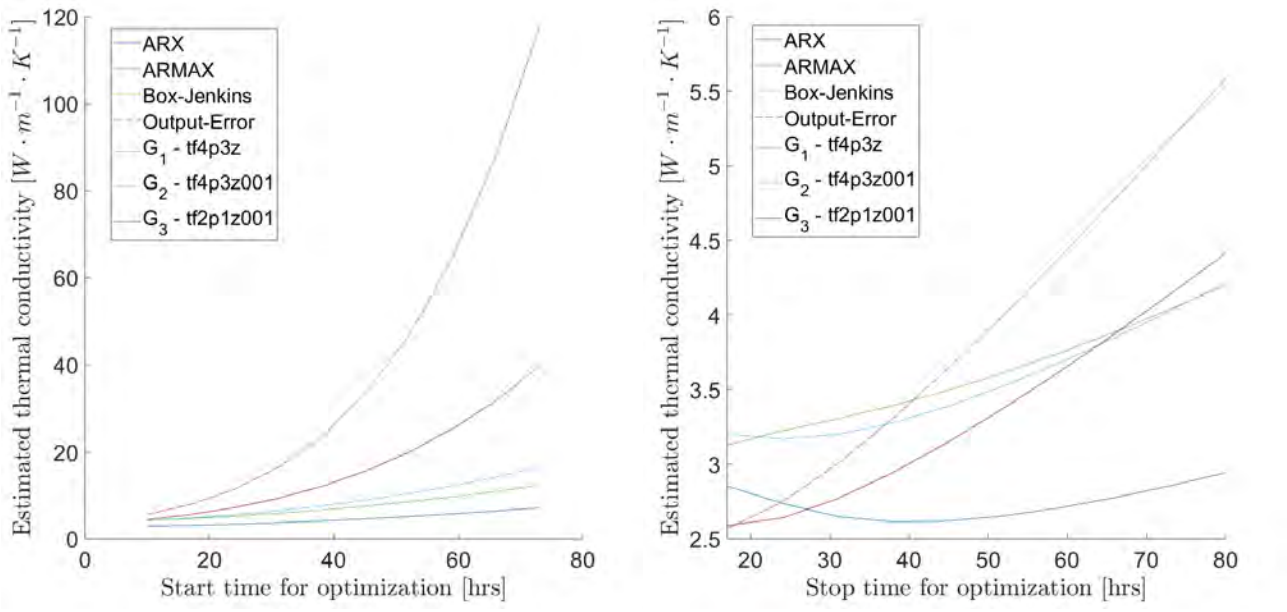


**(a)** Varying start time, stop time fixed at 80 hours **(b)** Varying stop time, start time fixed at 10 hours

**Figure A.21:** Effect of varying optimization period on estimation of thermal conductivity

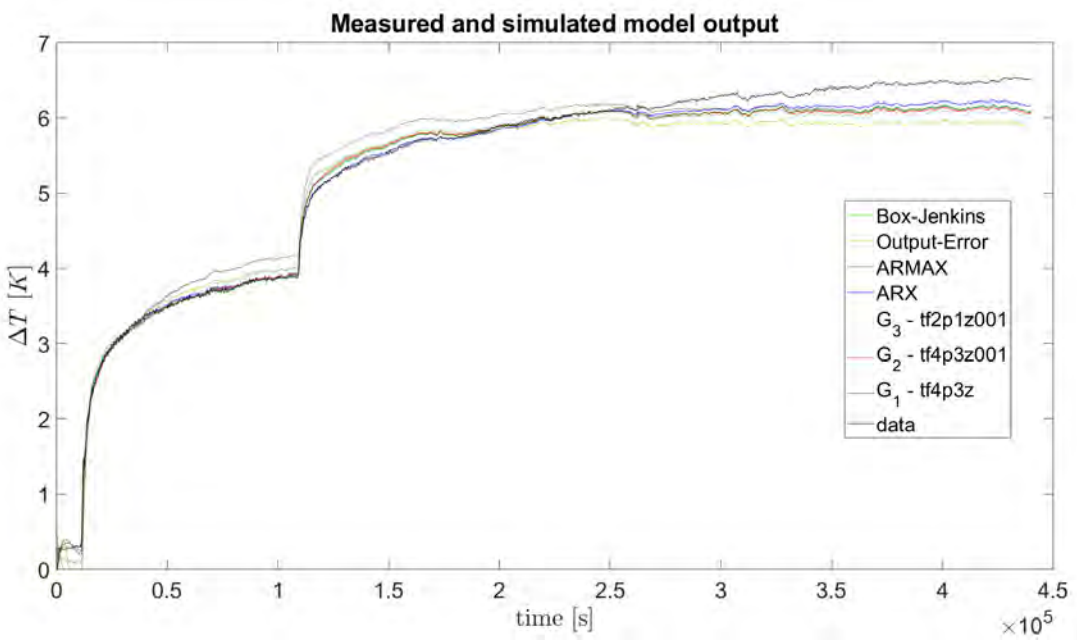


**Figure A.22:** Comparison between the second TRT and the models identified using the first TRT

## A.7 Conclusion

This project investigated the application of system identification methodologies to thermal response testing, which is used to estimate thermal properties of borehole heat exchangers and the surrounding ground.

First, the bias linked to the traditional MSE approach was investigated theoretically. It was shown that the bias induced by input noise should be proportional to the Frobenius norm of the impulse response. For a set of realistic parameters, it was shown that this norm is small in comparison to the variance term of the output. Some numerical examples were used to highlight the bias induced in the estimation of the ground thermal conductivity.

Secondly, input informativeness was investigated both using data and theoretically. Data seems to point in the direction of informative tests although this could be due to numerical effects. Theoretically, it was shown that the positive-definiteness of the spectrum of combined input-output cannot be used to determine if the test is informative. This result seemed to hold for any linear system with stable transfer function and quasi-stationary input.

Then non-parametric identification methods were investigated with an emphasis on spectral methods and FIR model. The spectral approach was not conclusive although it would be potentially very useful since the true response of the system be obtained. Being succesfull in this approach most likely requires further digital signal processing.

An FIR model of a TRT system using the equations for an ILS model was derived. Which can be used as an indicator of a learned model's suitability. Ultimately this was used in the model learning step to provide a prior on the expected shape of a model's input/step response as well as its frequency response.

Parametric methods were finally investigated. Models were trained on a portion of one thermal response test and checked again the validation set. The identified models were transfer functions, ARX, ARMAX, Box-Jenkins and Output-Error models. Rather than deriving the thermal properties from the value of the parameters identified in each model, the step response for each model was computed and then interpreted using the state-of-the-art ILS model. Models showed some ability to estimate the thermal properties of the ground as compared to a time-superposed ILS using a Newton-Raphson optimization method. Nevertheless, the results were very dependent on the chosen optimization period; maybe partly because the behavior of the system is different from expected, but maybe also because of having finite impulse responses within the test duration. This means reaching steady-state while performing the TRT which does not happen in reality.

The identified models were used with the second TRT as validation set but they could not reproduce the long-term behavior of the system. This might be further evidence that the long-term heat transfer behavior of the ground is effectively different between the two tests although they are performed in the same borehole (with different filling material but same surrounding ground). This could be the case if groundwater flow was effectively present during the first test and reduced due the grouting procedure in the second test.

Although not always successful, the system identification methods showed some potential for the TRT application. Besides further investigating the methods used in this work, some other investigation points could be undertaken. Using a Kernel-based regularization procedure is one of them; here it shown that that the ILS model have an impulse response with the behavior $A\frac{1}{t}e^{-\frac{C}{t}}$ so this could be used as a basis for the Kernel regularization. Synthetically replicating the signal or mirroring it to improve digital signal processing is a lead to be investigated.

Our initial hypothesis that system identification methods can be used to reduce the test

duration which is today quite long (at least 3 days) remains to be fully assessed. For this to take place, we need better understanding the accuracy of the estimation (variance of estimated parameters). Using another set of inputs/output is possible and could be more sound, e.g. the outlet temperature of the borehole heat exchanger as output and the inlet temperature and flow rate as input.

Finally, system identification could be used to better understand and characterize the short-term behavior of heat transfer inside borehole heat exchangers.